



Production of Solar Fuels using CO₂

DOCTORAL THESIS

Universita` degli Studi di Messina (HOME)

and

École supérieure de chimie physique électronique de Lyon,

Université Claude Bernard Lyon 1 (HOST)

SINCHEM - Sustainable and Industrial Chemistry

Erasmus Mundus - Joint Doctoral Research program

Dottorato di XXIX ciclo in

Ingegneria e Chimica dei Materiali e delle Costruzioni

and

Ecole Doctorale N° 206

(Ecole Doctorale de Chimie de Lyon : Chimie, Procédés, Environnement)

Supervisor (HOME): Prof.ssa Siglinda PERATHONER

Co-Supervisor: Dr. Claudio AMPELLI

Supervisor (HOST): Prof.ssa Elsje Alessandra QUADRELLI

Co-Supervisor: Dr. Chloe THIEULEUX

Thesis by

Bhanu Chandra MAREPALLY

April, 2017

Doctoral Defense Committee :

University of Messina

FORNASIERO, Paolo Prof. <i>Universita degli Studi di Trieste</i>	Referee
FONSECA, Isabel Prof. <i>Universida de Nova de Lisboa,</i>	Referee
LECLAIRE, Julien Prof. <i>Université de Lyon 1</i>	Jury (Internal)
CENTI, Gabriele Prof. <i>Universita degli Studi di Messina</i>	Jury (Internal)
DI RENZO, Francesco Prof. <i>CNRS, ICG Montpellier</i>	Jury (External)
GARCIA GOMEZ, Hermenegildo Prof. <i>Universidad Politecnica de Valencia</i>	Jury (External)
PERATHONER, Siglinda Prof. <i>Universita degli Studi di Messina</i>	Supervisor
QUADRELLI, Elsje Alessandra Prof. <i>Université de Lyon 1</i>	Supervisor

University of Lyon

DI RENZO, Francesco Prof. <i>CNRS, ICG Montpellier</i>	Referee
GARCIA GOMEZ, Hermenegildo Prof. <i>Universidad Politecnica de Valencia</i>	Referee
CENTI, Gabriele Prof. <i>Universita degli Studi di Messina</i>	Jury
LECLAIRE, Julien Prof. <i>Université de Lyon 1</i>	Jury
PERATHONER, Siglinda Prof. <i>Universita degli Studi di Messina</i>	Supervisor
QUADRELLI, Elsje Alessandra Prof. <i>Université de Lyon 1</i>	Supervisor

Dedicated

To

My Beloved Parents, my Wife

&

My Guru

EPIGRAPH

Every event in the history of time
can be defined by the
Conscious group of particles in existence.

ACKNOWLEDGEMENT

First and foremost, I express my deepest gratitude and love to the God Almighty for his grace to give me this wonderful opportunity to work in this fascinating field of artificial photosynthesis.

Now, I would like to express my love to *my dear father – M .Rajender Rao, my dear mother – Lakshmi Devi, my Late grandfather – E. Raj Gopal Rao, my brother – Sharath Chandra, my sister-in-law – Sravani Deekshit, my loving wife – Sindhoora and my relatives* for their continuous support and encouragement to walk the path of my heart. I thank all **my ancestors** for all their secret blessings.

I am forever grateful and I express my heartfelt thanks to **Late Dr. Jewan Prakash Raina** my **Guru**, ex-Senior Professor & Director, Centre for Nano Technology, VIT, India for his timely guidance & motivation all along my Masters and his advices to overcome the obstacles & keep moving forward to solve real world problems not just limited to the field of Nano Technology.

Any PhD. degree is not possible without a great guiding mind. I am very thankful to have **Prof. Siglinda Perathoner**, University of Messina, Italy as my principal advisor. I will never forget all the support you gave me with the many official works in Messina and the warmly welcome on my first day of my life in a foreign country. I still think, if it is coincidence or destiny that we both are born on the same day.

In life, there are times, when we need to make critical decisions, some show you the path and you will understand their meaningful words only as time passes! I thank you **Prof. Elsjé Alessandra Quadrelli**, for your better judgment and guidance even before you became my second principal advisor from CPE, Universite Claude Bernard Lyon, France.

Although, I got to speak to **Prof. Gabrielle Centi** only a handful times, I am very inspired by his work culture and passion towards research, thank you for being the anchor to all our research and experimentations.

Most of the times, professors are busy with a lot of works, I am very lucky to have **Dr. Claudio Ampelli**, as a Co-supervisor and more a mentor, guiding me on each step of my PhD research.

My research work at UCBL Lyon was for a short period, but I was fortunate to get guidance from *Dr. Chloe Thieuleux* in a few discussions. I would also like to thank *Dr. Jerome Canivet* for the precise expertized teachings on MOF synthesis techniques in a very short time.

All these acknowledgements would not have been possible without *SINCHEM*. I sincerely thank SINCEM program, the committee, and all its professors for their constant support and encouragement. A special thanks to *Prof. Stefania Albonetti*, SINCEM coordinator, for making this program not just a give and take, but a close family with strong scientific as well as cultural roots spread across the world.

I thank the University of Messina, Italy, École supérieure de chimie physique électronique de Lyon (CPE), Claude Bernard University (UCBL), Lyon 1, France and Institut de recherches sur la catalyse et l'environnement de Lyon, France (IRCE Lyon) for the necessary support and facilities.

I express my sincere thanks to Dr. Gargi Raina, Dr. Nirmala Grace, Dr. Bala Praveen Chakkravarthy, Dr. V. Velmurugan, Dr. Harish Kittur, Dr. P. Penchalaiah, Dr. George Jacob and Dr. K. Sivasankaran VIT University for their guidance and support during my Masters.

The seeds towards research are not sowed and reaped in a day - I would like to thank Dr. Chandrasekhar Mukku, Dr. M. B. Srinivas, Dr. R. Govindarajulu, Dr. G. Ram Murthy, Mr. Madhusudhan Rao, Dr. Vinayak Rao, Dr. K. Srinivasa Chary, Dr. U. Trivikram, Mrs. T. Naga Sree, Dr. V. Vishwanath Rao, Dr. Jaisval and Dr. Laxmi Narayana Prusty for their teachings and creation of strong foundation and thoughts in the field of science and technology.

Every research lab is defined by its group of researchers, each one of them contribute in some way along your journey of PhD. A simple thanks would never suffice for the many things you have taught me – it may be basic chemistry or laboratory pre-cautions or analytical tools and techniques or experimental procedures or fun talks about nothing and everything. You have been there for me right from my first step till the end, Thank you – Giorgia, Chiara, Salvatore, Paolo, Francesco, Maria Grazia, Roberto Pizzi, Gianfranco, Paola, Rosalba, Katia, Serena, Maria, Leone, Roberto Di Chio, Robert, Andres, Chalachew, Chen, Reine, Florian Wisser, Audrey, Iuliia, Tibo, David, Matthieu, Stephane, Walid, Bishoy, Ewelina, Aabid, Fred, Saranya, Gouthami, Felix, Ram and Santosh Rauri.

Engineering and tools play a major role in research, I thank Laurent Veyre, for his support with the electron-microscopy techniques and Daniele Cosio, for his support with mechanical designing of the cells.

A special thanks to my first friend abroad Atif, our saviors ‘saint’ Anna Maria, Mrs. Francesca Pollicino, Angela Garozzo, Macro Fabienne, Maria Angelina Beaucourt, Francois Bayard, Catherine Dallagnol and Lina Lagana.

A special thanks to our very own 1st SINCHEM family - Giuliana, Atif, Olena, Yu Zhang, Maria, Emilia, Tahrizi and Asja.

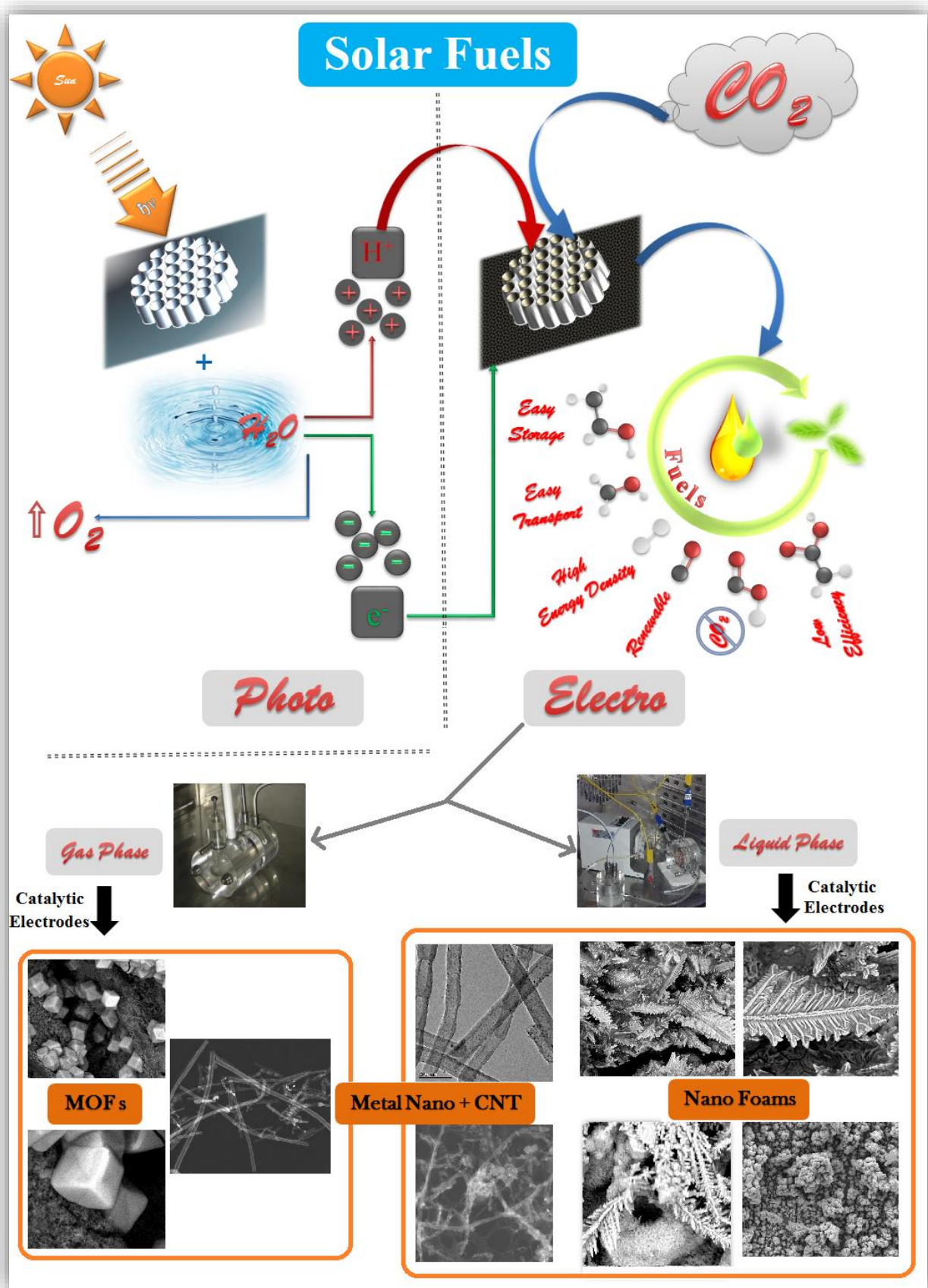
I thank my very special friends Tapish, Vishnu, Late Raju, Harish, Arya, Harsha, Mahesh, Naidu, Raghu, Sunil, Sumanth, Vamsi, Sundar, Rahim, Satheesh, Soundara Rajan, Chaithanya, Saurabh, Pooja, Kamran, Khaoula, Ramzi, Kiran Kumar, Jagadeesh, Mohan and Sreedhar.

I thank all my gamer friends who made my life, a notch more electrifying.

And last but not the least, I thank all my fellow conscious group of atoms, directly or indirectly responsible for the existence of this event in the history of time.

MAREPALLY BHANU CHANDRA

Graphical Abstract



Abstract (English)

In view of the recent alarming rate of depletion of fossil fuel reserves and the drastic rise in the CO₂ levels in the atmosphere leading to global warming and severe climate changes, tapping into all kinds of renewable energy sources has been among the top priorities in the research fields across the globe. One of the many such pathways is CO₂ reduction to fuels using renewable energies, more commonly referred as artificial photosynthetic cells or artificial leaves or photo-electro-catalytic (PEC) cells.

The key objective of the present PhD work was to conduct in-depth studies on two different electro-catalytic CO₂ reduction systems: electrolyte-less cell (gas phase) and electrolytic cell (liquid phase). In particular, a novel lab scale liquid phase cell, on the similar lines of the previously realized gas phase cell at the University of Messina, was developed and used to convert electro-catalytically CO₂ to more value-added products. The work was carried out at the Laboratory CASPE/INSTM of the University of Messina (Department of Electronic Engineering, Industrial Chemistry and Engineering). During the second year, a six-month period was spent at the École supérieure de chimie, physique, électronique de Lyon (CPE Lyon), where organometallic routes were explored for the synthesis of novel composite materials to be used as electrocatalysts in the CO₂ reduction process.

Experimental tests were carried out on various types of catalysts in both the gas and liquid phase cells to understand the different selectivity, productivity and the reaction products obtained. Liquid phase, in fact, has been the most studied process in literature, but some issues mainly related to CO₂ solubility and types of products formed (i.e. mainly formic acid), have never be allowed to pass the lab scale stage. The general aim of this PhD was to prepare novel metal doped nanocarbon substrates, which are very different with respect to the conventional metal bulk layers used as electrocatalysts in CO₂ reduction, and test them both in gas phase (to take advantage of these conditions, i.e easy recovery and improved quality of the products) and in liquid phase (to have a better comparison with conditions typically adopted in literature).

For the studies on the electro-catalytic reduction of CO₂ in gas phase cell, a series of electrodes (based on Cu, Fe, Pt and Cu/Fe metal nanoparticles – NPs - deposited on carbon nanotubes – CNTs - or carbon black and then placed at the interface between a Nafion membrane and a gas-diffusion-layer) were prepared. The results, evidencing the various types of products formed and their different productivities, are very promising. Under electrolyte-less conditions, the

formation of $\geq C1$ products (such as ethanol, acetone and isopropanol) were observed, the highest being for Fe and closely followed by Pt, evidencing that also non-noble metals can be used as efficient catalysts under these conditions. To enhance the productivities of the CO₂ reduction, a different set of electrodes were also prepared based on substituted Zeolitic Imidazolate (SIM-1) type MOF coatings during a stay at CPE Lyon and Institut de recherches sur la catalyse et l'environnement de Lyon (IRCELYON). Particularly, the catalysts tested were MOF-based Fe-CNTs, Pt-CNTs and Cu/Fe-CNTs. There was a significant change in the reaction products and in the selectivity towards the end-products. Particularly, especially for the MOF modified Pt based catalyst, there was an increase in the C-products and also a better selectivity towards higher C-products.

Moving to the studies on the electro-catalytic reduction of CO₂ in liquid phase cell, a similar set of electrodes were prepared. Initially, electrodes based on metal NPs of Cu, Fe, Pt, Ru and Co deposited on CNTs or carbon black were studied for their CO₂ reduction capability. The relative order of productivity in CO₂ electro-catalytic reduction in these series of electrodes was found to be different between the gas and liquid phase cells indicating the different reaction pathways. For liquid phase conditions, in terms of net C-products, catalytic electrodes based on Pt topped the class, closely followed by Ru and Cu, while Fe got the lowest position. The probable underlying reaction mechanism was also provided.

In order to improve further the performances of the CO₂ reduction in liquid phase conditions, a metal NPs size dependant study on the electro-catalytic reduction of CO₂ to fuels was carried out. This study was performed using electrodes based on metal NPs of Ru, Fe, Pt and Cu loaded on CNTs and then transferred on a gas diffusion layers (GDL). Varied sized metal NPs have been synthesized using different techniques: (i) impregnation route to achieve NPs in the size range of 10-50 nm; (ii) organometallic approach to synthesize uniform and ultrafine NPs in the size range of 1-5 nm (i.e., Fe NPs were synthesized through a novel synthesis route to attain 1-3 nm NPs); (iii) Nanowire (NW) top-down approach to obtain ultrafine copper metal NPs in the size range of 2-3.8 nm. Particularly, the novelty of nanowire approach is the ability to obtain very small metal NPs starting from the synthesis of Cu NWs and then transferring the Cu onto the carbon surface, taking advantage of the different inter-forces of between Cu NWs and the functional groups present on the partially oxidized CNT surface. Furthermore, unlike the case of organo-metallic approach, this approach allows a preparation under air avoiding the use of potentially demanding inert atmospheric conditions.

The enhancements in the fuel productivity were found to be 5-30 times higher for the smaller metal NPs obtained via organo-metallic route or nanowire route as compared to the larger metal NPs obtained via impregnation route. The results signify that the smaller sized metal NPs loading on the CNTs have a prevailing role in the catalytic performance and the selectivity towards different products. Moreover, the percentage of metal NPs loading was significantly reduced from 10 to 1-2 wt. % producing higher or equivalent fuels for small NPs as compared to the larger NPs. The reusability of the working electrodes and long reaction times (until 24 hours) were also probed.

A different set of electrodes based on nano-foams on metal foils, were also investigated to achieve further improvements in the electro-reduction of CO₂ to fuels. These nano-foams or dendrites were prepared by electrochemical deposition technique. Optimization studies on the deposition of these foams were performed initially to fix the set of preparation conditions. Moreover, voltage optimization study was performed using cyclic voltammetry and full CO₂ reduction tests to find the optimum voltage for the process. The nano-foam electrodes tested include Cu and Fe foams on Cu foil, Fe foil, Al foil, Inconel foil and Al grid/mesh. The enhancements in the fuel productivity for various foams were in the range of 2-10 times greater as compared to the highest net fuel productivity achieved using metal NPs doped carbon catalytic electrodes, from all the previous studies.

Various characterizations and analysis tools were used to analyse the catalysts qualitatively and quantitatively, which include Transmission Electron Microscopy (TEM), Scanning Electron Microscopy (SEM), Atomic Absorption Spectroscopy (AAS), X-ray diffraction (XRD), X-ray Photo-electron spectroscopy (XPS), and Brunauer-Emmett-Teller (BET). To determine the fuel productivities, Ion Chromatography (IC), Gas Chromatography-Mass Spectrometer (GC-MS), Gas Chromatography (GC) were used.

Keywords: CO₂ reduction; electrochemical cells; electro-catalysis; electrolyte-less conditions; gas phase; liquid phase; nano-foams (NFs); metal nano-particles (NPs); Cu nanowires (NWs); organo-metallic route; carbon nanotubes (CNTs); Metal-organic frameworks (MOFs); gas diffusion layers (GDL).

Abstract (Italian)

Alla luce del recente allarmante tasso di esaurimento delle riserve di combustibili fossili e al contemporaneo drastico aumento dei livelli di CO₂ nell'atmosfera, principale gas serra responsabile del riscaldamento globale e di cambiamenti climatici molto gravi, una delle priorità assolute nella ricerca a livello mondiale è quella di sfruttare il più possibile le fonti di energia rinnovabile. Una possibilità molto interessante è quella di realizzare un processo di riduzione della CO₂ a combustibili liquidi che sfrutti energie rinnovabili, quale quella solare, mediante dispositivi più comunemente noti come celle fotosintetiche artificiali o foglie artificiali o celle foto-elettro-catalitiche (PEC).

L'obiettivo principale di questo lavoro, è stato pertanto quello di condurre uno studio approfondito su due diversi sistemi elettrocatalitici di riduzione della CO₂ a prodotti liquidi con un più alto valore aggiunto, uno operante in fase gassosa (cioè in assenza di elettrolita al catodo) e uno operante in fase liquida. In particolare, è stata progettata e utilizzata nel processo di conversione della CO₂, un'innovativa cella in fase liquida operante su scala di laboratorio, sulla falsariga della cella in fase gas precedentemente sviluppata all'Università di Messina. Il lavoro è stato svolto principalmente presso il laboratorio CASPE/INSTM dell'Università degli Studi di Messina (Dipartimento di Ingegneria Elettronica, Chimica e Ingegneria Industriale). Un periodo di sei mesi è stato svolto invece, nel corso del secondo anno di dottorato, presso l'École supérieure de chimie, physique, électronique de Lyon (CPE Lyon). In tale periodo sono stati sintetizzati, mediante innovative tecniche di sintesi organometallica, materiali compositi da utilizzare come elettrocatalizzatori nel processo di riduzione della CO₂.

Sono state effettuate molteplici prove sperimentali utilizzando svariate tipologie di catalizzatori, sia in fase gas che in fase liquida, al fine di indagare la differente selettività, produttività e varietà di prodotti ottenuti. Il processo in fase liquida è infatti quello maggiormente studiato in letteratura, ma esistono alcune problematiche che devono essere superate per consentire un successivo semplice scale up. quali ad esempio, la scarsa solubilità della CO₂ e la tipologia di prodotti ottenuti (principalmente acido formico).

Lo scopo principale di questo lavoro è stato quello di preparare nuovi materiali a base di carboni dopati con metalli, catalizzatori questi molto diversi da quelli comunemente utilizzati nel processo di riduzione della CO₂ (generalmente metalli in bulk), e di testarli sia in fase gas (per sfruttare i vantaggi di questa condizione, quali ad esempio facile recupero dei prodotti e alta

qualità dei prodotti stessi) sia in fase liquida (per avere un miglior confronto con i dati ampiamente presenti in letteratura).

Per gli studi sulla riduzione elettrocatalitica della CO₂ nella cella operante in fase gassosa, sono stati preparati una serie di elettrodi (basati su nano particelle –NP- di Cu, Fe, Pt e Cu/Fe depositate su nanotubi di carbonio o carbon black e successivamente poste all'interfaccia tra una membrana di Nafion e uno strato a diffusione di gas –GDL-). I risultati ottenuti sono stati molto promettenti, sia in termini di tipologia di prodotti formati che di produttività. In fase gas (senza elettrolita) è stata osservata la formazione di prodotti $\geq C1$ quali etanolo, acetone e isopropanolo, in particolare utilizzando il Fe (seguito dal Pt), evidenziando che anche metalli non nobili possono essere usati in maniera efficiente in questo processo.

Per migliorare la produttività nella reazione di riduzione della CO₂, sono stati preparati elettrodi differenti, basati su coating con sostituti zeolitici imidazolici (SIM-1) tipo MOF. In particolare, i catalizzatori testati sono stati MOF modificati con Fe-CNT, Pt-CNT, e CuFe-CNT. E' stato osservato un cambiamento significativo in termini di produttività e anche di selettività verso i prodotti finali. Nel dettaglio, in particolare per il catalizzatore a base di MOF modificato con Pt, è stato osservato un aumento nei prodotti carboniosi e anche una selettività più alta verso prodotti con un più elevato numero di atomi di C.

Per quanto riguarda lo studio del processo di riduzione elettrocatalitica della CO₂ utilizzando la cella operante in fase liquida, sono state preparate tipologie di elettrodi simili ai precedenti. Inizialmente infatti, sono stati studiati elettrodi a base di nanoparticelle metalliche (Cu, Fe, Pt, Ru, Co) depositate su nanotubi di carbonio o carbon black. L'ordine relativo della produttività nella riduzione elettrocatalitica della CO₂ in questa serie di elettrodi, è però risultato essere diverso rispetto alla fase gassosa, indicando quindi un differente percorso di reazione. In termini di produttività totale, gli elettrodi a base di Pt hanno consentito di ottenere le migliori performance, seguiti da Ru e Cu, mentre il Fe ha dato risultati peggiori. Sulla base dei risultati sperimentali ottenuti, è stato inoltre ipotizzato un possibile meccanismo di reazione.

Successivamente, per cercare di migliorare ulteriormente le prestazioni nel processo di riduzione della CO₂ in fase liquida, è stato effettuato uno studio approfondito, volto ad indagare la dipendenza di tale processo dalle dimensioni delle nanoparticelle metalliche. A tale scopo sono stati utilizzati elettrodi a base di nanoparticelle metalliche (Ru, Fe, Pt e Cu) su nanotubi di carbonio (CNT) depositati su GDL. Sono state sintetizzate nanoparticelle metalliche di

diverse dimensioni utilizzando molteplici tecniche di sintesi: (i) impregnazione che ha consentito di ottenere NP di dimensioni comprese tra 10-50 nm; (ii) sintesi organometallica che ha consentito di ottenere NP uniformi e ultrafine con dimensioni comprese tra 1-5 nm. (ad esempio sono state sintetizzate NP di Fe di 1-3 P nm) (iii) sintesi mediante *nanowires* che ha consentito di ottenere NP di rame ultrafine con dimensioni comprese tra 2-3,8 nm.

In particolare, la novità dell'approccio mediante *nanowires* sta nella possibilità di ottenere particelle di dimensioni molto piccole sintetizzando inizialmente i Cu NWs, mettendoli poi a contatto con il supporto carbonioso e facilitandone il suo trasferimento, ciò grazie alle forze intermolecolari di attrazione dei gruppi funzionali presenti sui CNT parzialmente ossidati. Inoltre, a differenza della sintesi organometallica, tale approccio permette di condurre le reazioni in aria e non in atmosfera inerte.

I valori di produttività ottenuti sono stati 5-30 volte più alti utilizzando nanoparticelle metalliche più piccole (ottenute via *nanowires* o mediante sintesi organometallica) rispetto alle nanoparticelle metalliche più grandi (ottenute per impregnazione). I risultati sperimentali indicano pertanto che le NP di dimensioni più piccole hanno un ruolo fondamentale nelle performance catalitiche. Inoltre, il carico di NP metalliche è stato significativamente ridotto dal 10% al 1-2% in peso consentendo di ottenere, per le NP più piccole, una produttività equivalente o addirittura superiore rispetto alle nanoparticelle più grandi. In seguito, è stato effettuato anche uno studio sul possibile riutilizzo degli elettrodi di lavoro e sulla disattivazione per tempi di reazione più lunghi.

E' stata infine preparata una diversa tipologia di elettrodi a base di *nano-foams* su lastre metalliche, al fine di ottenere un ulteriore miglioramento nel processo di riduzione elettrocatalitica della CO₂. Le *nano-foams* o dendriti, sono state preparate mediante la tecnica di deposizione elettrochimica ed è stato effettuato uno studio preliminare di ottimizzazione, al fine di determinare le condizioni di sintesi più adatte.

In aggiunta, è stato eseguito uno studio specifico per ottimizzare il valore di Voltaggio da utilizzare nelle prove catalitiche, mediante sia test di voltammetria ciclica che test completi di riduzione della CO₂. Sono stati testati *nano-foams* a base di Cu e Fe depositati su fogli di Cu, Fe, Al, di Inconel e su una griglia di Al. L'aumento nella produttività usando queste tipologie di elettrodi, è stata nell'ordine di 2-10 volte rispetto alla massima produttività ottenuta utilizzando NP metalliche su materiali carboniosi.

Svariate tecniche analitiche sono state poi utilizzate per caratterizzare in modo approfondito i materiali preparati tra cui, microscopia elettronica a trasmissione (TEM), microscopia elettronica a scansione (SEM), spettroscopia ad assorbimento atomico (AAS), diffrazione a raggi X (XRD), spettroscopia fotoelettronica a raggi X (XPS), determinazione dell'area superficiale mediante metodo Brunauer-Emmett-Teller (BET). La determinazione dei prodotti di reazione è stata effettuata invece mediante cromatografia ionica (IC), gas cromatografia con rivelatore a spettrometria di massa (GC-MS), gas cromatografia (GC) con rivelatore a termo conducibilità (TCD).

Parole chiave: Riduzione della CO₂; celle elettrochimiche; elettro-catalisi; assenza di elettrolita; fase gassosa; fase liquida; nano-schiume (NFs); nano-particelle (NPs); nano-fili (NWs); sintesi organo-metallica; nanotubi di carbonio (CNT); strutture metallo-organiche (MOF); elettrodi a diffusione dei gas (GDE).

Abstract (French)

Compte tenu du récent taux alarmant d'épuisement des réserves de combustibles fossiles et de l'augmentation drastique des niveaux de CO₂ dans l'atmosphère qui a conduit au réchauffement de la planète et à des changements climatiques sévères, l'exploitation de toutes sortes d'énergies renouvelables a été la Parmi les principales priorités de la recherche Champs à travers le monde. L'une des nombreuses voies de ce genre est la réduction du CO₂ aux combustibles utilisant des énergies renouvelables, plus communément appelées cellules photosynthétiques artificielles ou feuilles artificielles ou cellules photoélectro-catalytiques (PEC).

L'objectif principal de ce travail était de réaliser des études approfondies sur les différents systèmes de réduction électro-catalytique du CO₂, à savoir les cellules sans électrolyte (phase gazeuse) et les cellules électrolytiques (phase liquide). Dans ce processus, nous avons conçu une nouvelle cellule en phase liquide à échelle de laboratoire sur les lignes similaires de la cellule de phase gazeuse de modèle précédemment modélisée. Des essais expérimentaux sur la réduction du CO₂ ont été réalisés sur différents types de catalyseurs dans les deux cellules afin de comprendre la sélectivité, la productivité et les produits de réaction obtenus. L'obtention de résultats de test dans les deux cellules nous a permis d'effectuer une comparaison décente avec les résultats de réduction électro-catalytique de CO₂ existants dans la littérature.

Des essais expérimentaux ont été réalisés sur différents types de catalyseurs à la fois dans les cellules en phase gazeuse et en phase liquide pour comprendre la sélectivité, la productivité et les produits de réaction obtenus. La phase liquide, en fait, a été le processus le plus étudié dans la littérature, mais certaines questions liées principalement à la solubilité du CO₂ et aux types de produits formés (c'est-à-dire principalement l'acide formique) n'ont jamais été autorisées à franchir le stade de l'échelle du laboratoire. L'objectif général de ce doctorat était de préparer de nouveaux substrats de nanocarbone dopés par des métaux, qui sont très différents par rapport aux couches en vrac métalliques conventionnelles utilisées comme électrocatalyseurs dans la réduction de CO₂, et de les tester en phase gazeuse (pour profiter de ces conditions, Une récupération facile et une qualité améliorée des produits) et en phase liquide (pour une meilleure comparaison avec les conditions typiquement adoptées dans la littérature).

Pour les études sur la réduction électro-catalytique du CO₂ en phase gazeuse, une série d'électrodes (à base de nanoparticules de Cu, Fe, Pt et CuFe déposées sur des nanotubes de carbone ou de noir de carbone puis placées à l'interface entre une membrane Nafion et Une électrode à couche de diffusion de gaz). Les résultats démontrent le type divers de produits formés et leurs productivités. Dans des conditions sans électrolyte, la formation de produits $\geq C1$ tels que l'éthanol, l'acétone et l'isopropanol a été observée la plus élevée étant pour Fe et suivie de près par Pt. Pour améliorer les productivités de la réduction du CO₂, un ensemble différent d'électrodes a été préparé sur la base de revêtements MOF de type imidazolate de type zéolitique substitué (SIM-1) lors d'un séjour au CPE Lyon et à l'Institut de recherches sur la catalyse et l'environnement de Lyon (IRCELYON). Les catalyseurs testés étaient Fe-CNT, Pt-CNT et CuFe-CNT basés sur MOF. Il y a eu un changement significatif dans les produits de réaction et aussi, la sélectivité vis-à-vis des produits finaux. Pour le catalyseur à base de Pt modifié, MOF, il y avait une augmentation des produits C et également une sélectivité différente tandis que pour le catalyseur à base de Fe, il y avait une légère diminution des produits C.

En se reportant aux études sur la réduction électro-catalytique du CO₂ dans une cellule en phase liquide, un ensemble similaire d'électrodes a été préparé afin d'obtenir une bonne comparaison des résultats dans les expériences en phase gazeuse. Initialement, des électrodes à base de nanoparticules métalliques (Cu, Fe, Pt, Ru, Co) déposées sur des nanotubes de carbone ou du noir de carbone ont été étudiées pour leur capacité de réduction du CO₂. L'ordre relatif de productivité dans la réduction électrocatalytique de CO₂ dans ces séries d'électrodes a été trouvé différent entre les cellules en phase gazeuse et en phase liquide indiquant les différentes voies de réaction. Pour les conditions de phase liquide, en termes de produits C nets, les électrodes catalytiques à base de Pt sont en tête de la catégorie, suivies de près par Ru et Cu, tandis que Fe a obtenu la position la plus basse. Le mécanisme réactionnel sous-jacent probable a également été fourni.

Afin d'améliorer encore les performances de la réduction du CO₂ dans les conditions de phase liquide, une étude de la nanoparticules métalliques (NPs) dépendant de la taille de la réduction électro-catalytique du CO₂ aux combustibles a été réalisée. Ceci a été réalisé à l'aide d'électrodes à base de nanoparticules métalliques (Ru, Fe, Pt et Cu) chargées sur les nanotubes de carbone (CNT) transférés sur les couches de diffusion gazeuse (GDL). On a synthétisé des nanoparticules de métal de différentes tailles en utilisant différentes techniques de synthèse: (i)

l'itinéraire d'imprégnation pour obtenir des NP dans la plage de tailles de 10 à 50 nm; (Ii) Approche organométallique pour synthétiser des NPs uniformes et ultrafines dans la plage de tailles de 1-5 nm. Fe ont été synthétisés par une nouvelle voie de synthèse et des conditions pour atteindre des NP de 1 à 3 nm. (Iii) Approche de haut en bas de Nanowire pour obtenir des NP métalliques de cuivre ultrafin dans la plage de taille de 2-3,8 nm. En particulier, la nouveauté de l'aide de nanofils est la capacité à obtenir des particules de très petite taille d'abord la synthèse du Cu NFs, puis de les mettre en contact avec le support carboné et de faciliter son transfert, cela grâce à des forces d'attraction intermoléculaires des groupes fonctionnels présent sur le CNT partiellement oxydée. En outre, contrairement à la synthèse organométallique, cette approche permet d'effectuer les réactions dans l'air et non pas dans une atmosphère inerte.

Les améliorations de la productivité du combustible ont été trouvées être au moins 5 à 30 fois plus élevées pour les NP métalliques de plus petite taille obtenus par voie organométallique ou par nanofil, par rapport aux NP métalliques plus grands obtenus par voie d'imprégnation. Les résultats indiquent que les NP métalliques de plus petite taille chargés sur les CNT jouent un rôle prédominant dans la performance catalytique et la sélectivité vis-à-vis de différents produits. En outre, le pourcentage de charge de NP métalliques a été réduit de façon significative de 10% à 1-2% en poids, produisant des carburants plus élevés ou équivalents pour de petites NP en comparaison avec les NP plus grandes. De plus, comme on a observé clairement la productivité en H₂ qui a augmenté de nombreux facteurs pour les NP plus petits sur les plus grandes NP. La réutilisabilité des électrodes de travail et les longs temps de réaction ont également été sondés.

Un ensemble différent d'électrodes à base de nano-mousses sur des feuilles métalliques a également été étudié afin d'obtenir des améliorations beaucoup plus importantes de l'électro-réduction de CO₂ aux carburants. Ces nano-mousses ou dendrites ont été préparées par une technique de dépôt électrochimique. Des études d'optimisation sur le dépôt de ces mousses ont été effectuées initialement pour fixer l'ensemble des conditions de préparation. De plus, une étude d'optimisation de la tension a été réalisée en utilisant la voltamétrie cyclique et des tests de réduction de CO₂ complets pour fixer une tension optimale pour les réactions. Les électrodes nano-mousses testées incluent (mousses Cu, Fe sur feuille Cu, feuille Fe, feuille Al, feuille Inconel et grille Al). Les améliorations de la productivité du combustible pour diverses mousses se situaient dans la plage de 2 à 10 fois par rapport à la productivité nette de combustible la plus élevée obtenue en utilisant des électrodes catalytiques en carbone dopé par des NP métalliques.

Différentes caractérisations et outils d'analyse ont été utilisés pour analyser les catalyseurs qualitativement et quantitativement qui incluent la microscopie électronique à transmission (TEM), la microscopie électronique à balayage (SEM), la spectroscopie d'absorption atomique (AAS), la diffraction des rayons X (XRD) La spectroscopie électronique (XPS) et Brunauer-Emmett-Teller (BET) et pour déterminer les productivités des combustibles, chromatographie ionique (IC), chromatographie gazeuse-spectromètre de masse (GC-MS), chromatographie gazeuse.

Mots-clés: Réduction du CO₂; des cellules électrochimiques; l'électro-catalyse; absence d'électrolyte; phase gazeuse; phase liquide; nano-mousses (NFs); nano-particules (NPs); nano-fils (NWs); synthèse organo-métallique; nanotubes de carbone (CNT); structures métallo-organiques (MOF); une électrode de diffusion de gaz (GDE).

TABLE OF CONTENTS

Dedication	iii
Epigraph	iv
Acknowledgements	v
Abstract	viii
Table of Contents	xx
List of Figures	xxvi
List of Tables	xxx

<u>CHAPTER</u>	<u>PAGE NO</u>
1. General Introduction	1
1.1 Energy.....	1
1.1.1. Global energy perspective.....	1
1.1.2. Energy Sources.....	1
1.1.3. Global climate change and CO ₂	1
1.2 Solar Fuels – A key to the global challenge.....	5
1.2.1. Photo-catalysis (HER reaction).....	6
1.2.2. Electro-catalysis (CO ₂ reduction).....	8
1.2.2.1. General terms reported in EC CO ₂ reduction.....	9
1.2.3. Thermodynamics and Reaction pathways.....	10
1.2.4. Catalysts.....	12
1.3 Global research outlook on CO ₂ reduction.....	13
1.4 Thesis (main aim, scope and chapter goals).....	15
1.5 References.....	16

2. CO₂ electro-catalytic reduction in electrolyte-less conditions (Gas phase)	23
2.1 Introduction.....	23
2.1.1. State of the art.....	23
2.1.1.1. Preparation of the electro-catalytic material.....	23
2.1.1.2. Assembling of the electrodes.....	25
2.1.1.3. Gas phase cell model and the testing of the electrodes.....	25
2.1.1.4. Importance of nano-carbon based substrates.....	26
2.1.1.5. Fuel productivity and selectivity.....	27
2.1.2. Scope of the chapter.....	28
2.2 Experimental.....	28
2.2.1. SIM 1 - MOF synthesis.....	28
2.2.2. Working electrode configuration (final template).....	29
2.3 Results and Discussions.....	30
2.3.1. Characterization.....	30
2.3.1.1. SEM Morphological Measurements.....	31
2.3.2. Electro-catalytic CO ₂ reduction in Gas phase.....	31
2.3.2.1. Voltage profile.....	31
2.3.2.2. Fuel Productivity.....	32
2.4 Conclusions.....	33
2.5 References.....	34
ANNEX ²	36

3. Design and performance of a novel cell for CO₂ electro-reduction (Liquid phase).....	38
3.1 Introduction.....	38
3.1.1. State of the art.....	38
3.1.2. Scope of the chapter.....	39
3.2 Experimental.....	40
3.2.1. Preparation of the Electrodes.....	40
3.2.2. Basic conditions of the cell.....	43
3.3 Results and Discussions.....	43
3.3.1. Design and engineering of the liquid phase electro-catalytic Cell.....	43
3.3.1.1. Modelling and working principles.....	43
3.3.1.2. Design Challenges.....	46
3.3.2. Characterization.....	47
3.3.2.1. Structural Analysis.....	47
3.3.2.2. TEM Morphological Measurements.....	48
3.3.2.3. Surface Analysis.....	51
3.3.2.4. Quantitative and physical characterizations.....	52
3.3.2.5. Current Profile.....	53
3.3.3. Electro-catalytic CO ₂ reduction.....	54
3.3.3.1. Fuel Productivity.....	54
3.3.4. Mechanism.....	57
3.4 Conclusions.....	60
3.5 References.....	62
ANNEX ³	66

4. Size controlled nanoparticles for liquid phase CO₂ electro-reduction.....	70
4.1 Introduction.....	70
4.1.1. State of the art (Organo-metallic).....	70
4.1.2. State of the art (Nanowire).....	71
4.1.3. Scope of the chapter.....	72
4.2 Experimental.....	72
4.2.1. Synthesis of metal nanoparticles via organo-metallic route.....	72
4.2.1.1. Pt nanoparticle synthesis.....	72
4.2.1.2. Ru nanoparticle synthesis.....	73
4.2.1.3. Fe nanoparticle synthesis.....	74
4.2.2. Synthesis of metal nanoparticles via nanowire route.....	74
4.2.3. Preparation of the working electrodes.....	76
4.3 Results and Discussions.....	77
4.3.1. Organo-metallic route.....	77
4.3.1.1. Synthesis and Characterization.....	77
4.3.1.1.1. Structural Analysis.....	77
4.3.1.1.2. TEM Morphological Measurements.....	78
4.3.1.1.3. Surface Analysis.....	81
4.3.1.1.4. Quantitative and physical characterizations.....	82
4.3.1.1.5. Current profile.....	83
4.3.1.2. Electro-catalytic CO ₂ reduction.....	84
4.3.1.2.1. Fuel Productivity.....	84
4.3.2. Nanowire route (Cu NWs to get Cu NPs).....	86
4.3.2.1. Synthesis and Characterization.....	86
4.3.2.1.1. Structural Analysis.....	86
4.3.2.1.2. TEM Morphological Measurements.....	87

4.3.2.1.3. Surface Analysis.....	89
4.3.2.1.4. Quantitative and physical characterizations.....	90
4.3.2.1.5. Current profile.....	91
4.3.2.2. Electro-catalytic CO ₂ reduction.....	91
4.3.2.2.1. Fuel Productivity.....	91
4.4 Conclusions.....	95
4.5 References.....	96
ANNEX ⁴	99
5. Nano foams for liquid phase CO₂ electro-reduction.....	102
5.1 Introduction.....	102
5.1.1. State of the art.....	102
5.1.2. Electro-chemical deposition	103
5.1.3. Scope of the chapter.....	103
5.2 Experimental.....	104
5.2.1. Synthesis of metal nano-foams via electro-chemical deposition.....	104
5.2.1.1. Cu nano-foam synthesis.....	104
5.2.1.2. Fe nano-foam synthesis.....	105
5.2.1.3. Metal foils.....	106
5.3 Results and Discussions.....	106
5.3.1. Characterization.....	106
5.3.1.1. SEM Morphological Measurements.....	106
5.3.1.2. Surface Analysis.....	110
5.3.1.3. Structural Analysis.....	110
5.3.1.4. Energy Dispersive X-ray spectroscopy (EDX).....	111
5.3.1.5. Quantitative discussion.....	112

5.3.1.6. Electro-catalytic CO ₂ reduction.....	112
5.3.1.6.1. Current profile.....	112
5.3.1.6.2. Voltage Optimization.....	113
5.3.1.6.3. Fuel Productivity.....	113
5.4 Conclusions.....	116
5.5 References.....	117
ANNEX ⁵	119
6. General conclusions and perspectives.....	123
7. Curriculum vitae.....	127

List of Figures

Fig. 1.1 Global carbon emissions from fossil fuels.....	3
Fig. 1.2 Global CO ₂ concentrations over the years.....	3
Fig. 1.3 Global CO ₂ concentrations predictions for the next hundred years.....	4
Fig. 1.4 Schematic representation of photo-chemical water splitting.....	7
Fig. 1.5 Schematic representation of photo-electro-chemical water splitting.....	8
Fig. 1.6 Reaction pathways of CO ₂ reduction to oxalate, CO, formate on inert electrodes.....	11
Fig. 1.7 Reaction pathways of CO ₂ reduction to different products on transition metal and molecular catalytic electrodes.....	11
Fig. 1.8 A graphical view on various categories of electrocatalysts of CO ₂ reduction.....	13
Fig. 2.1 (a) Scheme of the apparatus for electrolyte-less cell tests of CO ₂ reduction with the electro-catalyst in contact with a gaseous flux of CO ₂ . (b) Photo of the cell; in the inset view of the electrode and GDL.....	26
Fig. 2.2 Scheme showing MOF synthesis and transfer onto GDL.....	29
Fig. 2.3 Scheme showing the configuration of the final electrode template.....	29
Fig. 2.4 SEM image of the GDL with MOF cross-sectional view.	30
Fig. 2.5 SEM images showing the deposition of the MOFs crystals on the fibres of GDL.....	31
Fig. 2.6 SEM image showing the thickness of the MOF layer and the GDL.....	31
Fig. 2.7 Voltage profiles for MOF modified Pt, Fe – CNTs gas phase reaction.....	32
Fig. 2.8 H ₂ and CO productivity in (μmol/min) vs Time (min)	32
Fig. 3.1 A Schematic showing treating CNTs to obtain oxygen functionalities.....	41
Fig. 3.2 A Schematic showing transfer of metal NPs onto the CNTs from NPs/NWs in solvent and coating metal NP doped CNT based INK on GDL to make the working electrode.....	42
Fig. 3.3 Schematic illustration of the GDE-type electrodes utilized for the CO ₂ electrochemical reduction. Image on the left shows the full gas-diffusion electrode (GDE), while images on the	

right are scanning electron microscopy images of the side at contact with the membrane and of the side at contact with gas phase (CO ₂) or the electrolyte in which CO ₂ is bubbled.....	44
Fig. 3.4 Graphical representation of the experimental setup for liquid phase cell for CO ₂ reduction to fuels.....	45
Fig. 3.5 XRD patterns (Impregnation route, 10 wt. % of metal) for (a) bare CNTs, (b) Fe-CNT, (c) Cu-CNT, (d) Ru-CNT, (e) Pt-CNT.....	47
Fig. 3.6 TEM image showing (a) Pt NPs on CNT, (b) Fe NPs on CNT, (c) Cu NPs on CNT, (d) Ru NPs on CNT, (e) Co NPs on CNT via Impregnation Route.....	49, 50, 51
Fig. 3.7 XPS data for bare CNT _{ox} - (a) illustration of the C1s and respective deconvolution spectra, (b) XPS data illustration of the O1s and respective deconvolution spectra.....	51
Fig. 3.8 N ₂ adsorption/desorption isotherms for bare CNT _{ox} and Cu-CNT _{ox}	53
Fig. 3.9 Current profiles for Cu, Fe, Pt, and Ru loaded CNTs via Impregnation Route.....	53
Fig. 3.10 Schematic of the reaction mechanism of CO ₂ reduction to formic acid.....	58
Fig. 3.11 N ₂ adsorption/desorption isotherms for CNT _{ox} , Co, Pt, Fe, Cu, Ru NPs on CNT _{ox}	67
Fig. 3.12 Standard three-electrode cell configuration.....	68
Fig. 4.1 Schematic showing organo-metallic synthesis of Pt NPs from Pt(dba) ₂	73
Fig. 4.2 Schematic showing organo-metallic synthesis of Ru NPs from Ru(cod)(cot).....	73
Fig. 4.3 Schematic showing organo-metallic synthesis of Fe NPs from Fe(acac) ₃	74
Fig. 4.4 A Schematic with the process steps involved in the Cu Nanowires synthesis.....	75
Fig. 4.5 A Schematic showing formation of Cu NPs from Cu NWs on the CNTs.....	75
Fig. 4.6 Working electrode preparation by depositing metal NPs + CNT based INK on GDL..	76
Fig. 4.7 XRD (OM route) for (a) bare CNTs, (b) Fe-CNT, (c) Ru-CNT, (d) Pt-CNT.....	78
Fig. 4.8 TEM image showing Fe NPs colloidal solution via OM route (1 – 3.2 nm).....	79
Fig. 4.9 TEM image showing Pt, Fe, and Ru NPs on CNT via Organo metallic route (0.9 nm - 5.6 nm) and STEM image showing the uniformity of metal NP loading on the CNTs.....	80

Fig. 4.10 (a, c, e) XPS wide scan survey spectra for Pt, Fe, Ru on CNT catalyst (OM Route) ; (b, d, f) High-resolution spectrum of the Pt 4f, Fe 2p, Ru 3p doublets and their respective de-convolution spectra..	81
Fig. 4.11 N ₂ adsorption/desorption isotherms for Ru NPs-CNT _{ox} (a) OM, (b) ImR routes.....	83
Fig. 4.12 Current profiles for OM route (a) Fe CNT _{ox} , (b) Pt CNT _{ox} , (c) Ru CNT _{ox}	83
Fig. 4.13 XRD patterns (a) bare CNTs, (b) Cu-CNT (ImR route), (c) Cu-CNT (NW route)....	87
Fig. 4.14 TEM image showing (a) Cu NPs on CNT for ImR route (5 nm - 16 nm), (b) Cu nanowires before deposition onto CNTs.....	88
Fig. 4.15 TEM image showing Cu NPs on CNT via NW route (2 nm - 3.8 nm) and STEM image showing the uniform dispersion of the Cu NPs on the CNT.	88
Fig. 4.16 (a) XPS wide scan survey spectra for Cu/CNT catalyst, (b) XPS data illustration of the C1s and respective deconvolution spectra, (c) High-resolution spectrum of the Cu 2p doublet and respective de-convolution spectra, (d) XPS data illustration of the O1s and respective de-convolution spectra.	89
Fig. 4.17 N ₂ adsorption/desorption isotherms for Cu NPs-CNT _{ox} (a) NW, (b) ImR route.....	90
Fig. 4.18 Current profiles for Cu CNT _{ox} (a) NW route, (b) 10%, ImR, (c) 1%, ImR route.....	91
Fig. 4.19 Time dependence vs productivity of formic acid, acetic acid and H ₂ for Cu NPs on CNT _{ox} (a) 1%, ImR route, (b) 1%, NW route.	93
Fig. 4.20 N ₂ adsorption/desorption isotherms for Pt, Fe, NPs on CNT _{ox} (OM & ImR routes).	100
Fig. 5.1 Schematic showing Electro-deposition of Cu on metal/semi-conductor.....	102
Fig. 5.2 Schematic of the Electro-deposition of metal to nano-foam electrodes.....	103
Fig. 5.3 SEM image (top view) of the Cu NF on Cu foil with deposition time (a) 1 min, (b) 4 min.	105
Fig. 5.4 SEM images (top view) of the Cu NF on Cu metal foil with deposition t = 2 min.....	106
Fig. 5.5 SEM images of Cu NF on Cu (2 min) - dendrite structures.	106
Fig. 5.6 SEM images (cross-section view) of Cu NF on Cu (2 min).	107

Fig. 5.7 SEM images of Cu NF on Fe foil (2 min) (a) top view, (b) dendrite close-up.....	107
Fig. 5.8 SEM images of Cu NF on Al grid (2 min) (a) top view, (b) cross-section view.....	108
Fig. 5.9 SEM image of Fe NF on Al foil (deposition time = 2 min).	108
Fig. 5.10 (a) XPS wide scan survey spectra for Cu nano-foam on Cu (b) High-resolution spectrum of the Cu 2p doublets.	109
Fig. 5.11 XRD pattern of the Cu nano-foam with base substrate as Cu foil.....	110
Fig. 5.12 EDX spectra of the Cu nano-foam with base substrate as Cu foil.....	110
Fig. 5.13 Current profiles for (a) Cu NF on Cu, (b) Cu Foil, (c) Cu NF on Inconel, (d) Cu NF on (Al grid + Cu foil).	111
Fig. 5.14 Time dependence vs productivity of formic acid, acetic acid, CO and H ₂ for (a) Cu NF on Inconel, (b) Cu NF on Al grid + Cu NF on Cu foil.	114
Fig. 5.15 EDX spectra for (a) Cu NF on Fe foil; (b) Cu NF on Al grid; (c) Fe NF on Al grid, (d) Cu foil (polished); (e) Inconel foil.	119, 120

List of Tables

Table 1.1	CO ₂ reduction potentials for various CO ₂ reduction reactions products.....	12
Table 1.2	The performance report for various electro-catalysts in CO ₂ reduction.....	14
Table 2.1	Properties of commercial GDL and CNTs.....	24
Table 2.2	Productivity for the CO ₂ EC reduction in gas phase cell (Units: μmoles per hr).....	27
Table 2.3	Productivity for the CO ₂ EC reduction in gas phase cell (Units: μmoles per hr).....	33
Table 3.1	A review of the various conditions and the results of CO ₂ electro-reduction.....	39
Table 3.2	Properties of commercial GDL and CNTs.....	40
Table 3.3	Detailed size distributions of Pt, Fe, Cu, Ru and Co NPs via Impregnation routes...	48
Table 3.4	AAS and BET characteristics of Pt, Fe, Cu, and Ru NPs via Impregnation routes...	52
Table 3.5	Productivity values for the CO ₂ EC reduction in liquid phase cell.....	54
Table 3.6	Productivity values for the CO ₂ EC reduction in gas phase cell.....	55
Table 3.7	Comparison of types of products obtained in liquid and gas phase operations in CO ₂ electro-catalytic reduction.....	56
Table 4.1	Detailed size distributions of Pt, Fe and Ru NPs via organo-metallic route.....	79
Table 4.2	Textural characteristics of the electro-catalysts by BET method.	82
Table 4.3	Productivity for the CO ₂ EC reduction in liquid phase cell (Units: μmoles/hr).....	84
Table 4.4	Approximate calculated no. of surface atoms and the fraction of surface atoms.....	86
Table 4.5	Detailed size distributions of Cu-CNT via nanowire (NW) and ImR routes.....	88
Table 4.6	Textural characteristics of the electro-catalysts by BET method.....	91
Table 4.7	Products obtained in the CO ₂ electro-chemical reduction in liquid phase cell.....	92
Table 4.8	TOF values (μmol.s ⁻¹ .cm ⁻²) on Cu CNT (NW and ImR routes) based electrodes, in comparison with TOF values reported by Kuhl et al. [38] (*) for Cu foil electrode.....	94
Table 5.1	A review of the results of CO ₂ EC reduction using metals and foams catalysts.....	101
Table 5.2	Productivity for the CO ₂ electro-chemical reduction in liquid phase cell for Cu foil electrodes for different voltages (Units: μmoles per hr).....	112
Table 5.3	Productivity for the CO ₂ electro-chemical reduction in liquid phase cell for nano-foam electrodes (Units: μmoles per hr).	113

CHAPTER 1

1. General Introduction

1.1. Energy

1.1.1. Global energy perspective

World Energy consumption is increasing at an enormous rate, which reached to an average power consumption of 12.3 terawatts (TW) in 2013 (equivalently 1.1×10^{14} kWh or units) as compared to ~ 6 TW in 1980 ^[1]. This extensive rise in the energy consumption depends on various factors: population rise, standards of living, industrial growth, advanced technologies, etc. For instance, the world population has risen from 4.4 billion (1980) to 7.4 billion (current, 2016) ^[2] and is expected to reach 11.2 billion by 2100 ^[3], in-turn resetting the expected global energy need to ~ 43 TW ^[4]. Currently, the global energy dependency in non-renewables or fossil fuels is about 78.1 %, nuclear energy of about 2.7 % and the rest 19.2 % is renewable energy.

1.1.2. Energy Sources

The global energy sources can be broadly classified into: (i) renewable and (ii) non-renewable.

Renewable energy can be defined as the source of energy that can be replenished in an acceptable amount of time. This includes solar energy, hydro-power, wind energy, biofuels, biomass, tidal & wave energy and geo-thermal. In 2016, the individual contributions account for 8.9 % biomass (traditional), 4.2 % heat energy (geo-thermal, modern biomass, solar heat), 3.9 % hydro-electricity and 2.2 % electricity (wind, solar, geo-thermal, biomass) ^[4-6].

Non-renewable energy can be defined as the source of energy that cannot be replenished at a sufficient rate (a meaningful human-time frame) for sustainable usage. This includes earth minerals and ores, fossil fuels (coal, oil, natural gas, shale gas, etc) and also groundwater in specific aquifers. In 2016, the individual contributions account for 30 % coal, 33 % oil, 24 % natural gas and 2.7 % nuclear energy ^[4, 6].

1.1.3. Global climate change and CO₂

Large and critical changes in climate have happened very quickly in the last years, effecting the global environmental cycle. The climate change can be due to variations in nature such as

biotic processes, solar radiation, plate tectonics and volcanic eruptions. However, in recent times this has been effected by unaddressed and unchecked human activities, which have caused the serious phenomenon called global warming. This term refers to the rise in average surface temperatures on Earth (the global temperature increased by 0.8 °C in this century ^[7]), thus effecting entire planet climatic conditions, agriculture, aquatic life, plant life and human beings alike.

Global warming is mainly due to the human use of fossil fuels and other human activities, which release continuously into the atmosphere enormous amounts of greenhouse gases. The main greenhouse gas is CO₂ (81 %), other gases responsible for global warming are methane (11 %), nitrous oxide (6 %) and fluorinated gases (3 %) ^[8].

The gases trap heat within the atmosphere, causing various effects on ecosystems, including polar ice-cap melting (increasing the sea level, contributing to greater storm damage), warming ocean temperatures (causing stronger and more frequent storms), severe weather events (leading to floods and other damage), droughts and more severe wildfires. The climate change is thus a complex process depending on various factors as discussed above and each of these factors (natural causes) adjusting itself to the unaccounted add-on factor (greenhouse gases), thus changing the climate for good and making it permanently damaged.

CO₂ gas emissions is one of the major role-playing factor in the global warming. CO₂ plays a vital role in the plant life and algae (through photosynthesis), which have evolved from millions of years to form an efficient and renewable process for reducing CO₂. The sudden rise in the CO₂ levels in addition to rising temperatures does not give the slightest chance for evolution to react (as it is a slow process). The CO₂ emissions by various systems in the world are as follows: 91 % from burning fossil fuels and cement production, of which only about 50 % is recycled via absorption by land and ocean and photosynthetic process ^[9, 10]. The rest remains accumulated in the atmosphere. As the world energy demand keeps rising, the CO₂ emission and accumulation increase. *Fig. 1.1*, shows the global carbon emissions data.

As discussed above, the CO₂ concentration in the atmosphere continuously increased for the past two centuries and reached a current concentration of 401.6 ppm (Oct. 2016), i.e. it increased by more than 33 % in the past two centuries. *Fig. 1.2*, shows the graphical representation of the changes in the CO₂ concentrations over the time ^[11]. These huge level of CO₂ is leading to several environmental calamities, as specified above: climate change ^[12], rise

in global temperature in turn leading to sea level rising [13] and irreversible damage to ecological cycles. This has to be addressed before it crosses a threshold level, a point later cannot be corrected or reverted to reset the environmental conditions to a safe, life supporting level. The prediction of CO₂ concentration shown in Fig. 1.3, shows the drastic levels of CO₂, which in turn can lead to a temperature rise of 1 to 5.5 °C, thereby leading to a sea level rise of 20 to 90 cm [14]. The Fig. 1.3, (A1, A2, B1, B2) encompass four combinations of demographic change, social and economic development, and broad technological developments [14]. Two sub-scenarios of the A1 family (A1FI, A1T) explicitly explore alternative energy technology developments, holding the other driving forces constant, each with an illustrative scenario and IS92a is the scenario predicted in 1992 [14].

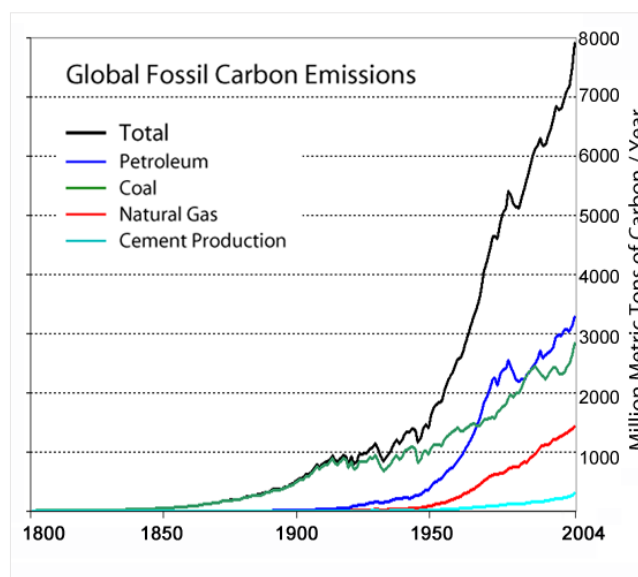


Fig. 1.1 Global carbon emissions from fossil fuels [9].

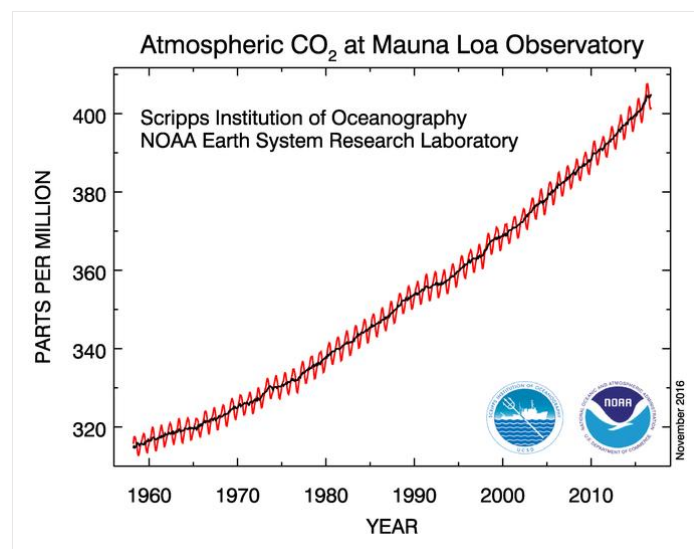


Fig. 1.2 Global CO₂ concentrations over the years [11].

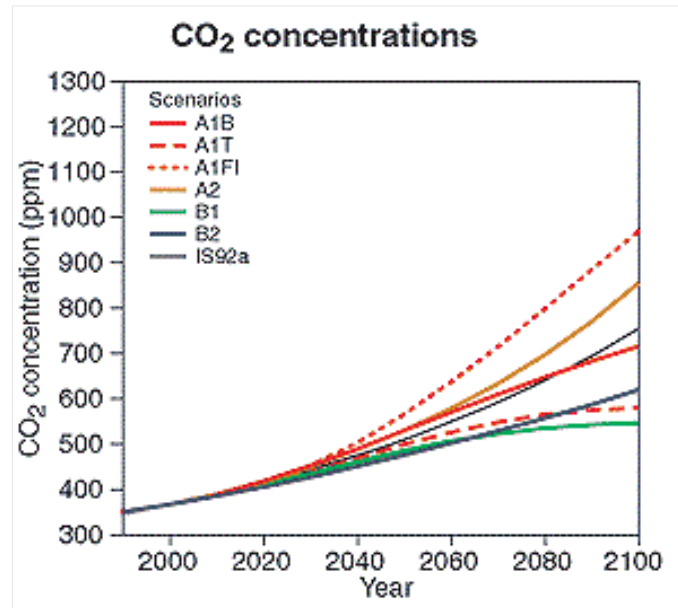


Fig. 1.3 Global CO₂ concentrations predictions for the next hundred years [14].

Various strategies for decreasing CO₂ emissions or accumulation via re-looping CO₂ into a renewable fuel production cycle or via capturing and burying large amounts of CO₂, are already in action. Burying CO₂ is a currently viable plan but the long term consequences are still unknown. Alternatively, the excess CO₂ (cheap and inexhaustible source of carbon) can be used as a starting material to synthesize or produce various chemicals or fuels by reduction methodologies, similar to the natural photosynthetic systems. This is sometimes referred to artificial leaves or photosynthesis. However, like all endothermic processes, this process of CO₂ reduction to fuels, also needs some amount of energy to drive and sustain the reaction. Moving closer to the well-established process in the nature, we can embed solar energy as a renewable source for supplying the necessary energy needed for the reduction. Solar energy is one of the most abundant energy source on this planet. The total solar energy hitting the earth in one hour is more than the net global annual energy consumption [15]. Due to the intermittency of insolation and the disparity of intensity over the globe surface, solar energy needs to be stored to become a major primary energy source. Converting solar energy into carbon based fuels through atmospheric CO₂ reduction, appears as an appealing solution for the future of energy demands. Conversion of CO₂ using renewable energy sources can be achieved through various catalytic processes (homogenous, heterogeneous, bio, photo, electro, and photo-electro) [16-38]. In general terms, it is possible to develop a multistep approach, in which electrical energy is generated using renewable energy sources, and then, H₂ is generated in electrolyzers using this electrical energy. Finally, H₂ is used in catalytic processes, either

homogeneous or heterogeneous, to convert CO₂ to different possible products, such as C1 (formic acid, methane, methanol) or >C1 chemicals (alcohols, dimethyl ether, light olefins, hydrocarbons, etc.). When cheap electrical energy sources are available, converting CO₂ by this approach may be already competitive, as demonstrated from the initiative of Carbon Recycling International (CRI) in Iceland (clean Renewable Methanol process) [22]. Other companies such as Mitsui Chemicals with their “Green House Gases-to-Chemical Resources” technology are active in this field [22]. Also, the conversion of CO₂ to methanol in order to import renewable energy from remote unused resources, is already economically attractive [39] and interesting perspectives exist also on producing light olefins from CO₂ [40].

In a longer-term perspective, it is necessary to reduce the number of steps. A first possibility is to develop inverse fuel cells, where CO₂ is directly fed on a special designed cathodic electrode, able to convert directly CO₂ using protons supplied by water oxidation (on the anodic zone) and electrons supplied externally from a RE source. This is the second type of routes that uses electrochemical or electro-catalytic processes.

In a much longer-time perspective, it is necessary to undertake a fully integrated artificial leaf-type solar cell, where there is the presence of a photo-anode able to photo-electrolyze water using sunlight (photo-electro-catalytic - PEC - solar cell) [41–44]. This is the third class of routes. Photochemical processes are included in this class, because they realize on a nano-scale, the separation between the processes of generation of protons/electrons from water using light, and those of reduction of CO₂ using protons/electrons. PEC solar cells follows the same idea on a macro-scale, but the physical segregation of the two processes in different sections, allows lowering self-quenching effects and separating the products at the anode (O₂) from those formed at the cathode (products of CO₂ EC reduction), with resultant safer operations. Realizing an efficient and effective electrode for the electro-catalytic conversion of CO₂ is a common aspect to both inverse fuel cells and the PEC solar cells.

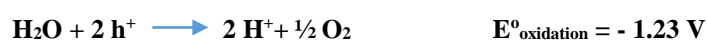
1.2. Solar Fuels – A key to the global challenge

Artificial photosynthetic systems have deeply been studied from a few decades to harvest solar energy and convert CO₂ into important fuels, using systems designed on similar lines based on the well-established photosynthetic process in nature. The process designed in the late 90s by Moore et al. [45, 46] can be considered as the beginning towards the mimicking of the natural bio-systems. This design included the generation of a pH gradient through the membrane of an

artificial vesicle using sunlight, quite similar in lines of natural photosynthesis. The pH gradient achieved is subsequently used as a power source for the ATPase immobilized in the membrane of the vesicle. This artificial system is simple and has the ability to convert solar energy into ATP far better than the natural photosynthetic system. However, there was an underlying problem, which needed to couple this system to another system that could make use of the generated ATP. This problem could not be addressed, and thereby not able to produce useful products from the energy conversion step. Several groups have focused their attention on the second step of photosynthesis, storing a flow of electrons into chemical bonds [47, 48]. However, the complexity and high cost-to-fuel of these designs limit the practicality of using them as a base section in artificial leaf-type systems. Though very close mimicking of the primary coordination sphere of the natural active sites have been achieved, they did not show any noteworthy activity towards CO₂ reduction. This leads to think of taking a slightly different approach towards creating artificial leaves, rather than trying to completely mimic the natural system (only the base idea needs to be considered).

1.2.1. Photo-catalysis (HER reaction)

The first reported overall photocatalytic water splitting by a titanium dioxide (TiO₂) electrode was performed by Fujishima and Honda [49]. After this pioneering work, various research studies on water splitting have been undertaken especially via heterogeneous catalysis using semiconductor materials due their non-overlapping valence bands and conduction bands (with a band gap < insulators and > conductors). When sufficient photochemical energy is provided, excited electrons move into the conduction band, leaving behind electron holes in the valence band and an excess of electrons in the conduction band. These are termed as electron-hole pairs, which play vital roles in the redox reactions of water splitting. Reduction of protons to H₂ is achieved via these electrons, and O²⁻ are oxidized by the holes. In order to start the redox reaction, it is required that the valence band's highest state should be more positive than water oxidation value (E_{O₂/H₂O}, 1.23 V vs. Normal hydrogen electrode; NHE), while the conduction bands lowest state should be more negative than the hydrogen evolution potential (E_{H₂/H₂O}, 0 V vs. NHE) [50].



Thus, the minimum band gap necessary for a viable water-splitting photo-catalyst is 1.23 eV. Accordingly, TiO_2 , ZrO_2 , KTaO_3 , SrTiO_3 , and BiVO_4 fall in this category and are good candidates for photo-catalytic water-splitting [51–53]. However, this condition is not absolute, as the band gaps of some typical semiconductors such as SiC , ZnO and CdS fit well into the water-splitting redox potential but are not active for water-splitting due to photo-corrosion. Photo-corrosion occurs if the anion from the catalyst itself is oxidized by photo-generated holes instead of H_2O . Another main challenge with the catalysts is that most semiconductors bandgap lies under the ultraviolet (UV) band, which accounts for only $\sim 4\%$ of the total solar energy (i.e. 40 W/m^2 out of the entire 1000 W/m^2) [54–56]. To improve the solar energy efficiency, band gap engineering needs to be done to push the photo-catalyst's ability to work under visible light (i.e. the semiconductor band gap $< 3 \text{ eV}$), since visible light contributes to nearly 50 % of the incoming solar energy. Semiconductor catalysts coupled with carbon materials or precious metal nano-particles have shown to have better visible light response [51, 57]. Moreover, metal sulfides, metal nitrides, and some metal-free catalysts proved to be promising candidates for photo-catalytic water splitting by visible light [52, 53, 58 and 59].

The photo-catalytic reactions can be classified into two types: -

Photo-chemical process this type of water-splitting consists of three components: a catalyst, a visible light absorber, and sacrificial electron donor. Although the fundamental principles of photo-chemical and photo-electro-chemical systems are identical, the only difference lies in their setup. As shown in *Fig. 1.4*, the water-splitting reaction occurs at the semiconductor-electrolyte junction where a necessary potential is generated. The semiconductor should be stable (corrosion free) in the electrolyte. Depending on the band gap position of the semiconductor as discussed above, they can be active in production of H_2 or O_2 or overall water-splitting [60].

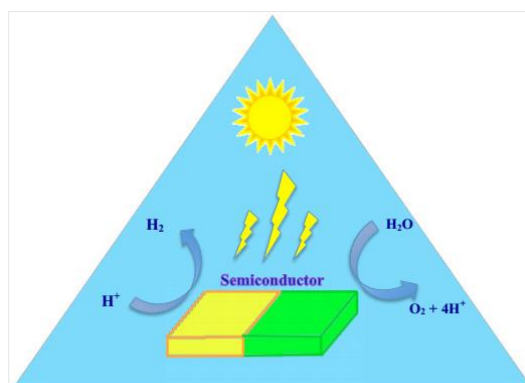


Fig. 1.4 Schematic representation of photo-chemical water splitting [61].

Photo-electro-chemical process: This type, commonly referred as PEC water-splitting, consists of a semiconductor photo-catalyst. When a solar-irradiation greater than its band gap is shined on it, the energy absorbed results in charge separation at the valence and conduction bands. Thereby, generating holes in valence band, which trigger the oxidation of H_2O at the surface of conduction band, and the photo-excited electrons in the conduction band, aid in the reduction of the H^+ to H_2 . In the PEC reactions, semiconductors can be used as photo-cathode or photo-anode and it is necessary the contact with the electrolyte containing a redox couple [62]. A schematic of the PEC water-splitting system is provided in Fig. 1.5.

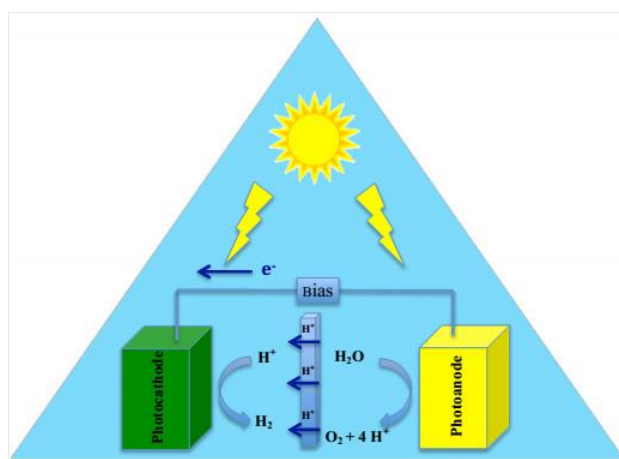


Fig. 1.5 Schematic representation of photo-electro-chemical water splitting [61].

1.2.2. Electro-catalysis (CO_2 reduction)

The photo-electro-catalytic route is a complex system that depends on a high number of factors (photo-catalyst, membrane, electrolyte, electro-catalyst, conductivity, leaks, irradiation conditions, voltage/current bias, diffusion, electrode contact and adherence, etc.). Too many parameters need to be considered in order to clearly understand the effects of varying electro-catalysts. In order to simplify this, a direct current/voltage bias was used instead of light-irradiation to simulate the photo-anodic half-cell. This is termed as electro-catalytic (EC) CO_2 reduction to fuels.

EC reduction of CO_2 involves a multi-step reaction mechanism with complex reaction pathways and can be classified into two types based on the nature of the catalyst: homogeneous and heterogeneous catalysis. In homogeneous CO_2 catalytic reduction systems, the electrode plays the role as an electron transfer media (similar to photosensitizer in photo-catalytic reduction) to the actual molecular catalyst in the electrolytic solution. In the heterogeneous CO_2 catalytic reduction, the reaction occurs at the electrode-electrolyte interface, with the

electrode being a solid electro-catalyst, while the electrolyte is generally an aqueous solution (mixed with salts to create ionic charges) saturated with CO₂ or under a direct flow of CO₂ in electrolyte-less systems. This heterogeneous CO₂ catalytic reduction process contains three major steps: (i) chemical adsorption of CO₂ on the electro-catalyst, (ii) transfer of electrons and protons to break C-O bonds and form C-H bonds, (iii) desorption of the products from the catalytic surface and diffusion into the electrolyte [63, 64]. The end-products depends on the electro-catalyst, electrolyte, potential applied, etc. The reaction products are a mixture of carbon compounds such as carbon monoxide (CO), formate (HCOO⁻) or formic acid (HCOOH), methane (CH₄), ethylene (C₂H₄), ethanol (C₂H₅OH), methanol (CH₃OH), acetic acid (CH₃COOH), etc. [65, 66].

1.2.2.1. General terms reported in EC CO₂ reduction

In regards to end-products reporting, there are many representations used in the literature [67]. These parameters can be defined as follows:

(i) **Onset potential:** This refers to the applied voltage on the electro-catalyst versus the reference electrode, for which the desired product is yielded in detectable quantities. It is to note that the onset potential is usually lower than the CO₂ reduction equilibrium potential, and the difference between them is termed as the over-potential.

(ii) **Faradaic efficiency (FE):** It is defined as the percentage of electrons utilized for the formation of a specific product. The FE is a direct indicator of product selectivity and can be calculated by the following equation:

$$FE = [(\alpha n F) / Q]$$

where α is the number of electrons transferred (e.g., $\alpha = 2$ for CO₂ reduction to HCOOH); n is the number of moles of the product yielded; F is the Faraday's constant (96485 C mol⁻¹); Q is the average charge passed.

(iii) **Energetic efficiency (EE):** The EE is defined as the net energy utilized towards the desired product. Higher energy efficiency is achieved for a high FE and a lower over-potential. It can be calculated by the following equation:

$$EE = [(E_{eq} * FE) / (E_{eq} + \eta)]$$

where E_{eq} is equilibrium potential; η is the over-potential.

(iv) **Current density:** The overall current density for CO₂ reduction is defined as the average current observed divided by the geometric surface area of the working electrode. It provides a measure to the reaction rate and it is crucial in understanding the electrolyser size needed and the cost of the system. The partial current densities for individual products can be calculated by multiplying corresponding FE with net current density.

(v) **Tafel plot:** This plot is derived from the over-potential versus logarithm of current density. This is very useful to evaluate the performance of the electro-catalyst. In general, the smaller is the Tafel slope, the better is the catalytic performance. For CO₂ electro-reduction, the Tafel slope gives an insight into the reaction mechanism. For example, a Tafel slope of 118 mV dec⁻¹ indicates that the rate determining step for CO₂ reduction is the CO₂⁻ generation, a key intermediate via one-electron transfer, while slope of 59 mV dec⁻¹ indicates the one-electron pre-equilibrium step before the rate-limiting chemical step [68].

(vi) **Turnover number (TON):** The *TON* is defined as the number of catalytic cycles that occur per catalyst over the catalytic lifetime. It can be calculated as the molar ratio of CO₂ reduction products to the amount of catalytic sites initially present:

$$TON = [(CO_2 \text{ reduction product}) / (catalyst)]$$

(vii) **Turnover frequency (TOF):** The *TOF* is defined the number of catalytic cycles per catalyst molecule per unit time. It can be calculated as:

$$TOF = [(CO_2 \text{ reduction product}) / (catalyst * time)] = [TON / time]$$

1.2.3. Thermodynamics

CO₂ is the most stable oxidized form of carbon and also, the end product of all combustion reactions of carbon-based fuels. CO₂ shows exceptional thermodynamic stability. Therefore, understanding the thermodynamics of the CO₂ reduction, is one of the major necessary aspects to decipher this challenging reaction pathway. *Fig. 1.6* and *Fig. 1.7* show that for different electrodes, the reduction of CO₂ to the radical CO₂⁻ (using one electron) is the first step for various product formations [69, 70], but it is also a very energy intensive and unfavourable process [71]. Other pathways are much less energy consuming, as shown in *Table 1.1*. All these reactions, involve protons coupled with electrons to sustain and provide the energy required

for the reaction, in a similar fashion to that of natural photosynthetic systems, and consume less energy, as hinted by less negative potentials [72, 73].

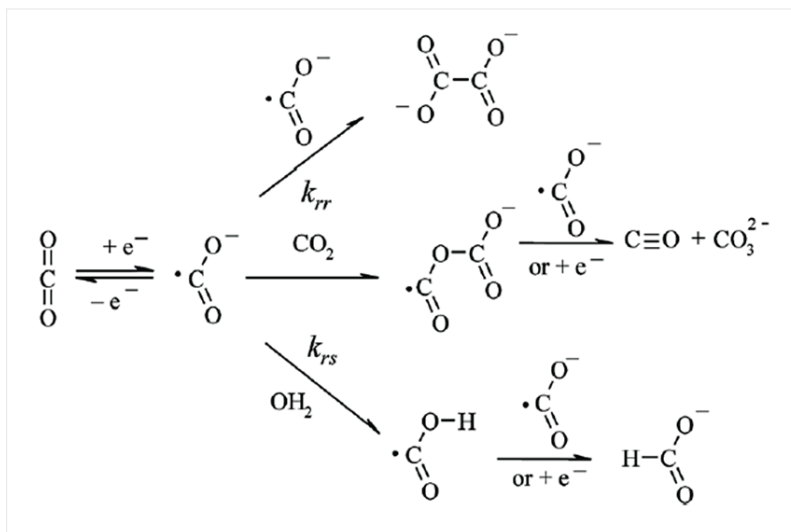


Fig. 1.6 Reaction pathways of CO₂ reduction to oxalate, CO, formate on inert electrodes [69].

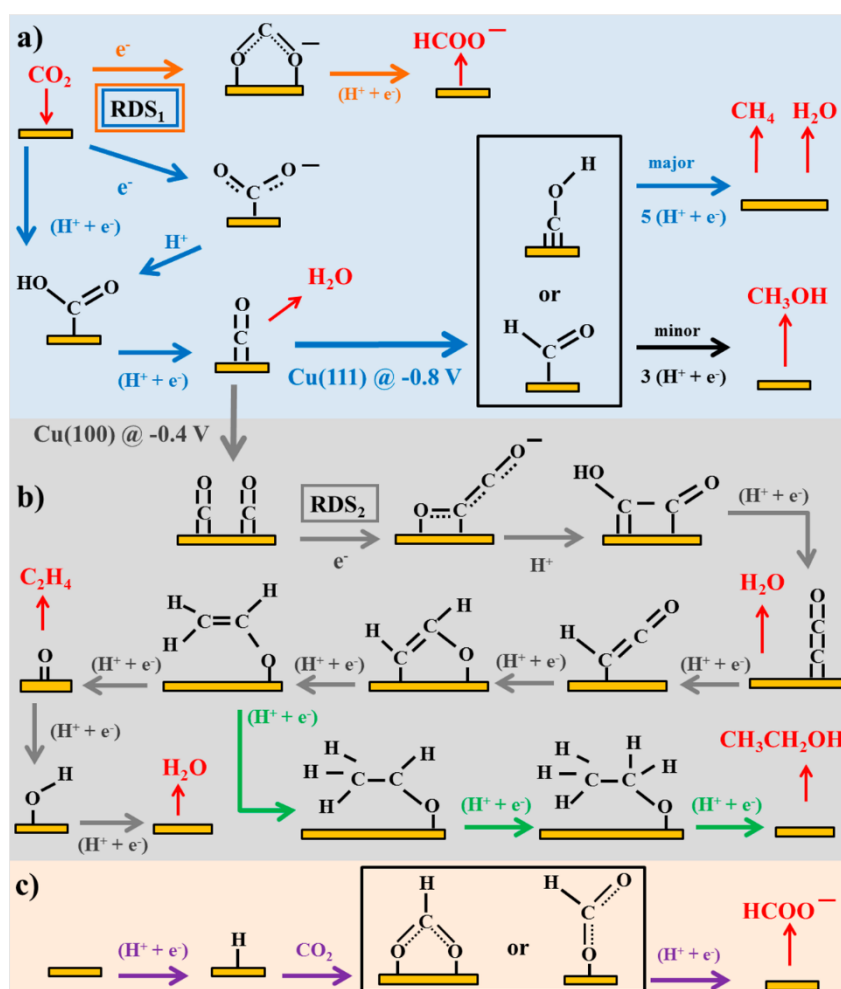


Fig. 1.7 Reaction pathways of CO₂ reduction to different products on transition metal and molecular catalytic electrodes [70].

Table 1.1 CO₂ reduction potentials for various CO₂ reduction reactions products [74, 75].

Reactions	E° (V) vs. SHE (at pH 7)
$2 \text{H}^+ + 2 e^- \rightarrow \text{H}_2$	- 0.41
$\text{CO}_2 + e^- \rightarrow \text{CO}_2^{\cdot -}$	- 1.89
$\text{CO}_2 + 2 e^- + 2 \text{H}^+ \rightarrow \text{HCOOH}$	- 0.60
$\text{CO}_2 + 2 e^- + 2 \text{H}^+ \rightarrow \text{CO} + \text{H}_2\text{O}$	- 0.52
$\text{CO}_2 + 4 e^- + 4 \text{H}^+ \rightarrow \text{C} + \text{H}_2\text{O}$	- 0.19
$\text{CO}_2 + 4 e^- + 4 \text{H}^+ \rightarrow \text{HCHO} + \text{H}_2\text{O}$	- 0.45
$\text{CO}_2 + 6 e^- + 6 \text{H}^+ \rightarrow \text{CH}_3\text{OH} + \text{H}_2\text{O}$	- 0.35
$\text{CO}_2 + 8 e^- + 8 \text{H}^+ \rightarrow \text{CH}_4 + \text{H}_2\text{O}$	- 0.23
$\text{CO}_2 + 12 e^- + 12 \text{H}^+ \rightarrow \text{C}_2\text{H}_4 + \text{H}_2\text{O}$	- 0.34

The trend of the reduction potentials from the *Table 1.1*, shows that the higher is the number of protons and electrons involved, the lower is the negative potential, and thus, lower energy consumption. However, these reactions still need energy and a suitable catalyst. Catalysts help to overcome the kinetic threshold limits and the energy to drive the electrons necessary at the reaction potential. Energy transfer to the system can be achieved via different routes: (i) a sacrificial material (oxidation potential is negative enough to react with CO₂) can be added for direct reduction of CO₂; (ii) photo-anode can be used to pump the energy necessary for the reaction (similar to natural system); (iii) an electrode used to provide for catalytic surface or for transfer of electrons (thenecessary potential of the catalytic species).

1.2.4. Catalysts

Various types of catalysts have been studied for quite a few decades [75-85]. These include bulk metals, nanostructured metals, mixed metals, non-metallic, molecular catalysts [86-104]. A detailed overview of these types of catalysts is shown in *Fig. 1.8*. The bulk metallic catalysts showed good activity for CO₂ reduction but they should be considered as a good starting point in understanding the fundamental effects of various metals. To improve the activity and performance of these metallic catalysts, further research has been undertaken into advanced nano-structured catalysts, such as nano-particles with varying shapes (spherical, cylindrical, rectangular, triangular, hexagonal, elliptical, etc), nano-porous, nanowires, etc.

Highly nano-structured catalysts not only gave rise to much higher currents, but also they exhibited unique catalytic properties as compared to their bulk counterparts. This category of catalysts showed promising results and enhancements over the bulk metallic catalysts. A third kind of catalysts was also studied, which had one common foundation principle: move away from usage of expensive metals; leading to studies on semiconducting materials, 2D materials (MoS₂, MoSe₂, grapheme, etc), carbon fibres and nanotubes, doped carbon materials, etc. Another category of catalysts laid there foundation on having a bio-mimetic materials that are close to bio-molecules in nature.

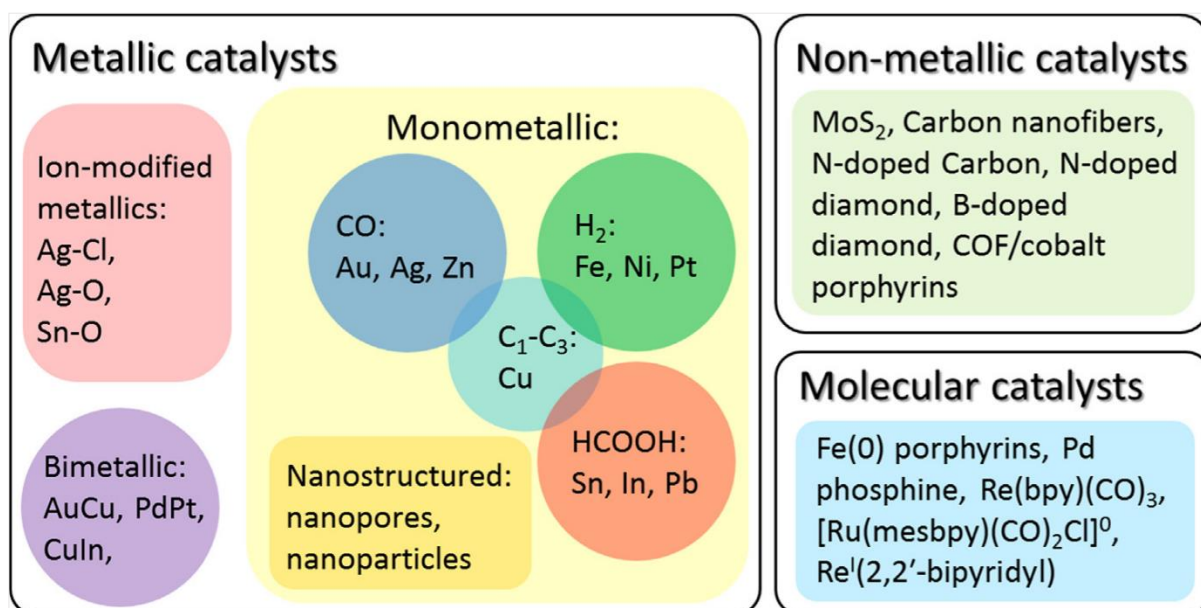


Fig. 1.8 A graphical view on various categories of electrocatalysts of CO₂ reduction [75].

1.3. Global research outlook on CO₂ reduction

In this section, a detailed overview into the fuel productivity data and the respective electro-catalytic conditions applied for the CO₂ reduction studies reported in the literature is addressed. These reported data are given for different categories of catalysts as discussed in the previous section. *Table 1.2* gives an insight into the details of the catalyst (all 4 categories – bulk metals, nano-structured metals, non-metallic and molecular) used, electro-catalytic conditions applied and the fuel productivity data [105, 106]. The basic bulk metallic catalysts favoured formation of certain products – HCOOH (Pb, Hg, In, Sn, Cd, Tl); CO (Au, Ag, Zn, Pd, Ga); CH₄, C₂H₄ and other hydrocarbons (Cu); H₂ (Pt, Ni, Fe, Ti) [107]. The formation of different products gives a raw idea into the selectivity for different metals.

Table 1.2 The performance report for various electro-catalysts in CO₂ reduction [105].

Electrodes	E vs. RHE (V)	Major Products	Faradaic Efficiency (%)	Reference	Current Density (mA cm ⁻²)	Electrolyte
Cu (10 nm)	- 1.1	H ₂ , CO, CH ₄ , C ₂ H ₄	64, 22, 10, 4	[108]	20	0.1 M KHCO ₃
Cu	- 1.25	H ₂ , CH ₄	13, 80	[109]	9	0.1 M NaHCO ₃
Ag	- 0.60	CO	92	[110]	18	0.5 M KHCO ₃
Ag	- 1.35	H ₂ , CO	55, 40	[111]	10	0.1 M KHCO ₃
Au (8 nm)	- 0.67	CO	90	[112]	-	0.5 M KHCO ₃
Au	- 0.35	CO	94	[113]	-	0.5 M KHCO ₃
Au (3.2 nm)	- 1.2	H ₂ , CO	80, 20	[114]	100	0.1 M KHCO ₃
Au	- 0.45	CO	90	[115]	-	0.5 M NaHCO ₃
Pd (3.7 nm)	- 0.89	CO	91.2	[116]	9	0.1 M KHCO ₃
Pd	- 0.15	HCOO ⁻	95	[117]	7	2.8 M KHCO ₃
Oxide-derived Au	- 0.4	CO	98	[118]	10	0.5 M NaHCO ₃
Oxide-derived Cu	- 0.5	CO, HCOOH	40, 33	[119]	2.7	0.5 M NaHCO ₃
Sn/SnO_x	- 0.7	CO, HCOOH	58, 40	[120]	1.8	0.5 M NaHCO ₃
Sn/grapheme	- 1.16	HCOO ⁻	93.6	[121]	10.2	0.1 M NaHCO ₃
Au₃Cu	- 0.73	CO, HCOO ⁻	64.7, 3.11	[122]	3	0.1 M KHCO ₃
Cu-In	- 0.6	CO, HCOOH	38, 34	[123]	1	0.1 M KHCO ₃
Ag/TiO₂	- 0.8	CO	> 90	[124]	101	1 M KOH
MoS₂	- 0.764	CO	98	[125]	65	H ₂ O/EMIM-BF ₄
PEI-NCNT	- 1.16	HCOO ⁻	85	[126]	7.2	0.1 M KHCO ₃
CNF	- 0.25	CO	-	[127]	4	EMIM-BF ₄
BDD	- 0.9	HCHO, HCOOH	65, 14	[128]	0.08	0.1 M MeOH (TBAP)
NCNT	- 0.28	CO	80	[129]	0.9	0.1 M KHCO ₃
[(bpy)₂Ru(dmbbbpy)Ru(bpy)₂](PF₆)₄	- 1.55	C ₂ O ₄ ²⁻	70	[130]	-	MeCN + 2.5 % H ₂ O

1.4. Thesis (main aim, scope and chapter goals)

The central idea of the research work is – 1) to develop compact electro-catalytic CO₂ reduction cells in liquid and gas phase (electrolyte-less conditions); 2) to design gas diffusible catalytic electrodes for CO₂ reduction that can be compared with data available in literature; 3) to test the electrodes and determine the fuel productivity, selectivity and to study the underlying reaction mechanism.

Chapter 2 deals with: 1) the design of the gas phase cell, the specific electrode design and metal nanoparticle doped carbon catalysts (importance of using carbon based systems); 2) testing of these electrodes in gas phase conditions to evaluate the fuel productivity and selectivity; 2) a separate set of electrodes, which were prepared via modifying the above gas diffusible electrodes with metal-organic frameworks (MOFs) and studied to determine the effects on CO₂ reduction.

Chapter 3 deals with the development of the liquid phase cell (to have a proper comparison with literature data), the specific electrode design and the synthetic routes to prepare metal nanoparticle doped carbon catalysts, then tested in liquid phase conditions to evaluate the fuel productivity and selectivity.

Chapter 4 deals with a similar set of catalytic electrodes (metal nanoparticle doped carbon catalysts), but prepared by different synthetic routes (organo-metallic and nanowire routes), to achieve size controlled, uniform nanoparticle doping. These synthetic routes are discussed in detail both novel routes and existing routes. Organo-metallic routes for Pt, Ru are well established while for Fe we designed a novel route. A size dependent study was conducted for the liquid phase CO₂ reduction to fuels in order to improve fuel productivity, fuel selectivity and optimize nanoparticle doping parameters.

Chapter 5 deals with the synthesis of metallic (Cu, Fe) nanofoams or dendrite like structures on various metal substrates (such as Cu, Fe, Al, Inconel, Al grid, steel wool) using electro-chemical deposition technique. The main motive behind this endeavour is to attain higher surface area catalytic materials of low cost, abundant transition metals. These nano-foam electrodes were experimented in the liquid phase for their fuel productivity.

Chapter 6 deals with the general conclusions from all the research works presented in the previous chapters. This summarizes, the overall results achieved in the CO₂ electrocatalytic reduction tests, the performance improvements, gas & liquid phase cell designs and engineering principles, novel synthesis route developed for catalyst preparation and new catalysts developed.

1.5. References

- [1]“Key World Energy Statistics 2015”, *IEA*.
- [2]“World Population Data Sheet 2016”, *Population Reference Bureau*.
- [3]“World Population Prospects - Population Division - United Nations”, *esa.un.org*.
- [4]“World energy outlook 2016”, *IEA*.
- [5]“IRENA - Renewable energy and jobs 2015”, *IRENA, Annual review*.
- [6]“Global Energy Trends - 2016 report”, *IEA*.
- [7]Hansen, J., R. Ruedy, M. Sato, and K. Lo (2010). Global surface temperature change. *Reviews of Geophysics*, 48 (RG4004).
- [8]“Greenhouse Gas Inventory Data Explorer – 2014”, *Environmental protection agency*.
- [9]Canadell, J.G., et al., *Proceedings of the National Academy of Sciences*, 2007, **104**(47), 18866-18870.
- [10]Le Quere, C., et al., Trends in the sources and sinks of carbon dioxide, *Nature Geosci.*, 2009, **2**(12), 831-836.
- [11]Tans, D.P. *NOAA/ESRL* (www.esrl.noaa.gov/gmd/ccgg/trends/) and Dr. Ralph Keeling, Scripps Institution of Oceanography (scrippsco2.ucsd.edu/).
- [12]Houghton, J.T., Climate Change, 1995, *the Science of Climate Change*, ed. C.U. Press 1996, Cambridge.
- [13]Wigley, T.M.L., *Geophysical Research Letters*, 1995, **22**(1), 45.
- [14]CO₂ and temperature rise prediction, *Intergovernmental Panel on Climate Change*.
- [15]“World Energy Assesment Report: Energy and the Challenge of Sustainability, 2003”, *United Nations Development Program*.
- [16]G. Centi, S. Perathoner, *Catal. Today*, 2009, **148**, 191.a
- [17]A. Dhakshinamoorthy, S. Navalon, A. Corma, H. Garcia, *Energy Environ. Sci.*, 2012, **5**, 9217.
- [18]G.P. Smestad, S. Steinfeld, *Ind. Eng. Chem. Res.*, 2012, 51, 11828.
- [19]Y. Izumi, *Coord. Chem. Rev.*, 2013, **257**, 171.

- [20] C. Graves, S.D. Ebbesen, M. Mogensen, K.S. Lackner, *Renew. Sustain. Energy Rev.*, 2011, **15**, 1.
- [21] J. Cejka, G. Centi, J. Perez-Pariente, W.J. Roth, *Catal. Today*, 2012, **179**, 2.
- [22] E.A. Quadrelli, G. Centi, J.-L. Duplan, S. Perathoner, *ChemSusChem*, 2011, **4**, 1194.
- [23] H.-R.M. Jhong, S. Ma, P.J.A. Kenis, *Curr. Opin. Chem. Eng.*, 2013, **2**, 191.
- [24] T.W. Woolerton, S. Sheard, E. Pierce, S.W. Ragsdale, F.A. Armstrong, *Energy Environ. Sci.*, 2011, **4**, 2393.
- [25] D.T. Whipple, P.J.A. Kenis, *J. Phys. Chem. Lett.*, 2010, **1**, 3451.
- [26] G. Wus, K. Xie, Y. Wu, W. Yao, J. Zhou, *J. Power Source*, 2013, **232**, 187.
- [27] E. Ruiz, D. Cillero, P.J. Martinez, A. Morales, G. san Vicente, G. de Diego, J.M. Sanchez, *Catal. Today*, 2013, **210**, 55.
- [28] A.F. Perez-Cadenas, C.H. Ros, S. Morales-Torres, M. Perez-Cadenas, P.J. Kooyman, C. Moreno-Castilla, F. Kapteijn, *Carbon*, 2013, **56**, 324.
- [29] Y. Oh, X. Hu, *Chem. Soc. Rev.*, 2013, **42**, 2253.
- [30] H.A. Hansen, J.B. Varley, A.A. Peterson, J.K. Norskov, *J. Phys. Chem. Lett.*, 2013, **4**, 388.
- [31] C. Costentin, M. Robert, J.-M. Saveant, *Chem. Soc. Rev.*, 2013, **42**, 2423.
- [32] D. Cheng, F.R. Negreiros, E. Apra, A. Fortunelli, *ChemSusChem*, 2013, **6**, 944.
- [33] Y. Na, P. Lincoln, J.R. Johansson, B. Norden, *ChemCatChem*. 2012, **4**, 1746.
- [34] C. Liu, T.R. Cundari, A.K. Wilson, *J. Phys. Chem. C*, 2012, **116**, 5681.
- [35] K.P. Kuhl, E.R. Cave, D.N. Abram, T.F. Jaramillo, *Energy Environ. Sci.* 2012, **5**, 7050.
- [36] J.A. Keith, E.A. Carter, *J. Am. Chem. Soc.*, 2012, **134**, 7580.
- [37] J.L. Inglis, B.J. MacLean, M.T. Pryce, J.G. Vos, *Coord. Chem. Rev.*, 2012, **256**, 2571.
- [38] L.L. Snuffin, L.W. Whaley, L. Yu, *J. Electrochem. Soc.*, 2011, **158**, F155.
- [39] L. Barbato, G. Iaquaniello, A. Mangiapane, in: M. De Falco, G. Iacquaneillo, G. Centi (Eds.), *CO₂: A Valuable Source of Carbon*, Springer (Green Energy and Technology series), Germany, 2013, pp. 67–79.
- [40] G. Centi, G. Iaquaniello, S. Perathoner, *ChemSusChem*, 2011, **4**, 1265.
- [41] S. Bensaid, G. Centi, E. Garrone, S. Perathoner, G. Saracco, *ChemSusChem*, 2012, **5**, 500.
- [42] C. Ampelli, G. Centi, R. Passalacqua, S. Perathoner, *Energy Environ. Sci.*, 2010, **3**, 292.
- [43] C. Ampelli, C. Genovese, R. Passalacqua, S. Perathoner, G. Centi, *Theor. Found. Chem. Eng.*, 2012, **46**, 651.
- [44] C. Ampelli, R. Passalacqua, C. Genovese, S. Perathoner, G. Centi, *Chem. Eng. Trans.*, 2011, **25**, 683.

- [45] G. S. Yfrach, P. A. Liddell, S. C. Hung, A. L. Moore, D. Gust, T. A. Moore, *Nature*, 1997, **385**, 239.
- [46] G. S. Yfrach, J. L. Rigaud, E. N. Durantini, A. L. Moore, D. Gust, T. A. Moore, *Nature*, 1998, **392**, 479.
- [47] A. Parkin, J. Seravalli, K. A. Vincent, S. W. Ragsdale, F. A. Armstrong, *J. Am. Chem. Soc.*, 2007, **129**, 10328.
- [48] T. Reda, C. M. Plugge, N. J. Abram, J. Hirst, *Proceedings of the National Academy of Sciences*, 2008, **105**, 10654.
- [49] A. Fujishima, K. Honda, *Nature*, 1972, **238**, 37.
- [50] T. Jafari, E. Moharreri, A. S. Amin, R. Miao, W. Song, S. L. Suib, *Molecules*, 2016, **21**, 900.
- [51] M. Halmann, M. Grätzel, *Energy Resources through Photochemistry and Catalysis*; Academic Press: New York, NY, USA, 1983.
- [52] N. Serpone, E. Pelizzetti, *Photocatalysis: Fundamentals and Applications*; Wiley: New York, NY, USA, 1989.
- [53] Y. V. Pleskov, Y. Y. Gurevich, *Semiconductor Photoelectrochemistry*; Consultants Bureau: New York, NY, USA, 1986.
- [54] A. Kudo, Y. Miseki, *Chem. Soc. Rev.*, 2009, **38**, 253.
- [55] A. L. Linsebigler, J. T. Yates Jr., G. Lu, *Chem. Rev.*, 1995, **95**, 735.
- [56] Z. Zou, J. Ye, K. Sayama, H. Arakawa, *Nature*, 2001, **414**, 625.
- [57] K. Sivula, R. van de Krol, *Nat. Rev. Mater.*, 2016, **70**, 15010:1.
- [58] H. Yoneyama, H. Sakamoto, H. Tamura, *Electrochim. Acta*, 1975, **20**, 341.
- [59] M. Ni, M. K. H. Leung, D. Y. C. Leung, K. Sumathy, *Renew. Sustain. Energy Rev.*, 2007, **11**, 401.
- [60] N. S. Lewis, *Nature*, 2001, **414**, 589.
- [61] A. Currao, *Chimia (Aarau)*, 2007, **61**, 815.
- [62] S. Ikeda, T. Itani, K. Nango, M. Matsumura, *Catal. Lett.*, 2004, **98**, 229.
- [63] R. J. Lim, M. Xie, M. A. Sk, J. M. Lee, A. Fisher, X. Wang, K. H. Lim, *Catal. Today*, 2014, **233**, 169.
- [64] R. Schlogl, *Angew. Chem. Int. Ed.*, 2015, **54**, 3465.
- [65] J. Qiao, Y. Liu, F. Hong, J. Zhang, *Chem. Soc. Rev.*, 2014, **43**, 631.
- [66] J. Albo, M. A. Guerra, P. Castaño, A. Irabien, *Green Chem.*, 2015, **17**, 2304.
- [67] H. R. M. Jhong, S. Ma, P. J. A. Kenis, *Curr. Opin. Chem. Eng.*, 2013, **2**, 191.
- [68] E. Gileadi, *Electrode Kinetics for Chemists, Engineers, and Materials Scientists*, Wiley-VCH, Weinheim, Germany 1993.

- [69] C. Costentin, M. Robert and J.-M. Savéant, *Chem. Soc. Rev.*, 2013, **42**, 2423.
- [70] R. Kortlever, J. Shen, K. J. P. Schouten, F. C. Vallejo, M. T. M. Koper, *J. Phys. Chem. Lett.*, 2015, **6**, 4073.
- [71] H.A. Schwarz and R.W. Dodson, *J. of Phys. Chem.*, 1989, **93**, 409.
- [72] I. Willner, R. Maidan, D. Mandler, H. Duerr, G. Doerr, K. Zengerle, *J. Am. Chem. Soc.*, 1987, **109**, 6080.
- [73] E. B. Cole, P. S. Lakkaraju, D. M. Rampulla, A. J. Morris, E. Abelev, A. B. Bocarsly, *J. Am. Chem. Soc.*, 2010, **132**, 11539.
- [74] A. J. Morris, G.J. Meyer and E. Fujita, *Acc. Chem. Res.*, 2009, **42**, 1983.
- [75] Q. Lu and F. Jiao, *Nano Energy*, 2016, (in press).
- [76] Y. Hori, Electrochemical CO₂ reduction on metal electrodes, in: C.G. Vayenas, R. E. White, M.E. GamboaAldeco (Eds.), *Modern Aspects of Electrochemistry*, 2008, **42**, 89.
- [77] K.P. Kuhl, T. Hatsukade, E.R. Cave, D.N. Abram, J. Kibsgaard, T.F. Jaramillo, *J. Am. Chem. Soc.*, 2014, **136**, 14107.
- [78] R.L. Cook, R.C. Macduff, A.F. Sammells, *J. Electrochem. Soc.*, 1987, **134**, 1873.
- [79] D.W. Dewulf, A.J. Bard, *Catal. Lett.*, 1988, **1**, 73.
- [80] Y. Hori, K. Kikuchi, A. Murata, S. Suzuki, *Chem. Lett.*, 1986, 897.
- [81] Y. Hori, K. Kikuchi, S. Suzuki, *Chem. Lett.*, 1985, 1695.
- [82] Y. Hori, A. Murata, R. Takahashi, *J. Chem. Soc.-Faraday Trans. 1*, 1989, **85**, 2309.
- [83] Y. Hori, H. Wakebe, T. Tsukamoto, O. Koga, *Electrochim. Acta*, 1994, **39**, 1833.
- [84] S. Ikeda, T. Takagi, K. Ito, *Bull. Chem. Soc. Jpn.*, 1987, **60**, 2517.
- [85] M. Maeda, Y. Kitaguchi, S. Ikeda, K. Ito, *J. Electroanal. Chem.*, 1987, **238**, 247.
- [86] A.M. Appel, J.E. Bercaw, A.B. Bocarsly, H. Dobbek, D.L. DuBois, M. Dupuis, J.G. Ferry, E. Fujita, R. Hille, P.J.A. Kenis, C.A. Kerfeld, R.H. Morris, C.H.F. Peden, A.R. Portis, S.W. Ragsdale, T.B. Rauchfuss, J.N.H. Reek, L.C. Seefeldt, R.K. Thauer, G.L. Waldrop, *Chem. Rev.*, 2013, **113**, 6621.
- [87] C. Costentin, M. Robert, J.M. Saveant, *Chem. Soc. Rev.*, **42**, 2423.
- [88] Q. Lu, J. Rosen, F. Jiao, *ChemCatChem*, 2015, **7**, 38.
- [89] Q. Lu, J. Rosen, Y. Zhou, G.S. Hutchings, Y.C. Kimmel, J.G.G. Chen, F. Jiao, *Nat. Commun.*, 2014, **5**.
- [90] J. Rosen, G.S. Hutchings, Q. Lu, R.V. Forest, A. Moore, F. Jiao, *ACS Catal.*, 2015, **5**, 4586.
- [91] J. Rosen, G.S. Hutchings, Q. Lu, S. Rivera, Y. Zhou, D.G. Vlachos, F. Jiao, *ACS Catal.*, 2015, **5**, 4293.
- [92] Y.H. Chen, M.W. Kanan, *J. Am. Chem. Soc.*, 2012, **134**, 1986.

- [93] C.W. Li, M.W. Kanan, *J. Am. Chem. Soc.*, 2012, **134**, 7231.
- [94] S.C. Ma, Y.C. Lan, G.M.J. Perez, S. Moniri, P.J.A. Kenis, *ChemSusChem*, 2014, **7**, 866.
- [95] Y.C. Hsieh, S.D. Senanayake, Y. Zhang, W.Q. Xu, D.E. Polyansky, *ACS Catal.*, 2015, **5**, 5349.
- [96] D. Kim, J. Resasco, Y. Yu, A.M. Asiri, P.D. Yang, *Nat. Commun.*, 2014, **5**.
- [97] R. Kortlever, I. Peters, S. Koper, M.T.M. Koper, *ACS Catal.*, 2015, **5**, 3916.
- [98] S. Rasul, D.H. Anjum, A. Jedidi, Y. Minenkov, L. Cavallo, K. Takane, *Angew. Chem. Int. Ed.*, 2015, **54**, 2146.
- [99] Y. M. Liu, S. Chen, X. Quan, H.T. Yu, *J. Am. Chem. Soc.*, 2015, **137**, 11631.
- [100] A.S. Varela, N.R. Sahraie, J. Steinberg, W. Ju, H.S. Oh, P. Strasser, *Angew. Chem. Int. Ed.*, 2015, **54**, 10758.
- [101] M. Asadi, B. Kumar, A. Behranginia, B.A. Rosen, A. Baskin, N. Reppin, D. Pisasale, P. Phillips, W. Zhu, R. Haasch, R.F. Klie, P. Kral, J. Abiade, A. Salehi-Khojin, *Nat. Commun.*, 2014, **5**.
- [102] B. Kumar, M. Asadi, D. Pisasale, S. Sinha-Ray, B.A. Rosen, R. Haasch, J. Abiade, A. L. Yarin, A. Salehi-Khojin, *Nat. Commun.*, 2013, **4**.
- [103] K. Nakata, T. Ozaki, C. Terashima, A. Fujishima, Y. Einaga, *Angew. Chem. Int. Ed.*, 2014, **53**, 871.
- [104] S. Lin, C.S. Diercks, Y.B. Zhang, N. Kornienko, E.M. Nichols, Y.B. Zhao, A.R. Paris, D. Kim, P. Yang, O.M. Yaghi, C.J. Chang, *Science*, 2015, **349**, 1208.
- [105] D.D. Zhu, J. L. Liu, S. Z. Qiao, *Adv. Mat.*, 2016, **28**, 3423.
- [106] J. Qiao, Y. Liu, F. Hong and J. Zhang, *Chem. Soc. Rev.*, 2014, **43**, 631.
- [107] H. R. M. Jhong, S. Ma and P. J. Kenis, *Current opinion in Chem. Engg.*, 2013, **2**, 191.
- [108] R. Reske, H. Mistry, F. Behafarid, B. R. Cuenya, P. Strasser, *J. Am. Chem. Soc.*, 2014, **136**, 6978.
- [109] K. Manthiram, B. J. Beberwyck, A. P. Alivisatos, *J. Am. Chem. Soc.*, 2014, **136**, 13319.
- [110] Q. Lu, J. Rosen, Y. Zhou, G. S. Hutchings, Y. C. Kimmel, J. G. Chen, F. Jiao, *Nat. Commun.*, 2014, **5**, 3242.
- [111] T. Hatsukade, K. P. Kuhl, E. R. Cave, D. N. Abram, T. F. Jaramillo, *Phys. Chem. Chem. Phys.*, 2014, **16**, 13814.
- [112] W. Zhu, R. Michalsky, O. Metin, H. Lv, S. Guo, C. J. Wright, X. Sun, A. A. Peterson, S. Sun, *J. Am. Chem. Soc.*, 2013, **1**, 16833.
- [113] W. Zhu, Y. J. Zhang, H. Zhang, H. Lv, Q. Li, R. Michalsky, A. A. Peterson, S. Sun, *J. Am. Chem. Soc.*, 2014, **136**, 16132.

- [114] H. Mistry, R. Reske, Z. Zeng, Z. J. Zhao, J. Greeley, P. Strasser, B. R. Cuenya, *J. Am. Chem. Soc.*, 2014, **136**, 16473.
- [115] X. Feng, K. Jiang, S. Fan, M. W. Kanan, *J. Am. Chem. Soc.*, 2015, **137**, 4606.
- [116] D. Gao, H. Zhou, J. Wang, S. Miao, F. Yang, G. Wang, J. Wang, X. Bao, *J. Am. Chem. Soc.*, 2015, **137**, 4288.
- [117] X. Min, M. W. Kanan, *J. Am. Chem. Soc.*, 2015, **137**, 4701.
- [118] Y. Chen, C. W. Li, M. W. Kanan, *J. Am. Chem. Soc.*, 2012, **134**, 19969.
- [119] C. W. Li, M. W. Kanan, *J. Am. Chem. Soc.*, 2012, **134**, 7231.
- [120] Y. Chen, M. W. Kanan, *J. Am. Chem. Soc.*, 2012, **134**, 1986.
- [121] S. Zhang, P. Kang, T. J. Meyer, *J. Am. Chem. Soc.*, 2014, **136**, 1734.
- [122] D. Kim, J. Resasco, Y. Yu, A. M. Asiri, P. Yang, *Nat. Commun.*, 2014, **5**, 4948.
- [123] S. Rasul, D. H. Anjum, A. Jedidi, Y. Minenkov, L. Cavallo, K. Takanebe, *Angew. Chem. Int. Ed.*, 2015, **54**, 2146.
- [124] S. Ma, Y. Lan, G. M. Perez, S. Moniri, P. J. Kenis, *ChemSusChem*, 2014, **7**, 866.
- [125] M. Asadi, B. Kumar, A. Behranginia, B. A. Rosen, A. Baskin, N. Reprin, D. Pisasale, P. Phillips, W. Zhu, R. Haasch, R. F. Klie, P. Král, J. Abiade, A. Salehi-Khojin, *Nat. Commun.*, 2014, **5**, 4470.
- [126] S. Zhang, P. Kang, S. Ubnoske, M. K. Brennaman, N. Song, R. L. House, J. T. Glass, T. J. Meyer, *J. Am. Chem. Soc.*, 2014, **136**, 7845.
- [127] B. Kumar, M. Asadi, D. Pisasale, S. Sinha-Ray, B. A. Rosen, R. Haasch, J. Abiade, A. L. Yarin, A. Salehi-Khojin, *Nat. Commun.*, 2013, **4**, 2819.
- [128] K. Nakata, T. Ozaki, C. Terashima, A. Fujishima, Y. Einaga, *Angew. Chem. Int. Ed.*, 2014, **126**, 890.
- [129] J. Wu, R. M. Yadav, M. Liu, P. P. Sharma, C. S. Tiwary, L. Ma, X. Zou, X.-D. Zhou, B. I. Yakobson, J. Lou, P. M. Ajayan, *ACS Nano*, 2015, **9**, 5364.
- [130] Md. M. Ali, H. Sato, T. Mizukawa, K. Tsuge, M. Haga, K. Tanaka, *Chem. Commun.*, 1998, **2**, 249.

CHAPTER 2

CO₂ electro-catalytic reduction in electrolyte-less conditions (Gas phase)

2.1. Introduction

2.1.1. State of the art

In this section, a detailed insight into the electrolyte-less CO₂ electrocatalytic reduction process is reported. Many reviews in literature discussed about the electrocatalytic reduction of CO₂ (see Chapter 1) but most of the photo- and electro-chemical studies were performed in liquid phase ^[1-6], i.e. in presence of a bulk electrolyte used to close the electric circuit in a PEC device. The electrolyte-less (EL) cell, also referred as gas phase cell, laid instead the basis for the futuristic aim of creating a viable artificial leaf or a complete photo-electro-catalytic cell ^[7-14]. The use of gas phase cell provides in fact many advantages: i) a simplification in the cell design suitable for easy industrial scale-up ii) no CO₂ adsorption issues iii) the possibility to operate at higher temperatures iv) no corrosion of the electrode and v) no difficulty in the recovery of liquid fuels produced. The recovery of the products of reaction is often an energetically-costly operation, which may eventually require more energy than the amount of renewable energy obtained in the same reaction. By using a cell designed for gas phase and continuous operations, the liquid fuels obtained can be collected without the need of distillation procedure. Moreover, long chain products were formed in gas phase compared to liquid phase conditions, in relation to differences in the reaction mechanism. This EL approach was widely reported by Centi and Perathoner's research group ^[15-23]. As the present PhD work was carried out within the same group, it is useful now to discuss some previous results in order to make a comparison with liquid phase experiments, which are the real objective of this work. However, some gas phase experiments were carried out by using MOF materials, as it will be described below.

2.1.1.1. Preparation of the electro-catalytic material

The electrodes used in the EL conversion of CO₂ to liquid fuels (>C₁) were based on carbon materials (carbon nanotubes – CNT – or carbon black – CB) doped with different metal nanoparticles (Fe, Co, Cu, Pt), then deposited onto a Gas Diffusion Layer (GDL SIGRACET GDL 24BC, supplied by SGL Group).

Commercial CNTs (cup-stacked CNT from Pyrograph Inc, PR-24-XT) were used as the base materials. These CNTs show a two layered wall structure: the inner layer consists of a catalytically grown hollow fishbone-type structure, whereas the outer layer consists of

disordered, pyrolytically grown structure, parallel to the main axis of the tube and with a thickness of about 5–6 nm. Due to the poorly ordered carbon surface, these CNTs offer a large number of sites for functionalization. The nature of the functional groups on the carbon surface plays an important role when the CNTs are used as support for catalyst. The properties of the CNTs and of the gas diffusion layer (GDL) are shown below in *Table 2.1*.

Table 2.1 Properties of commercial GDL and CNTs

Properties of GDL 25 BC Sigracet®		Properties of CNTs PR-24-XT-PS Pyrograf®	
<i>Thickness</i>	235 μm	<i>Surface area</i>	45 m^2/g
<i>Areal weight</i>	86 g/m^2	<i>Moisture</i>	<5 wt. %
<i>Porosity</i>	80 %	<i>Iron</i>	<14,000 ppm
<i>Air permeability</i>	1.0 $\text{cm}^3/(\text{cm}^2 \text{ s})$	<i>Fiber diameter (average)</i>	100 nm
<i>Electrical resistance (through plane)</i>	<12 $\text{m}\Omega \text{ cm}^2$	<i>Dispersive surface energy</i>	85 mJ/m^2 :
		<i>Polyaromatic hydrocarbons</i>	<1 mg PAH/g fiber

The CNTs were annealed in inert gas (750°C) to remove the polyaromatic carbon layer covering their outer surface. The functionalization of the CNTs was then made by an oxidative treatment in HNO_3 to introduce oxygen functionalities on the carbon surface: in detail, a suspension of 1 g of CNTs in 50 ml HNO_3 was maintained in reflux at 100°C for 2 h, followed by rinsing until neutral pH, filtering, and drying overnight. Different types of oxygen functionalities were introduced by this treatment. Their total amount and relative distribution can vary as a function of the annealing post-treatment in inert atmosphere, as shown from synchrotron radiation XPS data ^[24].

Metal nanoparticles (NPs) were then deposited by incipient wetness impregnation using an ethanolic solution containing the metal precursor(s). In detail, $\text{Fe}(\text{NO}_3)_3 \cdot 9\text{H}_2\text{O}$, $\text{Cu}(\text{NO}_3)_2 \cdot 3\text{H}_2\text{O}$, $\text{Co}(\text{NO}_3)_2 \cdot 6\text{H}_2\text{O}$ and $\text{H}_2\text{PtCl}_6 \cdot 6\text{H}_2\text{O}$ (72 mg, 38 mg, 49 mg and 27 mg, respectively, equivalent to 10 % of metal by weight with respect to the CNTs) was added to a mixture of 1 ml of ethanol and 0.2 ml of water and sonicated for 10 minutes. This metal amount was chosen to have a good comparison with the electro-catalysts used for PEM fuel cells (usually use 10-20 wt. % loading corresponding to $\sim 0.5 \text{ mg}/\text{cm}^2$ in the final catalyst). Then, the concentrated metal NPs solutions were impregnated onto CNTs by incipient wetness impregnation technique, by adding drop by drop till it slightly wetted the carbon substrate, then dried in the oven at a temperature slightly above the boiling point of solvent (80°C) for 24 h. The samples were annealed for 2 h at 350 °C and finally reduced in H_2 at 400 °C for 2 h.

This procedure led to well-dispersed metal nanoparticles, with an average size between 10 and 20 nm for iron or other non-noble metals, such as Co and Cu, while smaller average size (between 1 and 3 nm) for noble metals such as Pt ^[19].

2.1.1.2. Assembling of the electrodes

To prepare the electrode a similar procedure was used. In detail, 10 mg of this metal doped CNTs were mixed with 1 ml of ethanol and a drop of Nafion per-fluorinated resin (acting as a binding agent) and then sonicated for 30 minutes to get a dark black INK formulation. This INK was coated onto the GDL (on the top-side modified with Teflon coating) by impregnation. The final working electrode was assembled joining the GDL on a selective proton membrane (Nafion 115) by hot-pressing at 80 atm and 130 °C for 90 s. The active electro-catalyst is located between the GDL at direct contact with CO₂ in the gas phase and the Nafion membrane layer. Before its use, the Nafion membrane was treated with H₂O₂ to remove organic impurities and then in H₂SO₄ for activation.

2.1.1.3. Gas phase cell model and testing of the electrodes

The electro-catalytic tests of CO₂ conversion were carried out in a lab-scale (size of about 1.5 cm in diameter for the electrode) semicontinuous electro-catalytic reactor operating at 60 °C. This cell simulated the cathodic part of a full PEC cell. *Fig. 2.1* reports the schematic diagram of the apparatus and a photo of the PEC hemi-cell used in these experiments. The PEC hemi-cell has a three-electrode configuration, with a Pt wire (as counter-electrode) and a saturated Ag/AgCl electrode (as reference electrode) immersed in the simulator batch. The anode side of the cell (e.g., the side of the cell in contact only with Nafion membrane, but not with the electro-catalyst located on the other side of the cell) is filled with an electrolyte solution (0.5 M solution of KCl or KHCO₃) used to provide the protons needed for the reduction, which diffuse to the electro-catalyst through the Nafion membrane. The cathodic side of the cell operates in contact with a gas flow of 100% CO₂. A potentiostat/galvanostat (Amel mod. 2049A) was used to supply a constant current (in the range 10-20 mA) between the electrodes. The voltage increases as a function of time-on-stream during the first hour stabilizing to a value of about around -1.4 to -1.5 V. At the end of the reaction (typically, 1 h), the current polarity was inverted to facilitate desorption of the products from the working electrode. The liquid products were collected in a cold trap and analysed by a gas chromatograph equipped with a mass detector ^[19].

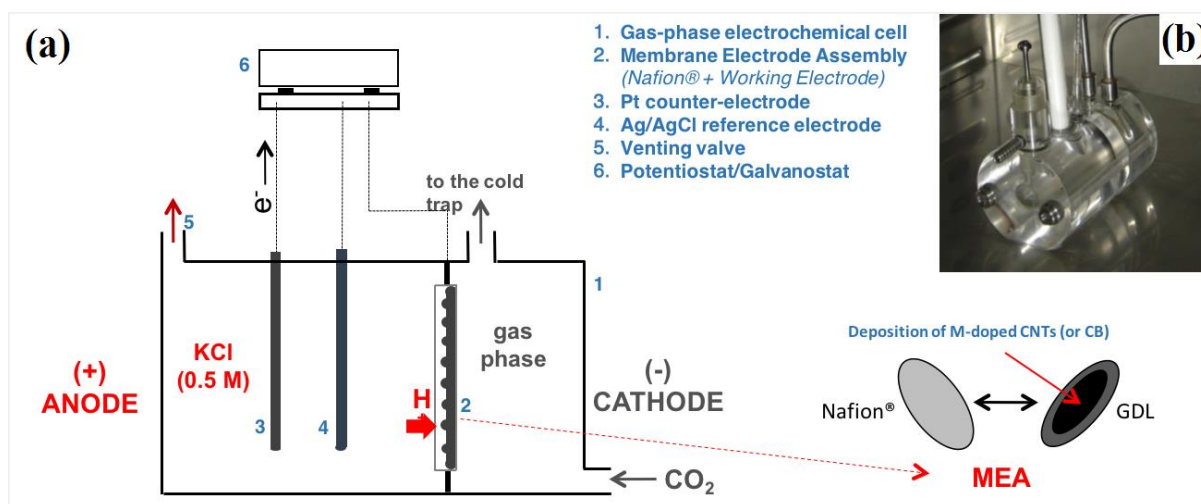


Fig. 2.1 (a) Scheme of the apparatus for electrolyte-less cell tests of CO₂ reduction with the electro-catalyst in contact with a gaseous flux of CO₂. (b) Photo of the cell; in the inset view of the electrode and GDL.

2.1.1.4. Importance of nano-carbon based substrates

The carbon support plays multiple roles: (i) it allows the dispersion of the metal nanoparticles and (ii) it determines the effectiveness of transport of electrons and protons to the metal nanoparticles for the electro-reduction of CO₂.

Even if carbon black materials (i.e Ketjen and Vulcan) also show some activity as conductive substrates for metal nanoparticles for the conversion of CO₂, the use of nanocarbons is critical to obtain good performances and control the selectivity in CO₂ reduction. This indicates that the carbon substrate does not play only a role as a conductive support, neither only it changes the dispersion of supported metal particles. There was in fact a visible difference in the catalytic activity of the electrodes based on Fe on Vulcan XC-72 (Carbon Black) and Fe on CNTs [19]. It was found that the higher number of sites were responsible for the formation of >C1 products in Fe/CNTs with respect to electro-catalysts based on Fe deposited on conventional conductive carbon black, even if there were no apparent differences in terms of iron nanoparticles sizes and distribution between these samples. Thus, the type of carbon is relevant, both in terms of nanostructure with carbon nanotubes allowing a double productivity with respect to commercial conductive carbon materials (carbon black), and in terms of nature of the surface sites and interaction with the metal nanoparticles.

Moreover, other studies concluded that bare CNT functionalized with oxygen functionalities or N₂-doped CNTs (also without metal NPs) showed different productivity results [25]. For instance, the modification of CNTs by introduction of N (N-CNTs) as support for iron, leads to a double activity and a significant change in the product distribution, with maximization of the isopropanol formation as reported by Arrigo et al. [25] This behaviour was explained by the effect of the smaller Fe particles present on Fe/N-CNTs with respect to Fe/CNTs.

2.1.1.5. Fuel productivity and selectivity

The studies conducted by Centi and Perathoner's research group on electrocatalytic conversion of gaseous streams of CO₂ back to liquid fuels, showed novel pathways for the CO₂ electro-reduction and the fuel productivity values reported were quite interesting. Moreover, the different kinds of products obtained in gas-phase reactions, provide a series of interesting indications both on the limiting steps of the process and on the reaction mechanism, evidencing possible differences in the reaction pathway in operations in the presence (liquid-phase) or absence (gas-phase) of a bulk electrolyte. The productivity data at 60°C for different metal doped CNTs reported are shown in the *Table 2.2* from literature [19].

Table 2.2 Productivity for the CO₂ EC reduction in gas phase cell (Units: $\mu\text{mol}\cdot\text{hr}^{-1}$) [19].

Catalysts		FUELS ($\mu\text{mol}\cdot\text{hr}^{-1}$)		
		CO	H ₂	C-Products (NET)
BASIC	Pt-CNT	18.0	165.0	1.6e-1
	Fe-CNT	35.0	149.0	2.1e-1
	Cu-CNT	40.0	157.0	1.4e-1
	Co-CNT	32.0	135.0	1.9e-1
MIXED	FeCu-CNT (50% each)	15.0	174.0	4.0e-1
	FeCuCo-CNT (40, 40, 20 %)	18.0	161.0	3.8e-1

Pt-CNTs resulted more stable and gave in some cases a higher productivity, but Fe-CNTs had excellent properties and can be preferable to noble-metal based electrocatalysts for the lower cost. Formation of bi-metallic and tri-metallic nanoparticles of Fe with Co and/or Cu were shown to increase the productivity, particularly with copper, although Cu itself showed poor performances. However, also the type of carbon is relevant, both in terms of nanostructure (CNTs allow a double productivity with respect to commercial conductive carbon materials) and in terms of nature of the surface sites and interaction with the metal nanoparticles.

2.1.2. Scope of the chapter

The central idea of the research work presented in this chapter is to probe into the strategies towards improvement of the CO₂ reduction (in EL conditions). Various parameters could be changed to improve the efficiency of the process such as nature of electrodes, phase of the nanoparticles (NPs), and CO₂ adsorption ability of the gas diffusion layers. Refer to this latter aspect, Metal-organic framework (MOF), have attracted considerable attention in the last years owing to their characteristics such as high porosity, high surface area and high chemical stability [26-31]. The most important property of MOFs materials is the well-known intrinsic capability of CO₂ adsorption [26-29]. Thus, to improve the performances of the electrocatalyst in the gas phase reduction of CO₂ process, the GDL was first modified using MOFs by designing a proper procedure to successfully coat the GDL with MOFs. We used a well-established methodology to synthesize MOFs, which was developed in one of our laboratories in IRCE Lyon [32, 33]. A substituted Zeolitic Imidazolate MOF (SIM-1) was prepared and subsequently transferred onto GDL. The objective of the work was to understand the effect of the MOFs on the CO₂ reduction in gas phase. The final working electrodes were prepared as described above and then the MOF modified working electrodes were tested for their catalytic performance on CO₂ reduction using the same conditions reported in the *paragraph 2.1.1.3*.

2.2. Experimental

2.2.1. SIM 1 - MOF synthesis

Prior to synthesis, the GDL was fixed in a Teflon casing with the top side having an opening equivalent to the catalytic area of the electrode in the gas phase cell. Moreover, the Teflon casing was taped (Teflon tape) properly on all the sides, to deposit the MOF only in the catalytic area. The support was then immersed vertically in a vial containing 0.71 g (2.73 mmol) of Zn(NO₃)₂•4H₂O and 1.20 g (10.94 mmol) of 4-methyl-5-imidazolecarboxaldehyde dissolved in 20 ml of DMF. After a solvo-thermal treatment at 358 K for 48 h, the resulting supported material was washed with ethanol to remove unreacted precursors and fine SIM-1 unsupported particles. The SIM-1 supported was then dried at room temperature. This synthesis route is shown in the literature [32, 33]. Finally, the GDL back-side (the opposite-side of catalytic layer) was coated with a thin micro MOF layer as shown in *Fig. 2.2*.

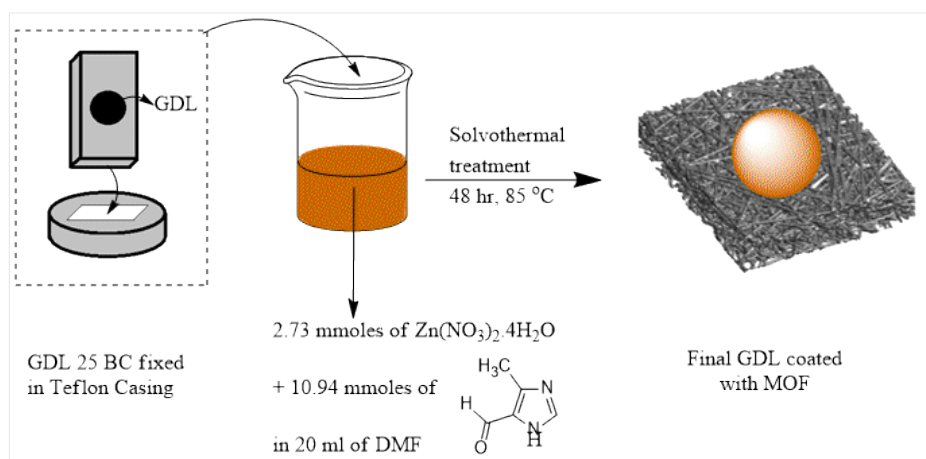


Fig. 2.2 Scheme showing MOF synthesis and transfer onto GDL

2.2.2. Working electrode configuration (final template)

The working electrode was prepared by depositing a thin layer of CNTs (doped with Pt, Fe or Cu) on the MOF/GDL (this time on the top-side of GDL). The resulting MOF/GDL/(metal)CNTs was finally hot pressed with a Nafion membrane as reported above in the paragraph 2.1.1.2. *Fig. 2.3* shows a scheme of the procedure. It is to take into account the thickness of the MOF as an additional parameter in analysing the fuel productivity values, since the addition of MOF is effectively equivalent to add catalytic materials, thus altering the electron conductivity and proton diffusion. For this configuration, the CNTs and MOFs are on the opposite sides of GDL, which have a noticeable effect on the electron flow and on the performances in CO_2 reduction.

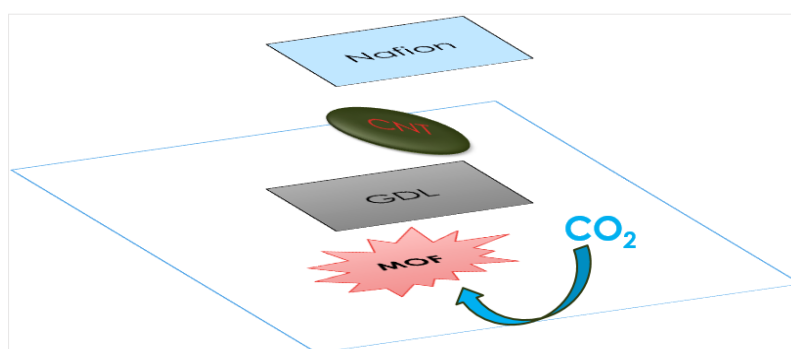


Fig. 2.3 Scheme showing the configuration of the final electrode template.

2.3. Results and Discussions

2.3.1. Characterization

The catalysts were characterized using different techniques to determine the physical and structural properties. The characterizations include AAS, BET, HRTEM, SEM, XPS and XRD. Apart from SEM analysis, rest of the characterizations will be given in detail in [Chapter 3](#).

2.3.1.1. SEM Morphological Measurements

[Fig. 2.4](#), shows the lateral view of the GDL with MOF and [Fig. 2.5](#), shows the deposition of the MOFs crystals on the fibre like structures of the bottom-side of GDL. From the [Fig. 2.6](#), it was found that the MOF thickness is around 15-25 μm (i.e. 2 or 3 layers of MOF crystals; each crystal size $\sim 7.5 \mu\text{m}$). The weight of the MOF layer deposited was found to be 5-9 mg (calculated by subtracting the initial weight of GDL from net final weight of GDL+MOF layer).

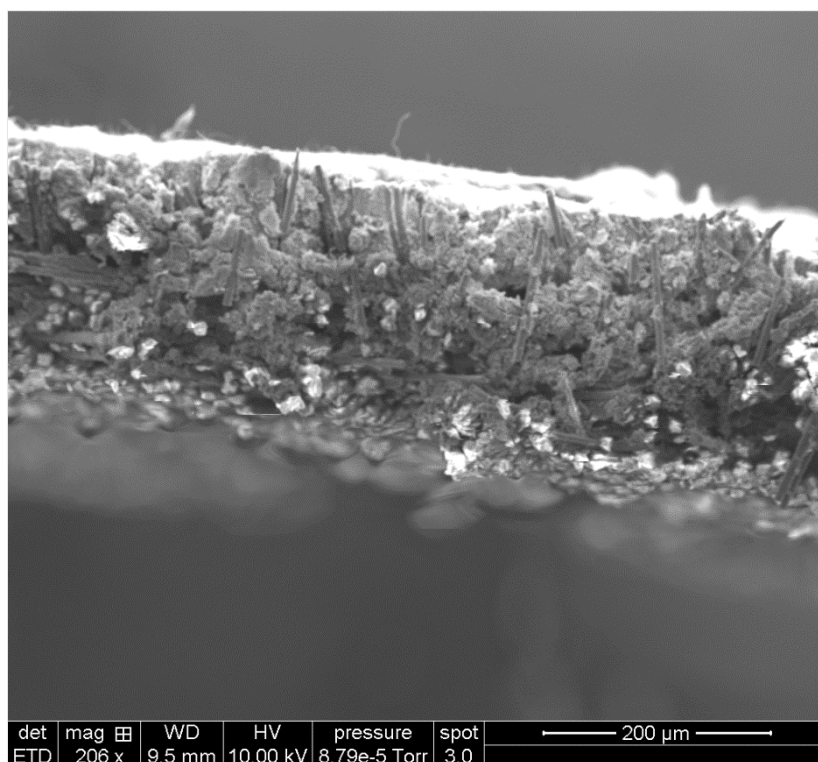


Fig. 2.4 SEM image of the GDL with MOF cross-sectional view.

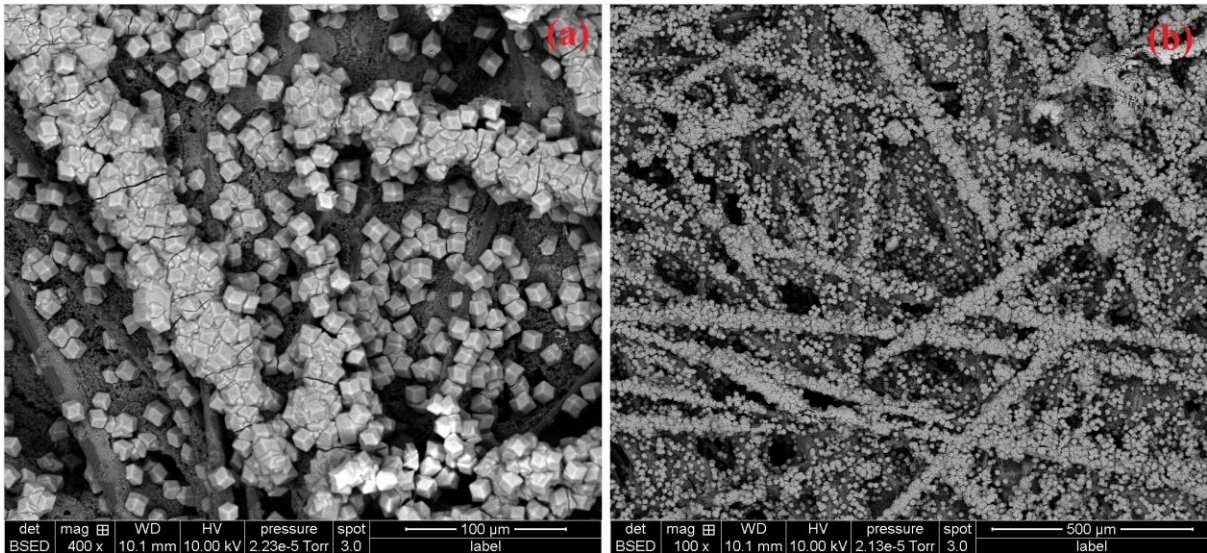


Fig. 2.5 SEM images showing the deposition of the MOFs crystals on the fibres of GDL.

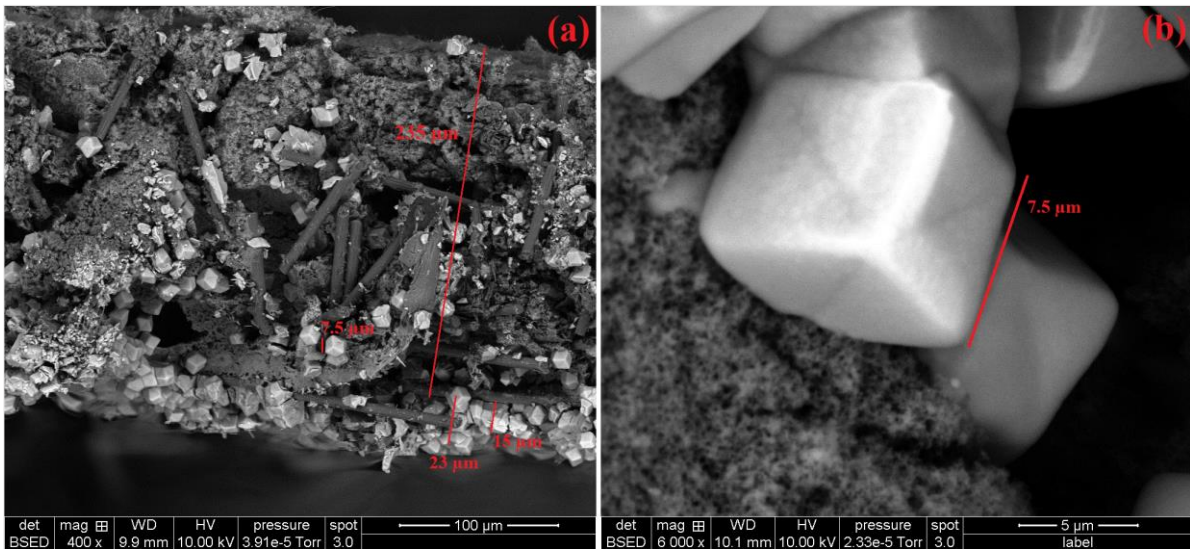


Fig. 2.6 SEM image showing the thickness of the MOF layer and the GDL.

2.3.2. Electro-catalytic CO₂ reduction in Gas phase

2.3.2.1. Voltage profile

Fig. 2.7 shows the voltage (V) variation as a function of time (t, min), for the two phases of adsorption (current = -10 mA) and desorption (current = +10 mA). The shift in phase is done at t= 1 h of the reaction. The voltage values ranged from -1.67 to + 3.74 for the Pt-CNT-MOF electrode and -1.45 to + 2.24 for the Fe-CNT-MOF electrode.

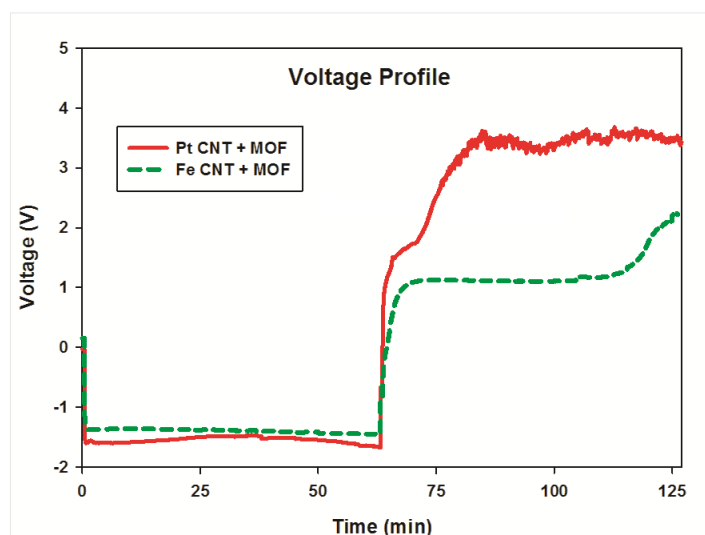


Fig. 2.7 Voltage profiles for MOF modified Pt, Fe – CNTs gas phase reaction.

2.3.2.2. Fuel productivity

The results obtained for the MOF coated Fe, Pt, or bimetallic CuFe doped CNTs based electrodes in the gas phase reduction of the CO₂ are presented in the [Table 2.3](#). Pt-CNT-MOF, allowed to increase the net carbon products (C-products) by 1.5 times and to decrease the hydrogen evolution reaction (HER) by 2 times in comparison with basic Pt-CNT electrode. The selectivity shifted towards C₂H₅OH and isopropanol in addition to CO. Small amounts of acetone were also observed. By using Fe-CNT-MOF, there was a decrease by 20% in the net C-products while an increase in the side reaction (HER) by 1.6 times was noticed in comparison with basic Fe-CNT electrode. The selectivity was also shifted from C₂H₅OH towards CH₃OH. In the case of CuFe-CNT-MOF, the net C-products is found to be 50 % lower compared to Fe-CNT-MOF and Pt-CNT-MOF, so further experimentation is needed to clarify this behaviour.

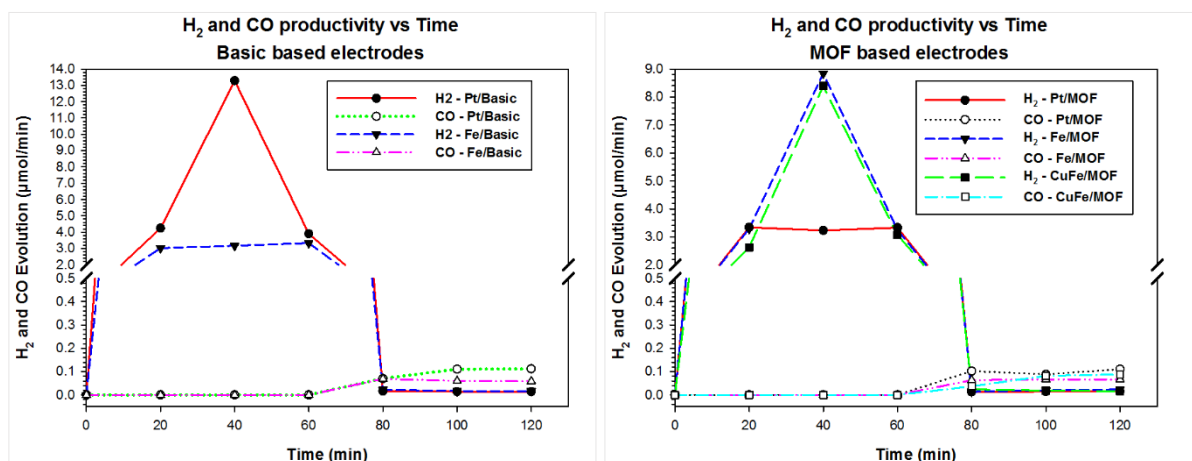


Fig. 2.8 H₂ and CO productivity in (µmol/min) vs Time (min).

Table 2.3 Productivity for the CO₂ EC reduction in gas phase cell (Units: $\mu\text{moles per hr}$).

CATALYSTS		FUELS ($\mu\text{mol}\cdot\text{hr}^{-1}$)						
		<i>Methanol</i>	<i>Ethanol</i>	<i>Acetone</i>	<i>Iso - propanol</i>	<i>CO</i>	<i>H₂</i>	<i>C-Products (NET)</i>
MOF	<i>Pt-CNT-MOF</i>	1.5e0	4.1e-1	1.6e-3	4.1e-1	6.0	190	2.3
	<i>Fe-CNT-MOF</i>	1.3e0	3.9e-1	4.9e-4	4.1e-1	3.9	310	2.1
	<i>CuFe-CNT-MOF</i>	8.7e-1	-	1.1e-3	1.6e-1	4.1	280	1.1
BASIC	<i>Pt-CNT</i>	1.3e-0	-	-	1.5e-1	5.8	430	1.5
	<i>Fe-CNT</i>	-	2.3e0	1.7e-3	4.4e-1	3.7	190	2.7

Fig. 2.8 shows the gas productivity values as a function of reaction time. Initially, H₂ is the main product of reaction, but after about 1 h of time of stream (by inverting polarity) its formation stops and CO start to be detected, together with >C1 products of reaction, in agreement with those previously observed by Genovese et al. [19]. Therefore, when the side reaction of recombination of protons/electrons were suppressed by inverting polarity, CO can form selectively and liquid fuels can desorb from these electrocatalysts.

2.4. Conclusions

The SIM-1 type MOFs were synthesized and successfully coated onto the GDL to study the improvements in the CO₂ adsorption and in the electro-catalytic CO₂ reduction to fuels in electrolyte-less conditions (gas phase). The catalysts tested were MOF based Fe-CNT, Pt-CNT, and CuFe-CNT, and results were compared with those obtained from testing the basic electrodes (Pt/CNTs and Fe/CNTs). This can be considered as the initial step into understanding the effects of supplementing the working electrode with materials able to enhance CO₂ adsorption such as MOFs.

The results showed some improvements in the fuel productivity values and a shift in the selectivity of various products. This sheds light on the MOFs influence on the reaction mechanism and not just as a boost to the CO₂ adsorption. By using Pt-CNT-MOF as electrode, (i) the C-products improved by 1.5 times, (ii) the H₂ evolution decreased by 2 times and (iii) a great shift in the selectivity towards ethanol and iso-propanol was observed compared to basic Pt-CNT electrode. For the case of Fe-CNT-MOF, instead, the C-products amount decreased by 20% and the H₂ evolution increased by 1.6 times. However, the CuFe-CNT-MOF catalyst did not show promising results.

Further work needs to be undertaken, in order to get a deeper understanding of the effects of MOF on the electro-catalytic gas phase CO₂ reduction. The prospective studies can be addressed to the testing of an electrode without the metal doped CNTs (only MOF doped GDL), to see the MOF real effect on the fuel productivity and selectivity. Moreover, a study to see the influence of the CO₂ concentration or using a mixture of gases (N₂, O₂, etc.) to simulate a near atmospheric CO₂ content, can be made. Further investigation into the lifetime of the MOF based electrodes needs to be reviewed by re-using the same electrode for testing.

2.5. References

- [1] J. Albo, M. A. Guerra, P. Castano, A. Irabien, *Green Chem.*, 2015, **17**, 2304.
- [2] P. Kang, Z. Chen, M. Brookhart, T.J. Meyer, *Top. Catal.*, 2015, **58**, 30.
- [3] Q. Lu, J. Rosen, F. Jiao, *ChemCatChem*, 2015, **7**, 38.
- [4] E.S. Rountree, B.D. McCarthy, T.T. Eisenhart, J.L. Dempsey, *Inorg. Chem.*, 2014, **53**, 9983.
- [5] J. Qiao, Y. Liu, F. Hong, J. Zhang, *Chem. Soc. Rev.*, 2014, **43**, 631.
- [6] E.V. Kondratenko, G. Mul, J. Baltrusaitis, G.O. Larrazabal, J. Perez-Ramirez, *Energy & Env. Science*, 2013, **6**, 3112.
- [7] S. Bensaid, G. Centi, E. Garrone, S. Perathoner, G. Saracco, *ChemSusChem*, 2012, **5**, 50.
- [8] D. G. Nocera, *Acc. Chem. Res.*, 2012, **45**, 767.
- [9] G. Centi, S. Perathoner, in *Chemical Energy Storage*, R. Schlögl Ed., De Gruyter 2013, 379.
- [10] K.S. Joya, Y.F. Joya, K. Ocakoglu, R. van de Krol, *Angew. Chemie, Int. Ed.* 2013, **52**, 10426.
- [11] J. Barber, P.D. Tran, *J. Royal Soc. Interface*, 2013, **10**, 20120984.
- [12] S. Fukuzumi, Y. Yamada, *ChemSusChem*, 2013, **6**, 1834.
- [13] D.K. Bora, A. Braun, E.C. Constable, *Energy & Env. Science*, 2013, **6**, 407.
- [14] G. Centi, S. Perathoner, Artificial leaves, in *Kirk-Othmer Encyclopedia of Chemical Technology*, 2014.
- [15] G. Centi, S. Perathoner, *Catal. Today*, 2003, **77**, 287-297.
- [16] G. Centi, S. Perathoner, G. Wine, M. Gangeri, *Green Chem.*, 2007, **7**, 671.
- [17] C. Ampelli, G. Centi, R. Passalacqua, S. Perathoner, *Energy & Env. Sci.*, 2010, **3**, 292.

- [18] C. Ampelli, C. Genovese, R. Passalacqua, S. Perathoner, G. Centi, *Theor. Found. Chem. Eng.*, 2012, **46**, 651-657.
- [19] C. Genovese, C. Ampelli, S. Perathoner, G. Centi, *J. Catal.*, 2013, **308**, 237-249.
- [20] C. Ampelli, S. Perathoner, G. Centi, *Chinese J. Catal.*, 2014, **35**, 783.
- [21] C. Ampelli, C. Genovese, M. Errahali, G. Gatti, L. Marchese, S. Perathoner, G. Centi *Chem. Eng. Trans.*, 2015, **45**, 701-713.
- [22] C. Ampelli, C. Genovese, B.C. Marepally, G. Papanikolaou, S. Perathoner, G. Centi, *Faraday Discuss.*, 2015, **183**, 125-145.
- [23] C. Ampelli, G. Centi, R. Passalacqua, S. Perathoner, *Catal. Today*, 2016, **259**, 246-258.
- [24] C. Genovese, C. Ampelli, S. Perathoner, G. Centi, *J. Energy Chem.*, 2013, **22**, 202.
- [25] R. Arrigo, M. E. Schuster, S. Wrabetz, F. Girgsdies, J. P. Tessonnier, G. Centi, S. Perathoner, D. S. Su, R. Schlögl, *ChemSusChem*, 2012, **5**, 577.
- [26] K. Sumida, D. L. Rogow, J. A. Mason, T. M. McDonald, E. D. Bloch, Z. R. Herm, T. H. Bae, J. R. Long, *Chem. Rev.*, 2012, **112**, 724-781.
- [27] A. L. Dzubak, L. C. Lin, J. Kim, J. A. Swisher, R. Poloni, S. N. Maximoff, B. Smitt, L. Gagliardi, *Nat. Chem.*, 2012, **4**, 810-816.
- [28] A. H. Lu, G. P. Hao, *Annu. Rep. Prog. Chem., Sect. A: Inorg. Chem.*, 2013, **109**, 484-503.
- [29] J. M. Simmons, H. Wu, W. Zhou, T. Yildirim, *Energy Environ. Sci.*, 2011, **4**, 2177.
- [30] I. Luz, A. Corma, F. X. L. Xamena, *Catal. Sci. Technol.*, 2014, **4**, 1829.
- [31] J. J. Baldovi, E. Coronado, A. G. Arino, C. Gamer, M. G. Marques, G. M. Espallargas, *Chem. Eur. J.*, 2014, **20**, 10695-10702.
- [32] S. Aguado,* J. Canivet and D. Farrusseng, *J. Mater. Chem.*, 2011, **21**, 7582-7588.
- [33] M. Baias, A. Lesage, S. Aguado, J. Canivet, V. M. Basle, N. Audebrand, D. Farrusseng, and L. Emsley, *Angew. Chem. Int. Ed.*, 2015, **54**, 5971-5976.

ANNEX²

Materials and Reagents:

Chemicals used in our synthesis route are copper (II) nitrate trihydrate [Cu(NO₃)₂.3H₂O], Iron (III) nitrate nonahydrate [Fe(NO₃)₃.9H₂O], chloroplatinic acid hexahydrate [H₂PtCl₆.6H₂O], Ruthenium Chloride hydrate (RuCl₃. xH₂O), Zinc (II) nitrate tetrahydrate [Zn(NO₃)₂.4H₂O], 4-methyl-5-imidazolecarboxaldehyde [C₅H₆N₂O], nitric acid (HNO₃, 65%), sulphuric acid (H₂SO₄, 95%), absolute ethanol (98 %), dimethyl formamide [DMF] potassium bicarbonate (KHCO₃, 99.7%), Nafion perfluorinated resin were obtained from Sigma-Aldrich and used without any further purification. Commercial carbon nanotubes (CNTs, PR-24-XT-PS) were bought from Pyrograf® and were pre-treated before use. Vulcan XC 72 (carbon black) was brought from Akrochem© and was pre-treated before use. Gas diffusion layer (GDL 25 BC) was obtained from Sigracet®. Nafion membrane (Nafion 115 and 117) was obtained from Ion power and was pre-treated before use.

Characterization Tools:

Scanning electron microscopy (SEM):

All the SEM images were obtained by Phenom ProX Scanning Electron Microscope (SEM) at the “Centre Technologiques des Microstructures”, CTμ, Villeurbanne, France.

CHAPTER 3

Design and performance of a novel liquid phase cell for CO₂ electro-reduction

3.1 Introduction

3.1.1. State of the art

As one of the sub-parts of the broader research area of solar fuels [1-10] towards a single compact artificial photosynthetic system [7, 11] to achieve sustainable low-carbon energy and chemical production [12-16], CO₂ electrocatalytic reduction [17-23] to fuels has quite often been studied. A lot of research went into this field from more than a century. Different kinds of catalysts have been researched which include metallic electrodes [24-30], metallic nanoparticles [26, 28, 29], nanostructures [31], homogenous and heterogeneous catalysts [32-35] and many computational studies [25]. Many studies were conducted either to increase the selectivity towards a desired product or to increase the net productivity of the reaction [36, 37].

Not many studies have been undertaken towards the cell design, which in reality plays a significant role in effecting the productivity of the CO₂ reduction reactions. Most of the CO₂ reduction research works reported in literature [38-42], use the basic three-electrode configuration given in *annex³*. This standard configuration has many shortcomings such as i) O₂ and H₂ formed by water splitting reaction (or fuels coming from CO₂ reduction) evolve in the same environment, creating safety problems and need to separate the products; ii) the electrodes are usually too distant each other causing high overpotential due to the charge diffusion in the electrolyte solution; iii) the electrodes are not designed to be used in compact devices for a delocalized production of energy; iv) the electrolyte is the same for both the half-reactions; v) the gas flow is not properly distributed on the electrode surface.

The conditions used for the CO₂ reduction in most of the works are quite different, which include potential/current applied, solvent, membrane, electrode kind, etc [38-44]. These details including performances from literature are presented in the *Table 3.1* below. A concrete statement cannot be made from these results comparing with the results obtained by our catalytic electrodes in liquid phase reactions but the gas phase results can be better understood scaling with these results. This is due to the reasons aforementioned (multi-variable conditions).

The importance of moving towards electrolyte-less (EL) systems is also ignored considering not many studies accounted for the cell design in the CO₂ reduction process.

Table 3.1 A review of the various conditions and the results of CO₂ electro-reduction.

Electrodes	E vs. NHE (V)	Major Products	Faradaic Efficiency (%)	Current Density (mA cm ⁻²)	Reference	Electrolyte
CuO	- 1.3	CH ₃ OH, CO	28	6.9	[44]	0.5 M KHCO ₃
Pt-Ru/C	- 0.06	CH ₃ OH, CO	7.5	0.04	[45]	Flow cell
RuO ₂ /TiO ₂ nanotubes	- 0.6	CH ₃ OH	60	1	[46]	0.5 M NaHCO ₃
Au/C	- 2.22	HCOO ⁻	64	200	[47]	0.5 M KHCO ₃
Ag	- 2.96	CO	53	100	[48]	0.5 M K ₂ SO ₄
Sn	- 2.7	HCOO ⁻	91	60	[49]	0.45 M KHCO ₃ + 2 M KCl
Cu Foil	- 1.2	CH ₄ , CO	40	10	[41], [43]	0.1 M KHCO ₃
Cu ₂ O derived Cu	- 1.0	C ₂ H ₄ , C ₂ H ₅ OH, CO	45	50	[39]	0.1 M KHCO ₃
Co protoporphyrin	- 1.4	CH ₄ , CO	7	2.7	[40]	0.1 M HClO ₄

Centi and Perathoner's research group, the only distinctive one, has successfully explored the CO₂ reduction in gas-phase, as exhaustively discussed in *Chapter 2*.^[27, 50-57], which bring us closer to the future goal towards a viable artificial leaf^[7, 10, 58-63]. The electrode design for these kinds of cells is a challenge in-itself as in the liquid phase the gas flow is not an issue, except for the CO₂ solubility. So, careful design and understanding towards these types of electrodes is one of the aspects of these studies.

3.1.2. Scope of the chapter

The central idea behind the research work presented in this chapter is to bridge the gas phase results with the ones presented in literature (based on conventional liquid phase cells). The goal is to utilize the same type of electrodes (nanoparticles based nanocarbon electrodes) and reaction conditions, except for the presence of the liquid bulk electrolyte, in order to compare conventional liquid phase and EL approaches, determine more precisely the differences in the productivity and type of products, and obtain indications about possible differences in the reaction mechanism.

The particular objectives of this chapter are to discuss the development of a novel liquid phase electro-catalytic (EC) cell, the challenges faced during the construction of the cell and the performances of the catalytic tests in this liquid phase cell. The electrodes were made from various metal nanoparticle doped carbon (carbon nanotubes – CNT – or carbon black – CB)

catalysts deposited onto a Gas Diffusion Layer (GDL). The design of the working electrode based on GDL is very similar to the one used in gas phase (except for the Nafion assembly), thus to have a better comparison between the two systems.

3.2 Experimental

This section covers the synthesis of the catalytic electrode materials, the electrode assembly and the conditions used to perform the CO₂ electro-catalytic reactions.

3.2.1. Preparation of the Electrodes

The electrode preparation can be summed-up into a three-step process:

Step 1: Synthesis of metal nanoparticles (NPs) suspended in a solvent;

Step 2: Transfer of the metal NPs onto commercial carbon substrates (CNTs, PR-24-XT-PS Pyrograf);

Step 3: Deposition of metal NPs decorated CNTs on the gas diffusion layer (GDL) to form the working electrode. The catalyst deposition was made on the opposite side of the Teflon modified base of the GDL.

Table 3.2 shows the basic properties of these materials used to prepare the working electrodes.

Table 3.2 Properties of commercial GDL and CNTs. (refer - *Pyrograf*®)

Properties of GDL 25 BC Sigracet®		Properties of CNTs PR-24-XT-PS Pyrograf®	
<i>Thickness</i>	235 μm	<i>Surface area</i>	45 m ² /g
<i>Areal weight</i>	86 g/m ²	<i>Moisture</i>	<5 wt.%
<i>Porosity</i>	80 %	<i>Iron</i>	<14,000 ppm
<i>Air permeability</i>	1.0 cm ³ /(cm ² s)	<i>Fiber diameter (average)</i>	100 nm
<i>Electrical resistance (through plane)</i>	<12 mΩ cm ²	<i>Dispersive surface energy</i>	85 mJ/m ² :
		<i>Polyaromatic hydrocarbons</i>	<1 mg PAH/g fiber

The PR-24-XT-PS CNTs have an average diameter of about 100 nanometers with an external stacked-ring type structure and the graphitic inner core is tubular shaped aligned along the main axis. These CNTs were heated at 750°C to remove polyaromatic hydrocarbons from their surface. Due to the stacked-cup structure, there are several graphitic edges that act as excellent sites for functionalization on the external surface.

The composition of the functional groups on the Vulcan (carbon black) / CNT surface has a major role in the catalytic activity. Thus, a direct oxidative treatment using concentrated HNO_3 was performed on the Vulcan / CNTs, introducing various surface oxygen functionalities. In detail, 1 g of Vulcan / CNTs were added to 50 mL of conc. HNO_3 and treated in reflux setup at 100°C for 3 h, followed by washing until neutral pH, filtering, and drying overnight, leading to formation of oxygen functionalities as shown in the [Fig. 3.1](#). The total quantity and relative distribution can vary as a function of the annealing post-treatment in inert atmosphere [\[23\]](#).

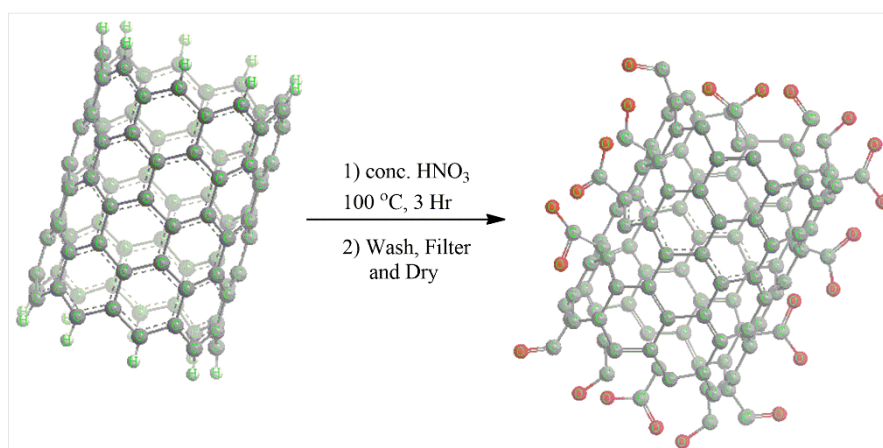


Fig. 3.1 A Schematic showing treating CNTs to obtain oxygen functionalities.

Step 1: Synthesis of metal nanoparticles via Impregnation (ImR) route

The precursor, 72 mg, 38 mg, 27 mg, 26 mg and 27 mg of $\text{Fe}(\text{NO}_3)_3 \cdot 9\text{H}_2\text{O}$, $\text{Cu}(\text{NO}_3)_2 \cdot 3\text{H}_2\text{O}$, $\text{Co}(\text{NO}_3)_2 \cdot 6\text{H}_2\text{O}$, $\text{RuCl}_3 \cdot x\text{H}_2\text{O}$ and $\text{H}_2\text{PtCl}_6 \cdot 6\text{H}_2\text{O}$ respectively, (equivalent to 10 wt. % of metal with respect to CNTs) was added to a mixture of 1 ml of ethanol and 0.2 ml of water and sonicated for 10 minutes. The reason for this choice of weight for the salt was to have a good comparison of metal loading with the electrocatalysts for PEM fuel cells (usually use 10-20 wt. % loading corresponding to $\sim 0.5 \text{ mg}/\text{cm}^2$ in the final catalyst).

Step 2: Transfer of metal nanoparticles onto CNTs

The 1 ml concentrated metal NPs solutions were impregnated onto 100 mg CNTs by incipient wetness impregnation technique, by adding drop by drop till it slightly wetted the carbon substrate, then dried in the oven at a temperature slightly above the boiling point of solvent used (70°C for THF and 115°C for toluene). This process was repeated until 1 ml metal NPs solution was completely exhausted. The final sample was dried overnight in an oven at 70°C

or 115 °C, as may be the case. Finally, the metal decorated carbon samples were annealed for 2 h at 350 °C (ramp rate 6 °C/min) under H₂ flow (25 ml/min). A schematic of the same can be seen in [Fig. 3.2](#). Also, reported through XPS data in [Fig. 3.7](#).

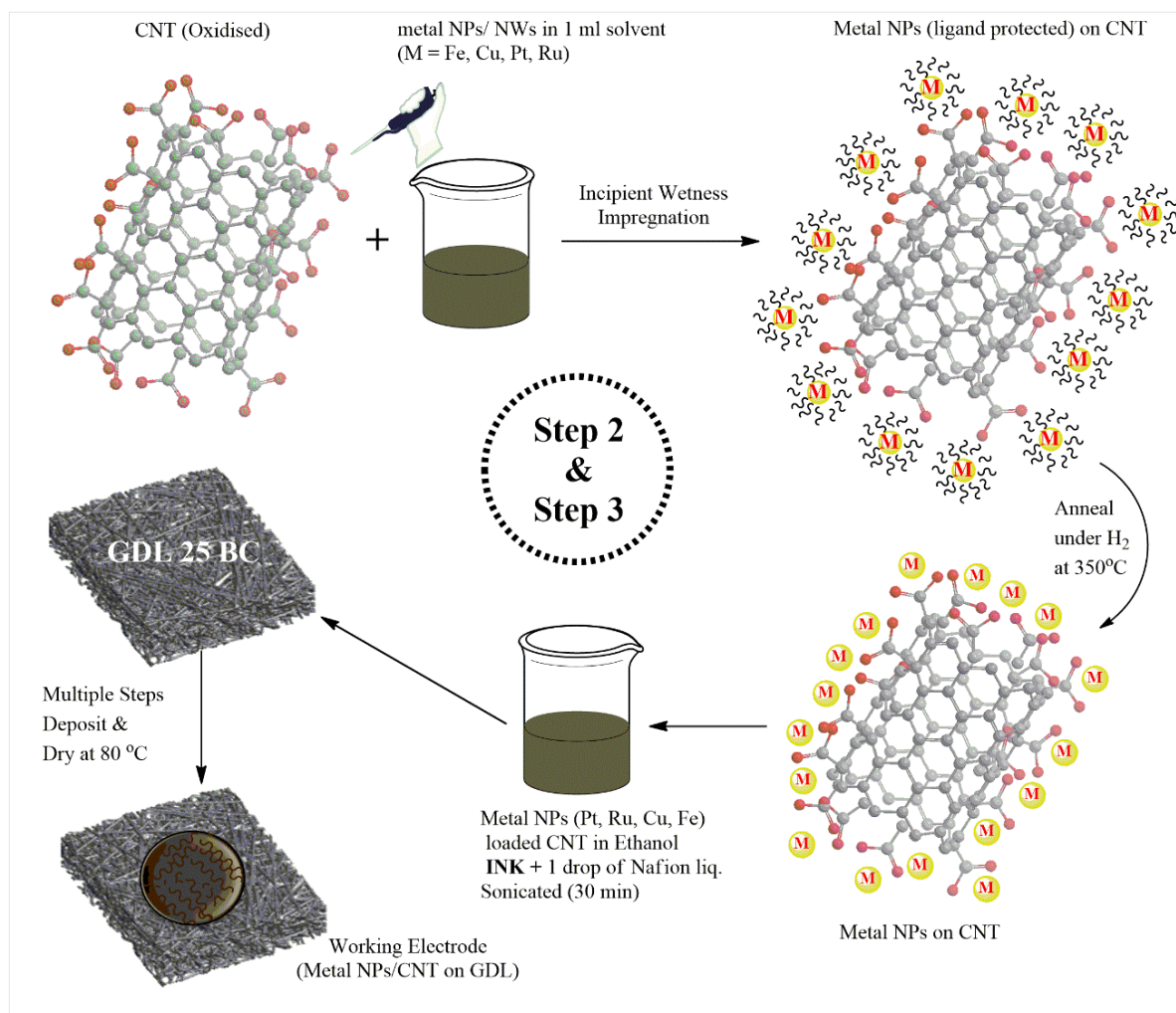


Fig. 3.2 A Schematic showing transfer of metal NPs onto the CNTs from NPs/NWs in solvent and coating metal NP doped CNT based INK on GDL to make the working electrode.

Step 3: Deposition of metal NPs loaded CNTs onto GDL

Finally to prepare the electrode, 35 mg of this metal doped CNTs were mixed with 3.5 ml of ethanol and a drop of Nafion perfluorinated resin (acting as a binding agent) and then, sonicated for 30 minutes to get a dark black INK formulation. This INK was coated onto the GDL in several steps of depositing thin layers and drying, thereby creating the final working electrode.

3.2.2. Basic conditions of the cell

Potentiostatic (-2V), 0.5 M KHCO₃, 10 ml/min CO₂ (100 %) flow, runtime 4 hours 30 minutes (in some cases 20 hours). Liquid samples collection at 1 hr, 4hr, and final time. Gas samples were analysed at 15 min, 30 min, 45 min, 60 min, 90 min and 4 hours. In some specific cases, galvanostatic conditions (5 mA and 10 mA), and Potentiostatic (-0.5V, -1V, -1.4V, -1.5V, -1.6V, -2V) were also used.

3.3 Results and Discussions

3.3.1. Design and engineering of the liquid phase electro-catalytic Cell:

3.3.1.1. Modelling and working principles

A novel electro-catalytic cell working in liquid phase was developed and realized at the laboratory CASPE/INSTM of the University of Messina. The cell is based on a three-electrode configuration *annex*³ and takes advantage of PEM fuel cell technology in terms of materials and working principle. The design of the cell was optimized for its compactness, electrode positioning, and uniform gas flow & supply. Moreover, all the engineering details were taken into account, i.e. the fitting of the electrodes, the effectiveness of the contact points on the working electrode and tightness of the two compartments. This new cell design has some similarities with respect to the gas phase device, which was fully described in *Chapter 2*:

- A proton selective membrane was used to separate the zone where the protons and O₂ form by water electrolysis (the anode), from the zone where CO₂ is reduced (the cathode). The membrane allows the migration of protons from the anode to the cathode side.
- The CO₂ continuously flows to the cathode of the electrocatalytic cell as 100% CO₂ at a rate of 10-20 ml/min;
- The negative currents/potentials applied are similar (1-2 V; 10-100 mA).
- The solvent used in the reaction 0.5 M KHCO₃, with a pH ranging in 8-8.5 (in the gas-phase cell this solvent is only on the anodic compartment).
- The design of the electrocatalytic electrode is similar: metal nanoparticles were deposited over a functionalized carbon black - CB /carbon nanotube - CNT and then supported over a conductive net (carbon paper), while the external side of the carbon support (the side coated with Teflon) was at contact with the gas or liquid phase to realize a gas diffusion electrode (GDE) *Fig. 3.3* as in PEM fuel cells.

Theoretically, these electrocatalytic cells can be considered as the CO₂ reduction hemi-cells of a complete PEC solar cell, where both photo-catalytic and electro-catalytic parts are present. In the photo-catalytic part, a photo-anode modelled with a photo-active material that is able to absorb sunlight to create a charge-separation, with the holes utilized at suitable catalytic centers for the reaction of water oxidation to produce O₂ and protons, the latter being transported to the electro-catalyst through the membrane. The electrons are instead collected and transported externally (through a wire) to the conductive electro-catalyst of the cathodic part of the PEC cell, where CO₂ is reduced to various fuels.

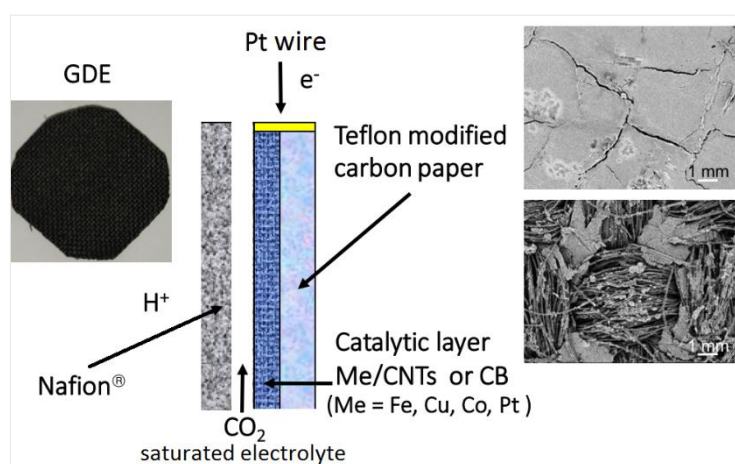


Fig. 3.3 Schematic illustration of the GDE-type electrodes utilized for the CO₂ electrochemical reduction. Image on the left shows the full gas-diffusion electrode (GDE), while images on the right are scanning electron microscopy images of the side at contact with the membrane and of the side at contact with gas phase (CO₂) or the electrolyte in which CO₂ is bubbled.

The liquid phase cell prototype was designed in Plexiglas (to allow visual inspection) and works on a three-electrode configuration, as it is graphically represented in *Fig. 3.4*. The cathode side houses the working electrode (5.7 cm², diameter 2.7 cm) placed at a small distance (0.5 cm) from the reference electrode (Ag/AgCl). A Pt wire makes up for the electric contact and closing of the external circuit between the working electrode and the counter electrode. A commercial Pt ball-edged rod (Amel) acts as the counter electrode, in the anodic compartment of the cell. A constant voltage bias (usually -2 V) is applied to the electrodes using a potentiostat-galvanostat (Amel mod. 2049A).

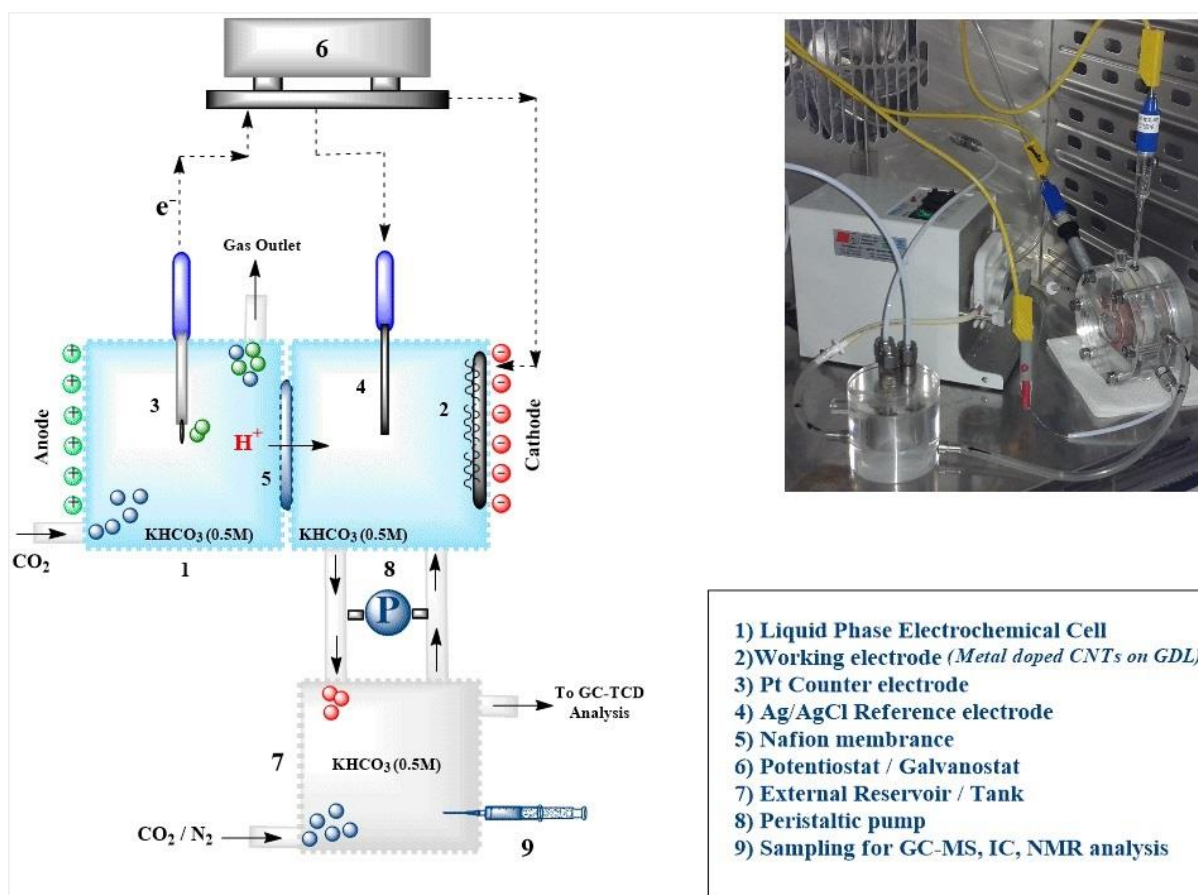


Fig. 3.4 Graphical representation of the experimental setup for liquid phase cell for CO₂ reduction to fuels.

The electro-catalytic cell is divided into two compartments: 1) anodic and 2) cathodic with the proton-exchange membrane (Nafion[®] 117) acting as the partition. A 0.5 M aqueous KHCO₃ electrolytic solution is used to perform the reactions. The volume of the electrolyte solution in the anodic compartment is 7 ml. An external reservoir containing the electrolytic solution is saturated with constant flow of pure gaseous CO₂ (10 ml/min). This CO₂ saturated electrolytic solution is flowed to the cathodic compartment using a peristaltic pump. The net volume of the solution (cathode + external tank + tubes) is 25 ml and the net volume in the cathodic compartment is 7 ml, the same as in the anode. CO₂ gas is also flowed into the anodic compartment in order to push the O₂ out (produced during the HER reaction), which otherwise could create accumulation of the O₂ bubbles around the counter electrode and thereby, leading to increase in the resistance of the solution and decrease in the overall productivity. Moreover, the presence of CO₂ and KHCO₃ in each compartment allows to buffer the electrolyte solution at a pH = 8 - 8.5.

The liquid samples were taken from the electrolytic solution in the external tank. The analysis of the composition of the solution was performed by using ^1H Nuclear Magnetic Resonance Spectroscopy (NMR), Gas Chromatography-Mass Spectrometer (GC-MS) and Ion Chromatography (IC). The gas samples were collected at regular intervals by sampling the gaseous stream leaving the external tank and analysed by Gas-chromatography (GC- TCD).

3.3.1.2. Design Challenges:

- In the initial stages of the development of the cell, one of the major problems encountered was to fix the working electrode position and depth as it is the main reason for leakage problems. This was solved by using a proper o-ring in the cathode, as well as by adopting a removable Plexiglas support to adjust the depth of different working electrodes.
- Unlike electrolyte-less cell, it was necessary to have a continuous flow of CO_2 saturated electrolyte. This was solved by adding an external reservoir tank, which also allowed to take many samples without having significant changes in reaction conditions (decrease of volume). Moreover, the presence of an external tank allowed to avoid a direct flow of CO_2 striking on the cathodic surface, which can negatively interfere with the reduction process. The decrease of the volume (due to the liquid samples for analysis) must be taken into account in the calculation of product concentrations.
- A simple but important problem that needed to be addressed was the O_2 bubble formation in the anodic compartment, due to water oxidation by water splitting reaction. These bubbles can accumulate in the anode and settle on the platinum counter electrode surface increasing the resistance in the system. This was solved to a good extent by flowing CO_2 (or any other inert gas) into the anodic compartment.
- The liquid phase cell designed here, has a runtime of about 20-24 hours before the electrolytic solution in the anodic compartment losses contact with the counter electrode. So, to solve this problem and to have longer reaction times, another external tank with the electrolytic solution continuously flowing was added.

3.3.2. Characterization:

The catalysts were characterized using different techniques to determine the physical and structural properties. The characterizations include AAS, BET, HRTEM, XPS, XRD and current profiles.

3.3.2.1. Structural Analysis

X-Ray Diffraction (XRD) was performed to determine the crystal structure of the catalysts.

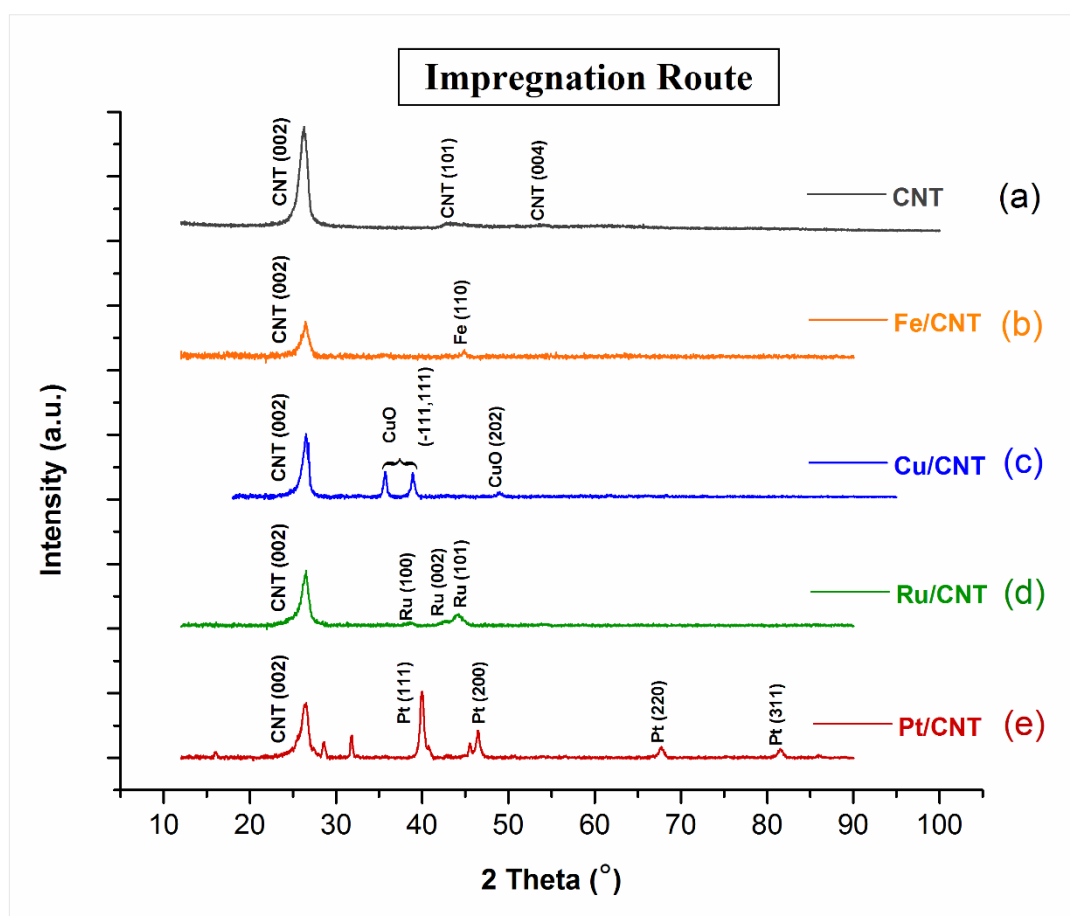


Fig. 3.5 XRD patterns (Impregnation route, 10 wt. % of metal) for (a) bare CNTs, (b) Fe-CNT, (c) Cu-CNT, (d) Ru-CNT, (e) Pt-CNT.

Fig. 3.5 shows the XRD patterns for (a) bare-CNTs, (b) Fe-CNT, (c) Cu-CNT, (d) Ru-CNT and (e) Pt-CNT synthesized via impregnation route. In the diffraction pattern of *Fig. 3.5* (a), the dominant peak at $2\theta = 26.45^\circ$ and minor peaks at $2\theta = 43.30^\circ$ and 54.13° were observed, which correspond to the planes (002), (101), (004) of the CNTs (graphitic), respectively. In the *Fig. 3.5* (b), a small peak was found at $2\theta = 44.93^\circ$, corresponding to the plane (110) of the Fe metal (BCC). In the *Fig. 3.5* (c), two twin peaks were observed at $2\theta = 35.67^\circ$ and 38.90° ,

corresponding to the planes (020) and (111), respectively and a weak peak at $2\theta = 48.97^\circ$, corresponding to the plane (202), of Cu oxide (monoclinic). In the *Fig. 3.5 (d)*, a peak was found at $2\theta = 44.27^\circ$, corresponding to the plane (101) of the Ru metal (HCP). Moreover, two weak peaks were observed at $2\theta = 38.59^\circ$ and 42.77° , which correspond to planes (100) and (002) of Ru metal. In the *Fig. 3.5 (e)*, two main peaks were observed at $2\theta = 39.97^\circ$ and 46.53° , corresponding to the planes (111) and (200) of the Pt metal (FCC), respectively. Moreover, two weak peaks were observed at $2\theta = 67.72^\circ$ and 81.53° , which correspond to planes (220) and (311) of Pt metal. The peak at $2\theta = 26.50^\circ$ was found to be present in all the nanoparticle sample patterns, which corresponds to the (002) plane of the CNTs.

3.3.2.2. TEM Morphological Measurements

High Resolution Transmission Electron Microscopy (HRTEM) was used to understand the structural and morphological characteristics of the catalysts. *Table 3.3* provides detailed size distributions of the metal NPs on CNT in terms of mean, standard deviation and range values.

Table 3.3 Detailed size distributions of Pt, Fe, Cu, Ru and Co NPs via Impregnation routes.

Electro-catalyst (<i>Impregnation Route</i>)	Particle Size (nm)		
	<i>Mean</i>	<i>Standard Deviation</i>	<i>Min. – Max.</i>
<i>Co-CNT_{ox}</i>	6.6	1.6	2.8 – 13.0
<i>Pt-CNT_{ox}</i>	7.8	3.8	2.2 – 32.0
<i>Fe-CNT_{ox}</i>	9.3	3.1	3.2 – 25.4
<i>Cu-CNT_{ox}</i>	10.4	4.4	3.6 – 39.0
<i>Ru-CNT_{ox}</i>	2.6	1.2	1.5 – 12.5

Fig. 3.6 (a), (b), (c), (d) and (e) show the micrographs for Pt, Fe, Cu, Ru and Co NPs obtained via the impregnation route, respectively. A non-uniform distribution and large particle size can be noticed clearly. The NPs size varies in a large range from 1.5 nm to 39 nm. Although the metal NPs are both inside and outside the CNTs, the larger NPs are mainly deposited inside the CNTs. This can be explained from the synthesis route (wetness impregnation, i.e. solvent with NPs being absorbed into the pore volume), which increases the probability of agglomeration inside rather than on the surface.

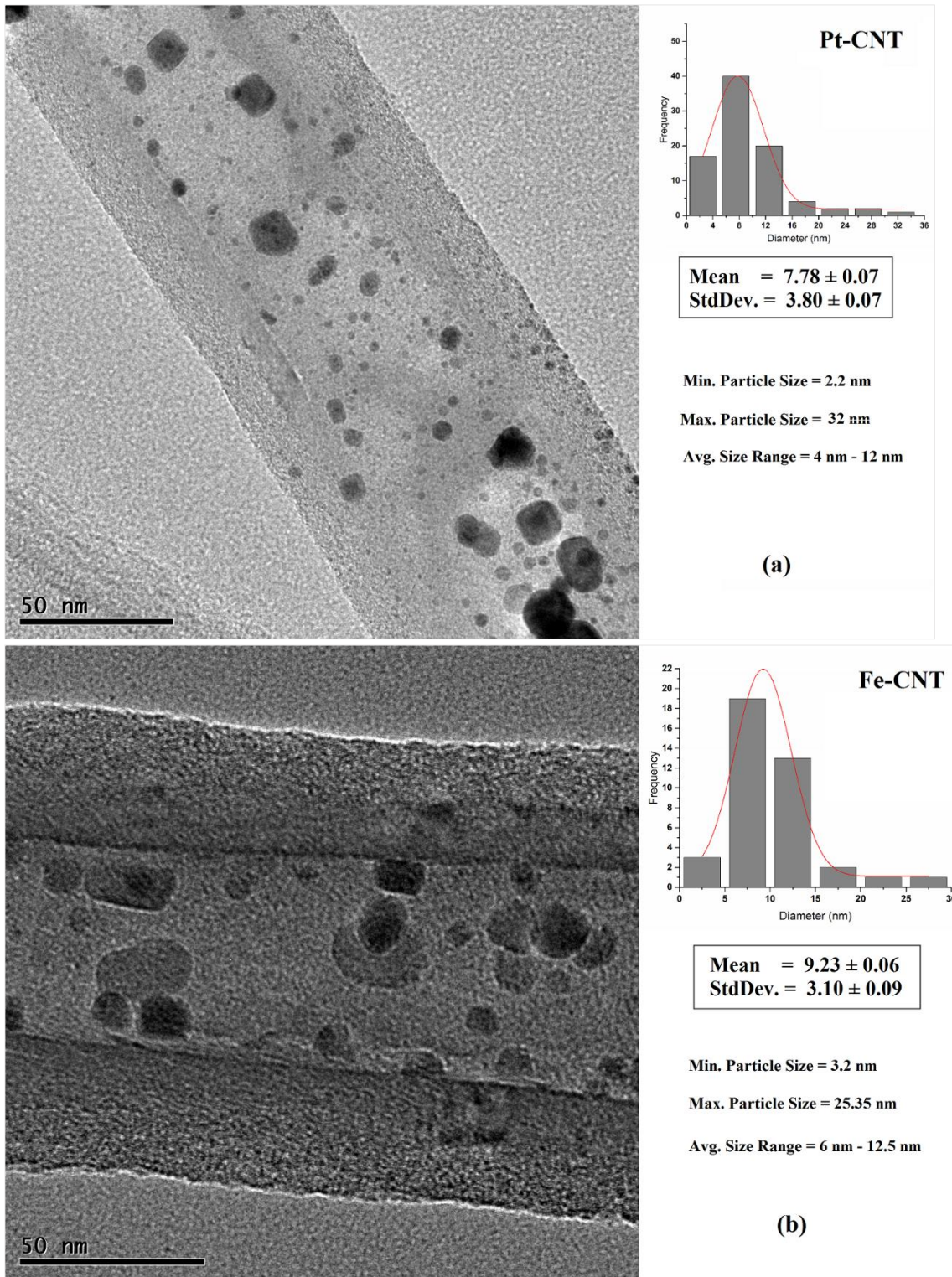


Fig. 3.6 TEM image showing (a) Pt NPs on CNT, (b) Fe NPs on CNT via Impregnation Route

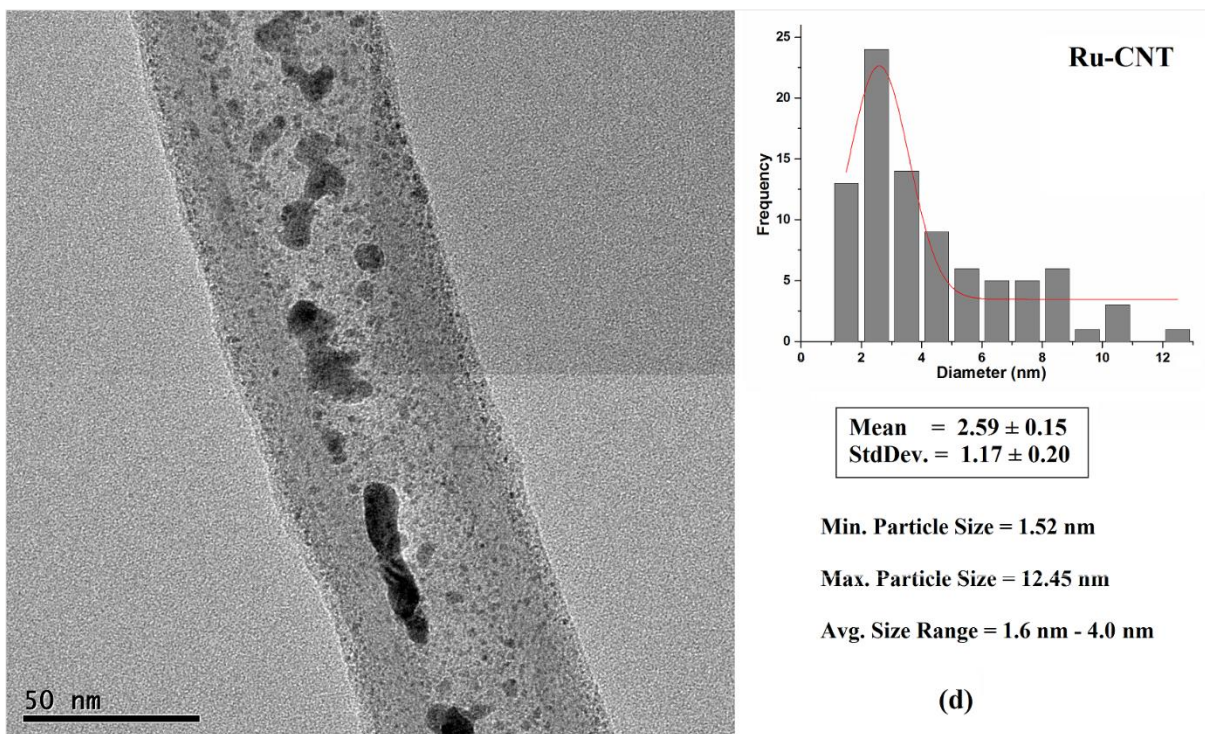
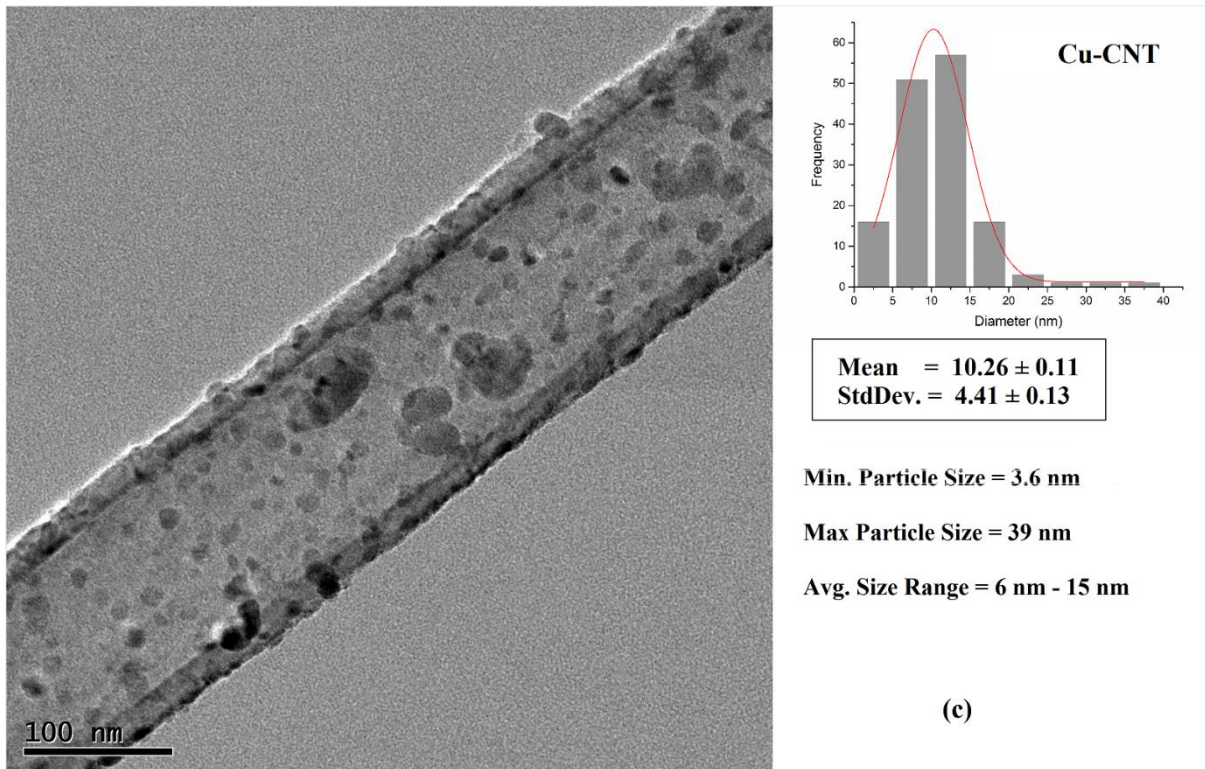


Fig. 3.6 TEM image showing (c) Cu NPs on CNT, (d) Ru NPs on CNT via Impregnation Route

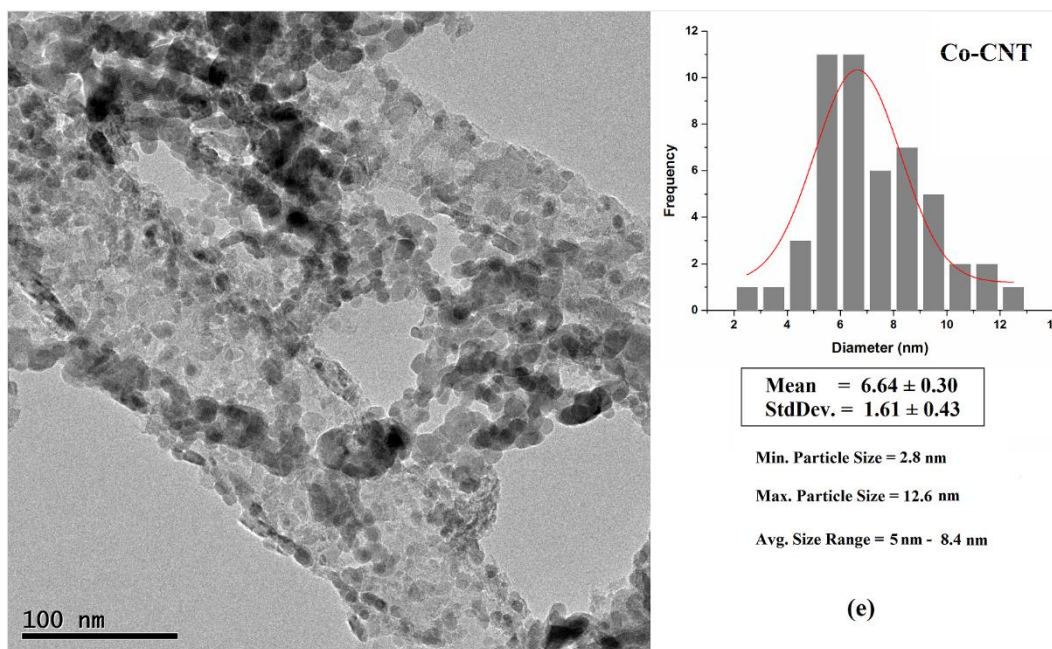


Fig. 3.6 TEM image showing (e) Co NPs on CNT via Impregnation Route

3.3.2.3. Surface Analysis

A quantitative surface analysis was performed by X-Ray photoelectron spectra (XPS). The survey gives an insight into the oxidation state of the metal NPs and the different oxygen functionalities present on the CNTs. The curve was corrected with the C-1s binding energy of adventitious carbon (284.9 eV) as the reference before collecting the data.

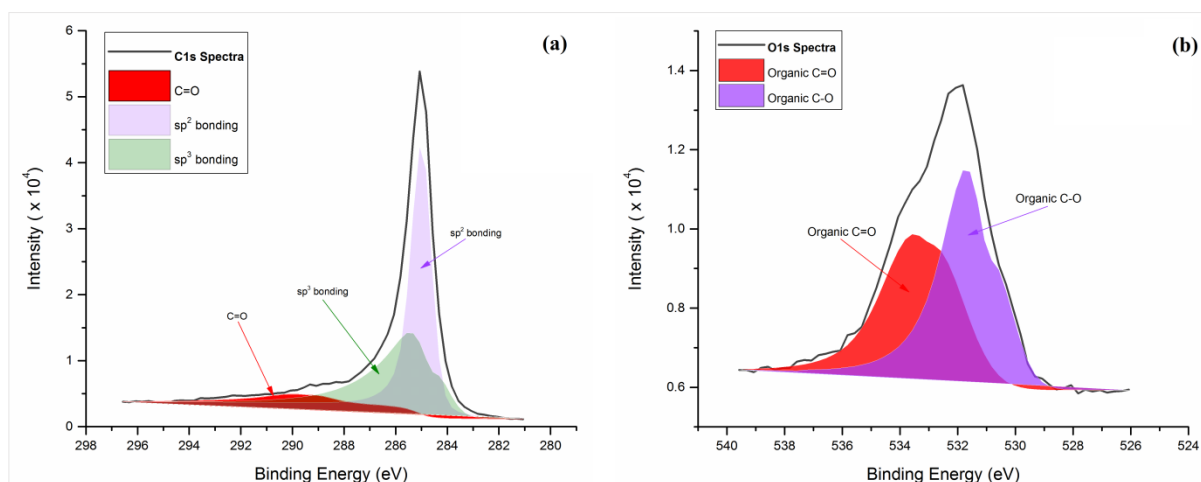


Fig. 3.7 XPS data for bare CNT_{ox} - (a) illustration of the C1s and respective deconvolution spectra, (b) XPS data illustration of the O1s and respective deconvolution spectra.

Fig. 3.7 (a) explains the type of carbon bonding present and also, the oxygen functionality left after NP loading. The two peaks found at 284 eV and 284.8 eV are the characteristic binding energies for the C=C and C-C species, and the peak at 289 eV corresponds to C=O. These give an insight into the graphitic nature of the Carbon. *Fig. 3.7 (b)* Illustrates the possible oxygen-carbon bonding on the CNT_{ox} surface, showing two different types of oxygen functionalities (C-O and C=O).

3.3.2.4. Quantitative and physical characterizations

The amount of metal loading on the CNT substrate in the catalyst was determined by Atomic Absorption Spectroscopy (AAS). The weight % of metal NPs on the CNT substrate prepared via different synthesis routes are furnished in the *Table 3.4*. The % metal loading on the CNTs for the impregnation Route were found to be in the range **9-10 %**.

The Brunauer-Emmett-Teller (BET) surface area and porosity of the catalytic material were analysed by N₂ adsorption/desorption.

Table 3.4 AAS and BET characteristics of Pt, Fe, Cu, and Ru NPs via Impregnation route.

Electro-catalyst	AAS (% wt. metal w.r.t. CNTs)	BET		
		$a_{BET} (m^2 \cdot g^{-1})$	$V_m (cm^3 \cdot g^{-1})$	Avg. pore diameter (nm)
<i>CNT_{ox}</i>	–	23.1	5.3	11.4
<i>Co-CNT_{ox}</i>	9.7	72.6	16.7	14.9
<i>Pt-CNT_{ox}</i>	9.3	23.6	5.4	11.3
<i>Fe-CNT_{ox}</i>	8.8	63.8	14.6	9.2
<i>Cu-CNT_{ox}</i>	9.5	48.3	11.1	10.8
<i>Ru-CNT_{ox}</i>	9.0	47.2	10.8	19.1

The BET characteristics are presented in the *Table 3.4* above. An increase in the surface area and pore volume with respect to the CNT_{ox} can be clearly noticed. No significant change in average pore diameter can be explained as the reduced sticking between the CNTs, due to the modified surface properties of functionalized CNTs during the metal NPs addition, except for Co, Ru -CNT_{ox}. These values attribute to the increased catalytic active area and increased fuel productivity, in tune with the results. *Fig. 3.8* shows, the N₂ adsorption-desorption isotherms for the bare CNT and Cu doped CNTs via Impregnation route. For other metal NPs (Pt, Fe, Ru, Co) the graph is shown in *Fig. 3.11*, in the *annex³*.

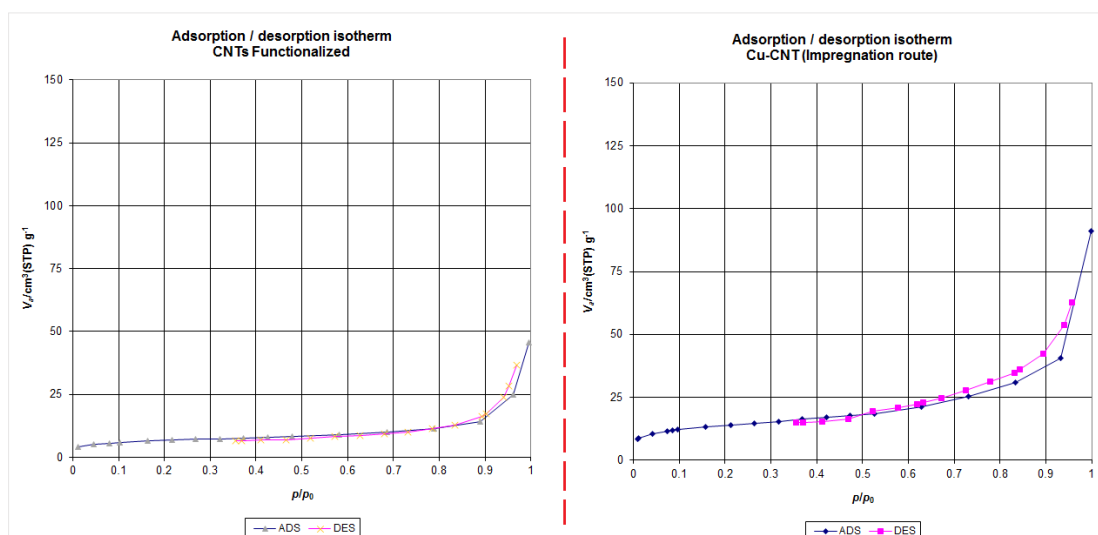


Fig. 3.8 N₂ adsorption/desorption isotherms for bare CNT_{ox} and Cu-CNT_{ox}.

3.3.2.5. Current Profile

The current profiles (in milli-amperes) for the CO₂ reduction reactions, for the different metal (Cu, Fe, Pt and Ru) doped CNT based electrodes formed via impregnation route are shown below in *Fig. 3.9*. A constant potential of -2.0 V is applied to the cell. It can be observed that the currents at the beginning of the reaction is quite high and then stabilize as an equilibrium pH is achieved in the electrolytes in the anodic and cathodic compartments. Although, the initial currents vary from 0.2 to 0.5 A, the equilibrium current lies in the range of 3 to 7 mA.

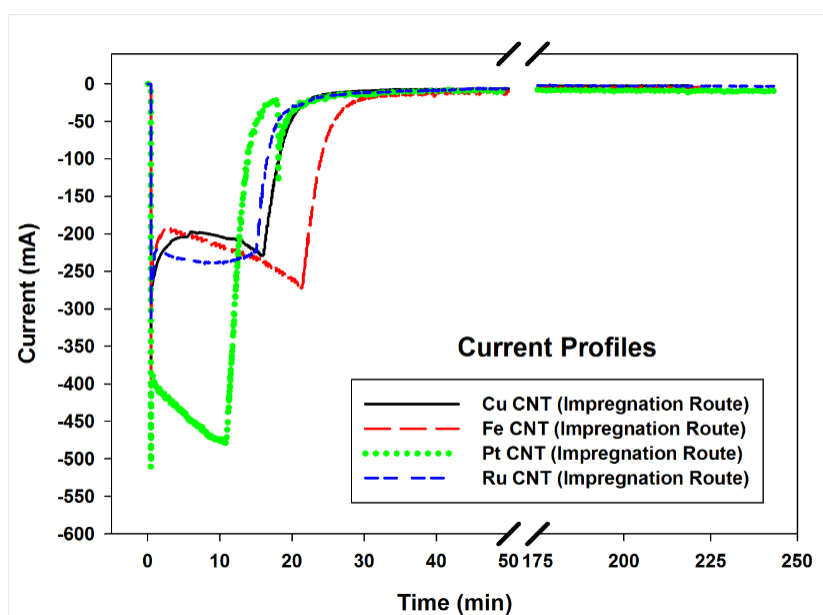


Fig. 3.9 Current profiles for Cu, Fe, Pt, and Ru loaded CNTs via Impregnation Route.

3.3.3. Electro-catalytic CO₂ reduction

3.3.3.1. Fuel Productivity

The fuels produced during the electrochemical reduction of CO₂ were analysed using various techniques, which include IC, GC-Mass, ¹H NMR, and GC-TCD as discussed above in the EC cell section. The major liquid products detected in the liquid electrolyte on the cathode side were formic acid, acetic acid, methyl formate, methanol and traces of acetone, isopropanol. The gaseous product was found to be H₂, although minor quantities of CH₄ and CO were expected but not found (under the detection limit). *Table 3.5* provides the quantitative productivity values (in micromoles per unit time - hour) of the various products formed for the Carbon black/ CNT based electro-catalysts doped with different metal NPs synthesized via impregnation route and also, to have a reference for the values reported, results of CNT (oxidised) alone are also presented (i.e. without any metal NPs, CNT deposited on the GDL).

Table 3.5 Productivity values for the CO₂ EC reduction in liquid phase cell.

FUELS ($\mu\text{mol}\cdot\text{h}^{-1}$)	CATALYSTS								
	<i>Cu Foil</i>	<i>CNT_{ox}</i>	<i>Fe/CB</i>	<i>Cu/CB</i>	<i>Co/CB</i>	<i>Pt/CNT_{ox}</i>	<i>Fe/CNT_{ox}</i>	<i>Cu/CNT_{ox}</i>	<i>Ru/CNT_{ox}</i>
<i>Formic Acid</i>	10.809	0.094	0.230	0.405	0.261	1.763	0.414	0.542	0.696
<i>Acetic Acid</i>	0.063	0.258	0.107	0.644	0.222	1.380	0.525	0.617	0.276
<i>Methyl Formate</i>	-	-	0.076	0.018	0.032	-	-	-	-
<i>Acetone</i>	0.006	-	-	-	-	-	0.006	0.005	-
<i>Methanol</i>	0.279	-	-	-	-	-	0.179	0.405	0.697
<i>Isopropanol</i>	0.008	-	-	-	-	-	0.003	-	-
<i>Ethanol</i>	0.016	-	-	-	-	-	-	-	0.009
<i>H₂</i>	202.42	6.099	2.800	2.300	1.173	97.232	32.263	35.357	63.640
<i>C-Products (NET)</i>	11.181	0.352	0.413	1.067	0.514	3.143	1.127	1.569	1.678

Note: CB – Carbon black ; CNT_{ox} – functionalized CNTs ; C-products – carbon products

The productivity and selectivity are quite different with similar catalysts in the gas phase reduction of CO₂ in comparison to the liquid phase reduction. The gas phase reduction fuels are reported in the *Table 3.6* in micromoles per time (hr-Hour).

Table 3.6 Productivity values for the CO₂ EC reduction in gas phase cell.

FUELS ($\mu\text{mol}\cdot\text{h}^{-1}$)	CATALYSTS				
	<i>Fe/CB</i>	<i>Pt/CNT_{ox}</i>	<i>Fe/CNT_{ox}</i>	<i>Cu/CNT_{ox}</i>	<i>Co/CNT_{ox}</i>
<i>Acetic Acid</i>	0.015	0.014	0.092	-	0.034
<i>Acetaldehyde</i>	0.029	0.017	0.067	0.011	0.045
<i>Acetone</i>	0.001	-	-	-	0.001
<i>Methanol</i>	0.110	0.010	0.140	0.048	0.120
<i>Isopropanol</i>	0.001	0.024	0.084	0.009	-
<i>Ethanol</i>	0.110	0.036	0.094	0.067	0.200
<i>CO</i>	36.0	35.0	65.0	9.6	32.0
<i>H₂</i>	320.0	450.0	360.0	170.0	200.0
<i>C-Products (NET)</i>	0.266	0.101	0.144	0.135	0.400

From the productivity values from the two tables above, it can be observed that the amount of liquid carbon products (C-products) is about 2 to 25 times higher for the liquid phase in comparison to the gas phase. But, in the gas phase there is a huge productivity shift towards the production of CO. However, a common aspect in both cells is the relevant formation of H₂. Hydrogen is an undesired product, because reduces the Faradaic efficiency to the products of CO₂ reduction. This indicates that in our experimental conditions the use of electrons/protons for the reduction of CO₂ is a slower process with respect their recombination to form H₂. Inhibiting the last reaction is thus a requirement to improve the performances in the electrocatalytic reduction of CO₂. On the other hand, these results also evidence that formation of H₂ is a facile reaction not specifically requiring dedicated catalysts.

There are main differences in the type of products of reaction between liquid- and gas-phase cell operations, e.g. presence or not of the bulk electrolyte. In the gas outlet stream leaving the cathodic part of the cell, together with H₂, CO and in small amount CH₄ are also detected in the case of gas phase operations. The two last products are not detected in liquid phase operations. Although CO may form from formic acid decomposition (see eq. 2a below) in liquid-phase operations, it immediately reacts and CO is not detected in the products stream leaving the cell, at least up to detection limit. On the contrary, CO is a main product of CO₂ electrocatalytic reduction in gas-phase cell operations, indicating a different mechanism of formation, with probably CO being the primary product of CO₂ reduction, rather than a

secondary product, as observed in liquid-phase operations. This may explain why methane, deriving from the catalytic reduction of CO on copper, iron and cobalt metal nanoparticles, is observed even if in small amounts in experiments with gas-phase cell, but not in those with liquid-phase cell.

The type of liquid products formed, detected in the electrolyte or condensed in the cold trap from the gaseous stream leaving the gas-phase cell, are also different in the two cases. *Table 3.6* summarize the behaviour of the different type of tested electrodes in gas-phase cell (EL conditions). As it can be observed, the different types of products in gas phase are:

- i) Methanol, rather than formic acid as C1 main product (together with CO);
- ii) Acetaldehyde, ethanol together with acetic acid as C2 products, while only the latter was observed together with methyl formate in some electrocatalysts;
- iii) Acetone and isopropanol as C3 products, while only acetone as C3 products were detected in liquid phase operations (isopropanol only in the case of Fe/CNT_{ox}).

This different type of products clearly suggests a different type of mechanism of CO₂ electro-catalytic conversion, in agreement with what commented before. *Table 3.7* summarizes the differences observed in the type of products of reduction of CO₂ between gas-phase and liquid-phase cell operations.

Table 3.7 Comparison of types of products obtained in liquid and gas phase operations in CO₂ electro-catalytic reduction.

Gas Phase	Liquid Phase
<i>Methanol</i>	
<i>Acetaldehyde</i>	Formic acid
<i>Acetic Acid</i>	Acetic acid
<i>Ethanol</i>	Methanol
<i>Acetone</i>	Methyl formate
<i>Isopropanol</i>	Acetone, Isopropanol (in traces)
<i>Hydrocarbons C4-C9 (in traces)</i>	

It may be evidenced that not only the productivity is different between gas-phase (*Table 3.6*) and liquid-phase (*Table 3.5*) operations, but also the relative order of activity. In gas-phase cell, the best productivity to C-products of CO₂ reduction is shown by Fe-CNT_{ox} (around 0.48 μmol/h). The same electrode in liquid phase operations, considering the total volume of

electrolyte, has a productivity of about 1.163 $\mu\text{mol/h}$, e.g more than twice as higher than that of gas phase. For Cu-CNT_{ox} catalyst, productivity in gas-phase operations is about 0.14 $\mu\text{mol/h}$, while in liquid-phase operations about 1.5 $\mu\text{mol/h}$. Thus again about one order of magnitude difference is observed. It is also important to note that we did not take into account the CO generation which is atleast 1-order magnitude higher for gas phase in comparison to liquid phase. The relative order of productivity for CO₂ reduction in gas-phase cell (*Table 3.6*):

Fe-CNT_{ox} > Co-CNT_{ox} > Fe-CB > Cu-CNT_{ox} > Pt-CNT_{ox}

while for liquid-phase cell (*Table 3.5*):

Pt-CNT_{ox} > Ru-CNT_{ox} \approx Cu-CNT_{ox} > Fe-CNT_{ox} > Co-CB > Fe-CB > CNT_{ox}

This observation further remarks that different aspects may determine the productivity in the reduction of CO₂, reasonably associated to a different reaction mechanism.

3.3.4. Mechanism

The clarification of above question requires a more in depth analysis of the reaction mechanisms, with operando techniques, which, however, are not simple to apply to electrochemical tests under relevant environmental conditions. We may thus advance only some initial considerations, which help in setting the scene for more detailed mechanistic studies.

As earlier reported in the paper ^[27], the CNT_{ox} has a catalytic ability to produce small amounts of products. The activity is governed by the oxygen functionalities generated by oxidative pre-treatment (discussed in experimental section) but the CNTs (un-oxidised) alone were relatively inactive and did not produce any significant amounts of products. It can be concluded that the leftover metal impurities from the CNT synthesis (by Chemical vapour deposition – relevant data in *Table 3.2*), do not have an effect on the electro-reduction of CO₂.

The proton transferred through the Nafion membrane along with the electrons flowing through the outer circuit leads to formation of H₂, as shown in the *Table 3.5*. The H⁺ generated, reduces the CO₂ present in the electrolytic solution leading to the formation of formic acid. The products formed can be explained as due to the presence of active electro-catalytic sites, i.e. oxygen functionalities on the CNT_{ox} likely chetonic or carboxylic groups as shown in the XPS data and also, as seen for other catalytic reactions ^[65].

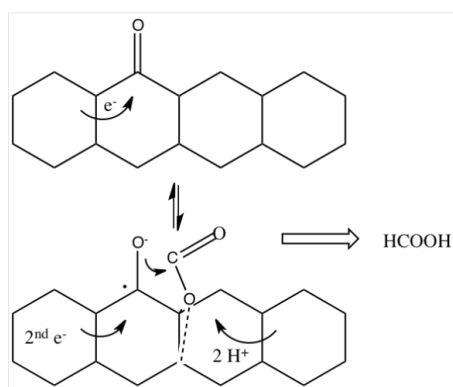


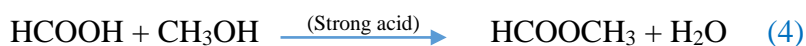
Fig. 3.10 Schematic of the reaction mechanism of CO₂ reduction to formic acid [27].

Chetonic or carboxylic groups present at the edges or defects of CNTs may act as trapping sites for electrons, forming resonance species. The localized electron on the carbon activates the adjoining C-C bond, making it possible to coordinate with the oxygen atom in CO₂, and also breaking the molecule from linearity as shown in *Fig. 3.10*. Similar activation mechanism was proposed for the N-doped CNTs active in oxygen reduction reaction (ORR) [65-67].



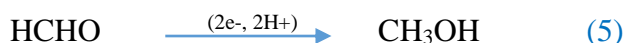
Formic acid and acetic acid formation are expected to follow the steps as outlined in the previous work [27]. Acetic acid (other major product as reported in *Table 3.5*) formation is a bit more complicated to explain. A plausible conception is that the formic acid further reduces, leading to the formation of formaldehyde which may selectively transform into acetic acid. It is reported that formaldehyde can selectively convert into acetic acid in relatively mild conditions (500 psi CO, 100°C) in the presence of a strong acid (HI) [68]. Formic acid under acidic conditions (as the conditions existing near the electrocatalyst surface and being close to the proton exchange membrane) decomposes to CO and H₂O. The thus formed carbon monoxide may react with the formaldehyde under acidic conditions to selectively produce acetic acid (a variation of Kock-Haaf reaction) [68]. It is expected that a similar mechanism occurs in our case during the electrochemical reduction of CO₂. This may also account for why further reduction of formaldehyde to methanol was not observed.

The presence of a metal nanoparticle leads to an increase in the productivity in the conversion of CO₂ and the presence of methanol or methyl formate in some cases (*Table 3.5*). The latter reasonably derives from the reaction of formic acid esterification with methanol under acid conditions:



Methyl formate may thus be associated with the formation of methanol and its fast conversion under the reaction conditions present in our experiments.

Various other observations can be made on the results evidenced in *Table 3.5*. Copper-based electrodes have been tested in three types of forms: as Cu foil (as reference, being one of the type of electrodes often utilized in the electrocatalytic reduction of CO₂), and in the form of copper nanoparticles supported over CNT_{ox} or CB. It may be observed that methyl formate is observed in the case of CB as support for Cu NPs, while for the Cu NPs on CNTs or Cu foil promotes the formation of methanol and minor quantities of other products. In terms of productivity, Cu-CNT_{ox}/GDL has slightly higher formation of net C-products than Cu-CB/GDL, although the copper amount and size of the copper nanoparticles is analogous but the surface area are different. The higher surface area of CB with respect to CNT_{ox} (*Table 3.4*) may thus be not the reason for the different behaviour, being dispersion of copper in the two supports relatively similar. We may also note in *Table 3.5* that formic and acetic acid formation are more or less similar in both Cu-CNT_{ox}/GDL and Cu-CB/GDL. Thus the main difference between the two samples is in the rate of the further reduction of formaldehyde to methanol:



Methanol then further reacts according to eq. (4). CB (Vulcan XC-72) contains about 0.3% S, present as sulphonic groups (-SO₃H) on the surface. These acid groups, stronger than the -COOH groups present on CNT_{ox} as a consequence of the oxidative pretreatment, reasonably favour a better surface transport of protons coming from the membrane. Probably the difference in the behaviour observed between CNT_{ox}/GDL and Cu-CB/GDL is associated with the different concentration of protons at the electrocatalytic centers, although this hypothesis should be better proofed. A higher proton concentration favours the further reduction up to methanol, reducing the rate of side reactions. In fact, *Table 3.5* shows that productivity shifts towards methanol for CNT_{ox}/GDL with respect to Cu-CB/GDL.

3.4 Conclusions

The comparison of the same electrodes for the electrocatalytic reduction of CO₂ in operations in the presence (liquid-phase) or absence (gas-phase) of a bulk electrolyte provided a series of interesting indications both on the limiting steps of the process and on the reaction mechanism.

It was demonstrated that under electrolyte-less (EL, i.e. gas phase) operations, the productivity in the reduction of CO₂ is about 2 to 25 times lower in comparison to liquid phase, and different type of products were formed. This is related to differences in the reaction mechanism, which were discussed, although further studies are needed to clarify better the reaction mechanism and the influence of the presence of the electrolyte. Iron based catalyst showed promising results much better than Cu, Co, and Pt.

In liquid-phase operations it is suggested that the mechanism involves the step reduction via intermediate formation of formic acid and formaldehyde and finally methanol, although the latter step was observed only in some electrodes. In fact, due to the strong acid conditions present at the electro-catalyst, located at the interface with Nafion membrane, formic acid decomposes to generate CO, which reacts with formaldehyde to form acetic acid. Methanol also reacts further in these strong acid conditions to form methyl formate. Moreover, Cu and Ru based catalyst showed promising results much better than Co, Fe and good selectivity towards methanol production.

In gas-phase operations, this mechanism is no longer effective and the conversion of CO₂ involves its dissociation to CO, which remains strongly chemisorbed, giving rise to further transformation reactions and formation of C-C bonds that produce a different spectrum of products of that observed in liquid-phase operations.

The electrocatalysts utilized here are based on metal nanoparticles (Fe, Cu, Co, Pt, Ru) deposited on two types of conductive carbon supports: carbon nanotubes functionalized by oxidation treatment (CNT_{ox}) and Vulcan XC-72 carbon black (CB). CNT_{ox} without metal particles is active both in producing H₂ from protons/electrons and in the reduction of CO₂. The possible mechanism and the role of carbonyl groups, formed during the oxidative treatment, was discussed. It was commented why in general also when metal nanoparticles are present, the carbon does not act only as support or to transport charges, but has also an active role in the reaction mechanism. It is suggested that the active sites for the electrocatalytic reduction of CO₂ are located at the perimetral edge between metal nanoparticles and the carbon.

The nature of the latter, in particular the type of surface functional groups, determine thus considerably the performances, as experimentally observed.

As commented, these results are the start, not the end of the analysis of the mechanism of reaction in the type of electrodes investigated here. However, we believe that these results evidence how a more complex surface chemistry than typically supposed in literature is present in the electro-catalytic reduction of CO₂ on the type of electrodes we investigated. It should be commented that their performances are better than that of various other electrodes reported in literature for the conversion of CO₂, even if the different reaction conditions and way to report the data do not often allow a precise comparison.

There is thus, the need of a better understanding of the performances and reaction mechanism of these electro-catalysts (based on metal nanoparticles on conductive, functionalized carbon support) for the reduction of CO₂. They may open new possibilities in controlling the type of products formed and their productivity in this challenging reaction.

3.5 References

- [1] G.A. Ozin, *Adv. Mat.*, 2015, **27**, 1957.
- [2] G. Centi, S. Perathoner, in *Green Carbon Dioxide*, G. Centi, S. Perathoner, Eds., Wiley & Sons, 2014, **1**.
- [3] M.D. Kaerkaes, O. Verho, E.V. Johnston, B. Aakermark, *Chem. Rev.*, 2014, **114**, 11863.
- [4] S. Protti, A. Albin, N. Serpone, *Phys. Chem. Chem. Phys.*, 2014, **16**, 19790.
- [5] C. van der Giesen, R. Kleijn, G.J. Kramer, *Env. Science & Techn.*, 2014, **48**, 7111.
- [6] J.M. Thomas, *Energy & Env. Science*, 2014, **7**, 19.
- [7] S. Bensaid, G. Centi, E. Garrone, S. Perathoner, G. Saracco, *ChemSusChem*, 2012, **5**, 50.
- [8] G. Centi, S. Perathoner, *Greenhouse Gases: Science and Techn.*, 2011, **1**, 21.
- [9] G. Centi, S. Perathoner, *ChemSusChem*, 2010, **3**, 195.
- [10] D.G. Nocera, *Acc. Chem. Res.*, 2012, **45**, 767.
- [11] G. Centi, S. Perathoner, Artificial leaves, in *Kirk-Othmer Encyclopedia of Chemical Technology*, 2014.
- [12] C. Ampelli, S. Perathoner, G. Centi, *Phil. Trans. Royal Soc., A: Math., Phys. & Eng. Sciences*, 2015, **373**, 1.
- [13] P. Lanzafame, G. Centi, S. Perathoner, *Chem. Soc. Rev.*, 2014, **43**, 7562.
- [14] S. Perathoner, G. Centi, *ChemSusChem*, 2014, **7**, 1274.
- [15] G. Centi, E.A. Quadrelli, S. Perathoner, *Energy & Envi. Science*, 2013, **6**, 1711.
- [16] S. Perathoner, G. Centi, *J. Chinese Chem. Soc.*, 2014, **61**, 719.
- [17] J. Albo, M. A. Guerra, P. Castano, A. Irabien, *Green Chem.*, 2015, **17**, 2304.
- [18] P. Kang, Z. Chen, M. Brookhart, T.J. Meyer, *Top. Catal.*, 2015, **58**, 30.
- [19] Q. Lu, J. Rosen, F. Jiao, *ChemCatChem*, 2015, **7**, 38.
- [20] E.S. Rountree, B.D. McCarthy, T.T. Eisenhart, J.L. Dempsey, *Inorg. Chem.*, 2014, **53**, 9983.
- [21] J. Qiao, Y. Liu, F. Hong, J. Zhang, *Chem. Soc. Rev.*, 2014, **43**, 631.
- [22] E.V. Kondratenko, G. Mul, J. Baltrusaitis, G.O. Larrazabal, J. Perez-Ramirez, *Energy & Env. Science*, 2013, **6**, 3112.
- [23] C. Genovese, C. Ampelli, S. Perathoner, G. Centi, *J. Energy Chem.*, 2013, **22**, 202.
- [24] A. A. Peterson, and J. K. Norskov, Activity Descriptors for CO₂ Electroreduction to Methane on Transition-Metal Catalysts, *J. Phys. Chem. Lett.*, 2012, **3**, 251-258.

- [25] J. Hussain, E. Skúlason, and H. Jónsson, *Procedia Comput. Sci*, Computational study of electrochemical CO₂ reduction at transition metal electrodes, 2015, **51**, 1865-1871.
- [26] D. Gao, H. Zhou, J. Wang, S. Miao, F. Yang, G. Wang, J. Wang, and X. Bao, Size-Dependent Electrocatalytic Reduction of CO₂ over Pd Nanoparticles, *J. Am. Chem. Soc.*, 2015, **137**, 4288–4291.
- [27] C. Ampelli, C. Genovese, B.C. Marepally, G. Papanikolaou, S. Perathoner and G. Centi, Electrocatalytic conversion of CO₂ to produce solar fuels in electrolyte or electrolyte-less configurations of PEC cells, *Faraday Discuss.*, 2015, **183**, 125-145.
- [28] R. Reske, H. Mistry, F. Behafarid, B. R. Cuenya, and P. Strasser, Particle Size Effects in the Catalytic Electroreduction of CO₂ on Cu Nanoparticles, *J. Am. Chem. Soc.*, 2014, **136**, 6978–6986.
- [29] H. Mistry, R. Reske, Z. Zeng, Z. J. Zhao, J. Greeley, P. Strasser, and B. R. Cuenya, Exceptional Size-Dependent Activity Enhancement in the Electroreduction of CO₂ over Au Nanoparticles, *J. Am. Chem. Soc.*, 2014, **136**, 16473–16476.
- [30] K. J. P. Schouten, Z. Qin, E. P. Gallent, and M. T. M. Koper, Two Pathways for the Formation of Ethylene in CO Reduction on Single-Crystal Copper Electrodes. *J. Am. Chem. Soc.*, 2012, **134**, 9864–9867.
- [31] D. Raciti, K. J. Livi, and C. Wang, Highly Dense Cu Nanowires for Low-Overpotential CO₂ Reduction, *Nano Lett.*, 2015, **15**, 6829–6835.
- [32] J. Christophe, T. Doneux, and C. Buess-Herman, Electroreduction of Carbon Dioxide on Copper-Based Electrodes: Activity of Copper Single Crystals and Copper–Gold Alloys, *Electrocatal.*, 2012, **3**, 139-146.
- [33] Y. Hori, R. Takahashi, Y. Yoshinami, and A. Murata, Electrochemical Reduction of CO at a Copper Electrode, *J. Phys. Chem. B*, 1997, **101**, 7075–7081.
- [34] C. W. Li, and M. W. Kanan, CO₂ Reduction at Low Overpotential on Cu Electrodes Resulting from the Reduction of Thick Cu₂O Films, *J. Am. Chem. Soc.*, 2012, **134**, 7231.
- [35] A. A. Peterson, F. Abild-Pedersen, F. Studt, J. Rossmeisl, and J. K. Nørskov, How copper catalyzes the electroreduction of carbon dioxide into hydrocarbon Fuels, *Energy Environ. Sci.*, 2010, **3**, 1311-1315.
- [36] Z. Weng, J. Jiang, Y. Wu, Z. Wu, X. Guo, K. L. Materna, W Liu, V. S. Batista, G. W. Brudvig, and H. Wang, “Electrochemical CO₂ Reduction to Hydrocarbons on a Heterogeneous Molecular Cu Catalyst in Aqueous Solution”, *J. Am. Chem. Soc.*, 2016, **138**, 8076–8079.

- [37] Q. Lu and F. Jiao, “Electrochemical CO₂ reduction: Electrocatalyst, reaction mechanism, and process engineering”, *Nano Energy*, 2016 (in press)
- [38] W. I. A. Sadat and L. A. Archer, *Sci. Adv.*, 2016; **2**: e1600968.
- [39] R. Kas, R. Kortlever, A. Milbrat, M. T. M. Koper, G. Mul and Jonas Baltrusaitis, *Phys. Chem. Chem. Phys.*, 2014, **16**, 12194.
- [40] J. Shen, R. Kortlever, R. Kas, Y. Y. Birdja, O. D. Morales, Y. Kwon, I. L. Yanez, K. J. P. Schouten, G. Mul and M. T. M. Koper, *Nat. Commun.*, 2015, **6**, 8177.
- [41] R. Kas, R. Kortlever, H. Yilmaz, M. T. M. Koper and G. Mul, *ChemElectroChem*, 2015, **2**, 354–358.
- [42] R. Kortlever, J. Shen, K. J. P. Schouten, F. C. Vallejo, and M. T. M. Koper, *J. Phys. Chem. Lett.*, 2015, **6**, 4073–4082.
- [43] R. J. Lim, M. Xie, M. A. Sk, J. M. Lee, A. Fisher, X. Wang, K. H. Lim, *Catalysis Today*, 2014, **233**, 169–180.
- [44] A. Goepfert, M. Czaun, J. P. Jones, G. K. S. Prakash and G. A. Olah, *Chem. Soc. Rev.*, 2014, **43**, 7995.
- [45] S. Shironita, K. Karasuda, K. Sato, M. Umeda, *J. Power Sources*, 2013, **240**, 404–410.
- [46] J. Qu, X. Zhang, Y. Wang and C. Xie, *Electrochim. Acta*, 2005, **50**, 3576–3580.
- [47] C. Delacourt and J. Newman, *J. Electrochem. Soc.*, 2010, **157**, B1911–B1926.
- [48] Y. Hori, H. Ito, K. Okano, K. Nagasu, S. Sato, *Electrochim. Acta*, 2003, **48**, 2651–2657.
- [49] H. Li and C. Oloman, *J. Appl. Electrochem.*, 2007, **37**, 1107–1117.
- [50] G. Centi, S. Perathoner, *Catal. Today*, 2003, **77**, 287–297.
- [51] G. Centi, S. Perathoner, G. Wine, M. Gangeri, *Green Chem.*, 2007, **7**, 671.
- [52] C. Ampelli, G. Centi, R. Passalacqua, S. Perathoner, *Energy & Env. Sci.*, 2010, **3**, 292.
- [53] C. Ampelli, C. Genovese, R. Passalacqua, S. Perathoner, G. Centi, *Theor. Found. Chem. Eng.*, 2012, **46**, 651–657.
- [54] C. Genovese, C. Ampelli, S. Perathoner, G. Centi, *J. Catal.*, 2013, **308**, 237.
- [55] C. Ampelli, S. Perathoner, G. Centi, *Chinese J. Catal.*, 2014, **35**, 783.
- [56] C. Ampelli, C. Genovese, M. Errahali, G. Gatti, L. Marchese, S. Perathoner, G. Centi *Chem. Eng. Trans.*, 2015, **45**, 701–713.
- [57] C. Ampelli, G. Centi, R. Passalacqua, S. Perathoner, *Catal. Today*, 2016, **259**, 246–258.

- [58] G. Centi, S. Perathoner, in *Chemical Energy Storage*, R. Schlögl Ed., De Gruyter 2013, 379.
- [59] K.S. Joya, Y.F. Joya, K. Ocakoglu, R. van de Krol, *Angew. Chemie, Int. Ed.* 2013, **52**, 10426.
- [60] J. Barber, P.D. Tran, *J. Royal Soc. Interface*, 2013, **10**, 20120984.
- [61] M.D. Kaerkaes, O. Verho, E.V. Johnston, B. Aakermark, *Chem. Rev.*, 2014, **114**, 11863.
- [62] S. Fukuzumi, Y. Yamada, *ChemSusChem*, 2013, **6**, 1834.
- [63] D.K. Bora, A. Braun, E.C. Constable, *Energy & Env. Science*, 2013, **6**, 407.
- [64] K.P. Kuhl, E.R. Cave, D.N. Abramc, T.F. Jaramillo, *Energy & Environ. Sci.*, 2012, **5**, 7050.
- [65] D.W. Wang, D.S. Su, *Energy Environ. Sci.*, 2014, **7**, 576.
- [66] G. Centi, S. Perathoner, D.S. Su, *Catal. Surveys from Asia*, 2014, **18**, 149.
- [67] D.S. Su, S. Perathoner, G. Centi, *Chem. Rev.*, 2013, **113**, 5782.
- [68] L. Kaplan, *J. Org. Chem.*, 1985, **50**, 5376.

Characterization Tools:

X-Ray Diffraction (XRD):

XRD was performed to determine the crystal structure of the catalysts using a D2 Phaser Bruker diffractometer equipped with a Cu-K α radiation (1.5406 Å) source operating at 30 kV and 10 mA. A scan rate of 0.025°/s with a 2 θ range in 12° to 100° was used for data collection.

High Resolution Transmission Electron Microscopy (HRTEM):

HRTEM was used to understand the structural and morphological characteristics of the catalysts by using a MET JEOL 2100FEF (field effect gun energy filtering) microscope at the “Centre Technologiques des Microstructures”, CT μ Villeurbanne, France; equipped with an energy-dispersive x-ray (EDX) analyser.

X-Ray photoelectron spectra (XPS):

Quantitative surface analysis was performed by XPS using PHI 5000 VersaProbe II spectrometer with a monochromatic Al-K α X-ray source operated at 100 W, 20 kV.

Brunauer-Emmett-Teller (BET):

BET surface area and porosity of the catalytic material were analysed by N₂ adsorption/desorption at 77 K using an ASAS 2020 Micromeritics system. To degas the samples, a pre-treatment was performed at 10⁻⁴ Pa, 150 °C for 2 Hr.

Atomic absorption spectroscopy (AAS):

The amount of metal loading on the CNT substrate in the catalyst was determined using a Perkin-Elmer AAnalyst 200, atomic absorption spectrometer.

N₂ adsorption-desorption isotherms:

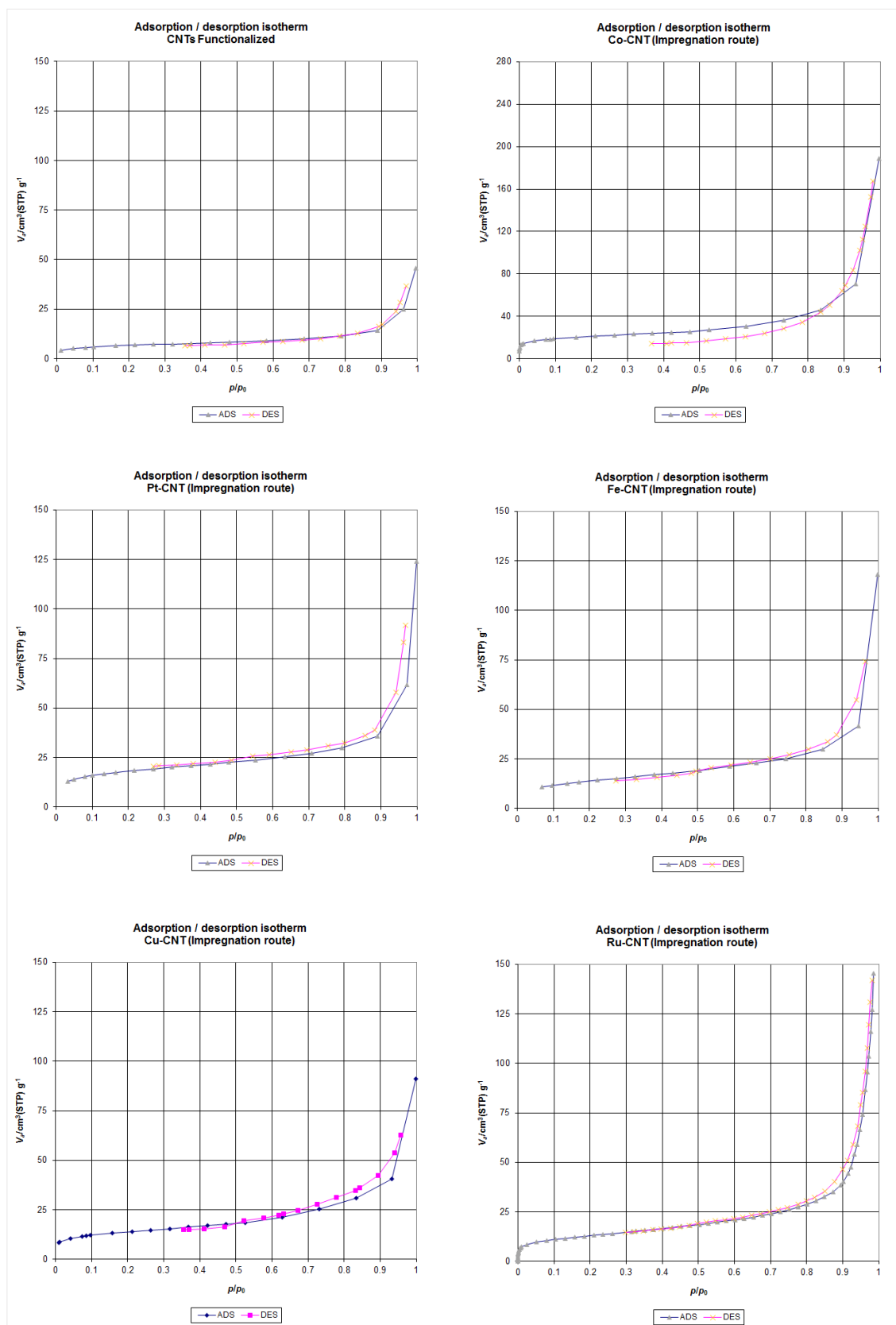


Fig. 3.11 N₂ adsorption/desorption isotherms for CNT_{ox}, Co, Pt, Fe, Cu and Ru NPs on CNT_{ox}.

Standard three-electrode system:

Voltammetry is the study of current variation as a function of applied potential. The potential is varied arbitrarily or continuously, and the actual current value is measured as the dependent variable. The shape of the graph depends on the speed of potential variation (nature of driving force) and on whether the solution is stirred or quiescent (mass transfer).

To perform such an experiment we need at least two electrodes – 1) Working electrode, (in contact with the analyte), need to apply the suitable potential in a controlled way and promote the transfer of charge to and from the analyte; 2) Electrode acting as the other half of the cell. This second electrode need to have a known potential value to have a reference for the potential of the working electrode, and also it must balance the charge added or removed by the working electrode. Although this is a viable setup, it has some shortcomings. One of them, is - it is very difficult for an electrode to supply a steady potential while passing current to counter redox reactions at the working electrode.

To solve this problem, the second electrode is divided into – 1) Supplying electrons and 2) Providing a reference potential. The reference electrode is a half cell with a measured reduction potential value. Its only function is to work as reference in measuring and regulating the working electrode's potential and at no point does it flow any current. The auxiliary electrode (counter electrode) flows all the current necessary to balance the current detected at the working electrode. This is achieved at the counter by often swinging to extreme potentials at the edges of the solvent window, where oxidation or reduction of the solvent or supporting electrolyte occurs. These electrodes, the working, reference, and auxiliary (counter) together make up the modern three electrode system shown in *Fig. 3.12*.

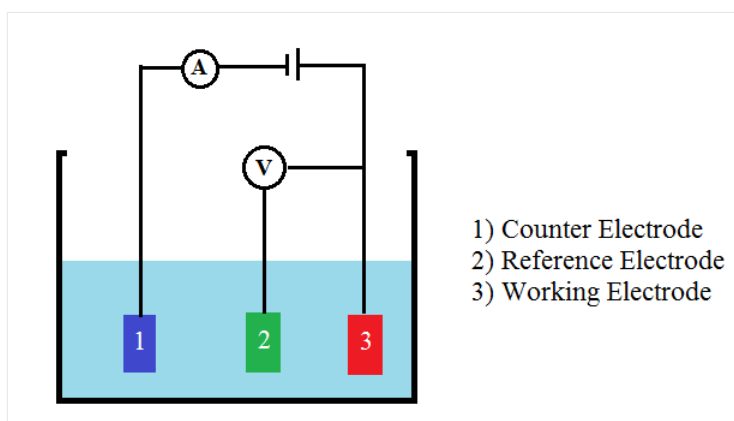


Fig. 3.12 Standard three-electrode cell configuration.

CHAPTER 4

Size controlled nanoparticles for liquid phase CO₂ electro-reduction

4.1. Introduction

4.1.1.State of the art (Organo-metallic (OM))

Metallic nanoparticles display applications from gas sensing, catalytic electrodes (photo, electro), magnetic, transparent conductors, templating, etc. [1-16]. their size typically range between 1 to 10 nm and the most classical synthetic route entails the reduction of metallic salts, possibly in presence of a stabilizing ligand [17]. The organo-metallic synthesis of nanoparticles is a preparation route to stable and mono-dispersed metallic small nanoparticles (typically between 2 and 4 nm in diameter) that has emerged less than 15 years ago [1-3]. This method follows the utilization of a ligand establishing a covalent bond with the metallic atoms of the nanoparticle's surface during the nanoparticle formation by reduction of monoatomic organometallic precursors (hence the name of organometallic synthesis which typically leads to the presence of a M-Si bond, but also a Me-Sn bond on the surface of the NP). The ligand is typically a long chain silane or stannane, etc which confers solubility in many solvents (both polar and apolar depending on the specific chain chosen), thus leading to very stable colloids thanks to the covalent (thus non-exchangeable) M-E bond.

The colloid can be used as precursor of supported or embedded metallic nanoparticles by impregnation or sol-gel hydrolytic processes followed by calcination. The use of an organometallic precursor as metal source allows the avoidance of some common catalytic poisons (typically Cl, NO₃, etc) that can be found on the surface of the calcined nanoparticle when other metal source (typically chlorides or nitrates) are used. Furthermore, the replacement of ligands commonly used to stabilize (non-organometallic) colloids, such as PVP, PVA or PEG, PAA with silane, generates the formation of more sintering-resistant NPs. The formation of porous siliceous patches at the support-nanoparticle interface during the calcination process can in part account for this increased stability toward sintering with respect to NPs obtained with common stabilizers (PVP, PVA, Fructose, etc). This makes the method an ideal choice for someone wanting to synthesize controlled catalytically active metallic nano-particles. Overall, the synthesis requires inert atmospheric conditions to prepare the necessary nano-materials. In literature, various approaches to achieve different metal or metal oxide or bi-metallic nanoparticles using varied precursor materials [1-8] exist. These works include Fe, Co, Ni, Pt, Pd, Ru, Sn, ZnO, Ni_xSi, NiPd, NiFe, FeCo, TiO₂, ZnO and many more [1-16].

The OM approach has mainly four parameters – 1) Precursors (organo-metallic complexes), 2) Solvent (simple or mixture), 3) Stabilization (by silane or stannane ligands which can act in some cases as reducing agent themselves etc) 4) Temperature, pressure, reducing agent [5, 7]. These nanomaterials can be further be loaded onto substrates or included into templates (membranes, mesoporous materials, etc) as needed for a specific study or application.

4.1.2. State of the art on Cu based nanoparticles (Nanowire (NW))

Recently, it was demonstrated that the presence of Cu nanoparticles (NPs) on the electrode surface can strongly influence the catalytic activity and selectivity during CO₂ electro-reduction [17]. Particularly, as compared with the bulk Cu electrode, Cu NPs under 5 nm exhibited a dramatic increase in the overall current density. In this direction, the ability to synthesize small Cu NPs onto a carbon support can be a useful approach, especially when the functional groups present on the carbon surface may take part in the reaction addressing the formation of the reduction products. In literature, there are quite a few research works to synthesize various Cu nano-materials. Comprehensive studies on the copper nanoparticles synthesis techniques had been already undertaken for their potential applications in electro and photo catalysis, anti-microbial and anti-fungal coatings, electric and thermal conductive coatings, lubricants and many more. Various methods in literature include pyrolysis [18], vapour depositions [19, 20], laser ablation [21], γ -irradiative hydrothermal routes [22, 23], electro and sono-chemical routes [24, 25], by reduction in solvents [26-28], liquid-phase co-precipitation [29]. Most of the above-reported nanoparticle syntheses yielded in Cu NPs with diameter of 5 nm or above [30]. Pyrolysis techniques yielded the NPs in the size range of 30-150 nm [18, 31], vapour depositions yielded in NPs in the size range of 20-45 nm [19, 20]. NPs of size 30 nm was achieved using laser ablation techniques [21], NPs in the size range of 30-35 nm were achieved using sono electrochemical route [25] and NPs in the size range of 5-20 nm were achieved using reductions techniques [28]. More importantly these preparation methods have many restraining factors for the viability and scalability to the potential applications. For instance, vapour depositions and laser techniques pose the problem of high costs and complex equipment, while other synthesis techniques such as reduction and co-precipitation are cost effective but compromising the size and uniformity.

In this context, a very easy and scalable synthetic route based on the preparation of Cu nanowires (NWs) followed by a deposition on activated nanocarbon-based electrodes was reported in this thesis as a novelty. The different inter-forces between Cu NWs and the functional groups present on the nanocarbon surface allow obtaining very small, uniform and stable Cu NPs of size less than 3.8 nm. Many studies reported on the NW synthesis in the past [32-36], which were used for various applications such as transparent conducting electrodes, solar cells, sensors, etc., but there are no evidence of the use of NWs to prepare small particles.

4.1.3. Scope of the chapter

The key goal of the research work presented in this chapter is to understand the effects of the size of nanoparticles (NPs) on the catalytic activity for CO₂ reduction. To accomplish this, there is the need to synthesize size-controlled nanoparticles, achieved by two different methodologies – i) organo-metallic route and ii) nanowire synthesis route (NPs synthesized using NWs). Small NPs of Pt, Ru, Fe were achieved via OM approach and very small Cu NPs were synthesized via NW approach. We were able to chart out novel synthesis routes for Fe NPs using OM approach and also a novel top-down approach from Cu NWs to ultrafine Cu NPs. Pt, Ru NPs were synthesized following a well-established OM approach in our research group. After successfully synthesizing the small NPs (Pt, Fe, Ru and Cu) loaded on CNTs were transferred on to gas diffusion layer (GDL). The thus formed working electrodes were tested for their catalytic performance on CO₂ reduction using a liquid phase cell (as discussed in *Chapter 3*).

4.2. Experimental

4.2.1. Synthesis of metal nanoparticles via organo-metallic route

All experiments were carried out under a controlled Argon atmosphere, using Schlenk and glove-box techniques.

Pt nanoparticle synthesis:

34 mg of Bis(dibenzylidene acetone) Platinum, Pt(dba)₂ (equivalent to 0.0513 mmoles) was dissolved in 34 ml of tetrahydrofuran, THF in a Schlenk and 20 µL of octylsilane, SiC₈H₂₀ was added as a stabilizing agent (also a reducing agent) to the final solution after carefully transferring into a glass reactor without any exposure to air. Then, constant stirring of 500 rpm

and a 3 bar H₂ pressure were maintained in the reactor. A basic scheme is shown in *Fig. 4.1*. The development in the reaction can be observed from the changes in the colour of the solution mixture, which turns dark brownish black. The setup was left overnight for 15 Hr to complete the reaction [12, 13]. The final metal NPs solution is concentrated to 1 ml (derived from the porosity of CNTs that was calculated using the diameter, length and approx. density of the CNTs) and ready to be deposited onto 100 mg of CNTs. The colloids were analysed by TEM and the colloidal solution was used for impregnation. This Pt NP synthesis is reported in the literature [12, 13].

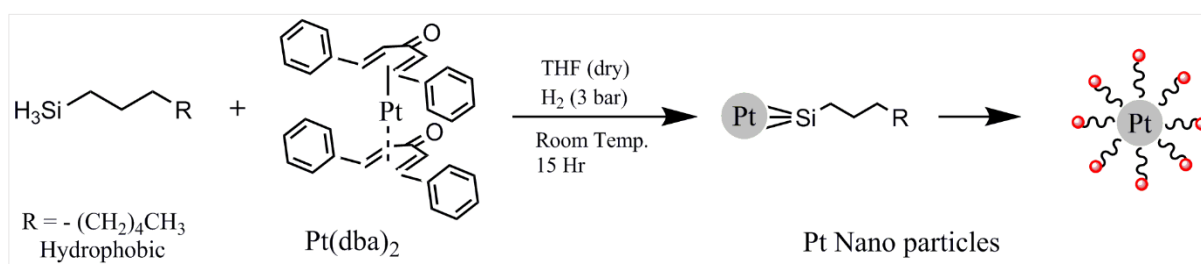


Fig. 4.1 Schematic showing organo-metallic synthesis of Pt NPs from $\text{Pt}(\text{dba})_2$.

Ru nanoparticle synthesis:

31 mg of (1,5-cyclooctadiene)(1,3,5-cyclooctatriene) ruthenium, $\text{C}_{16}\text{H}_{22}\text{Ru}$ (equivalent to 0.099 mmoles) was dissolved in 36.5 ml of tetrahydrofuran, THF in a Schenk and 10 μL of octylsilane, $\text{SiC}_8\text{H}_{20}$ was added as a stabilizing agent (also a reducing agent) to the final solution after carefully transferring into a glass reactor without any exposure to air. As described above, constant stirring of 500 rpm and a 3 Bar H₂ pressure were maintained in the reactor. A basic scheme is shown below *Fig. 4.2*. The development in the reaction can be observed from the changes in the colour of the solution mixture which turns dark brownish black. The setup is left overnight for 15 hr to complete the reaction [3]. The final metal NPs solution is concentrated to 1 ml (from porosity of CNTs as described above) and ready to be deposited onto 100 mg of CNTs. The colloids were analysed by TEM and the colloidal solution was used for impregnation. This Ru NP synthesis is reported in the literature [3].

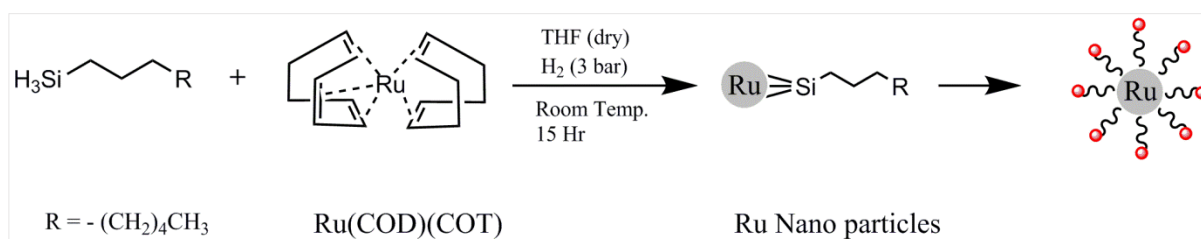


Fig. 4.2 Schematic showing organo-metallic synthesis of Ru NPs from $\text{Ru}(\text{cod})(\text{cot})$.

Fe nanoparticle synthesis:

60 mg of Iron (III) acetyl acetonate, $\text{Fe}(\text{acac})_3$ (equivalent to 0.1786 mmoles) was dissolved in a 60 ml mixture of Toluene and Hexane in 3:2 ratio. And 30 μL of octyl silane, $\text{SiC}_8\text{H}_{20}$ was added as a stabilizing agent (also a reducing agent) to the final solution after carefully transferring into a glass reactor without any exposure to air, thereby ruling-out the chances of oxidation of metal NPs. Then, constant stirring of 500 rpm and a 3 Bar H_2 pressure, 50 $^\circ\text{C}$ were maintained in the reactor. The application of H_2 speeds up the reaction and enables the reduction of M^{n+} to M^0 and constant stirring prevents the possibility of agglomeration. A basic scheme is shown below *Fig. 4.3*. The development in the reaction can be observed from the changes in the colour of the solution mixture which turns dark reddish orange. The setup is left overnight to complete the reaction. The final metal NPs solution is concentrated to 1 ml and ready to be deposited onto 100 mg of CNTs. The colloids were analysed by TEM.

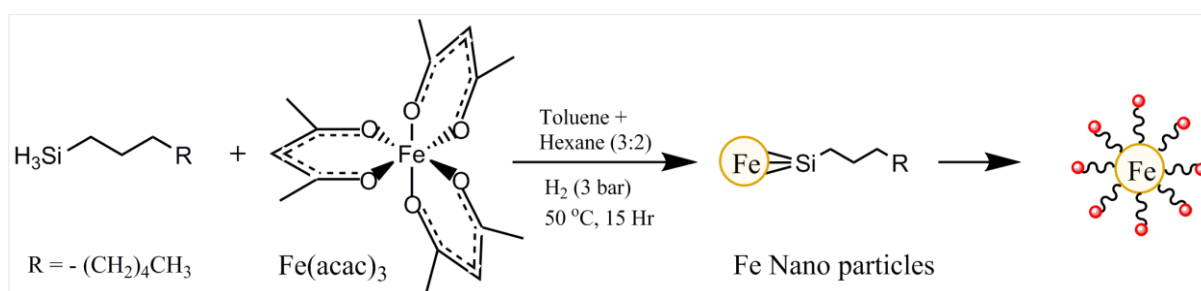


Fig. 4.3 Schematic showing organo-metallic synthesis of Fe NPs from $\text{Fe}(\text{acac})_3$.

4.2.2. Synthesis of metal nanoparticles via nanowire route

In this synthesis, we started with 7.6 mg of $\text{Cu}(\text{NO}_3)_2 \cdot 3\text{H}_2\text{O}$ salt (equivalent to 2 % of Copper metal by weight with respect to 100 mg of CNT or 2/63.5 moles of salt), 2% wt of Cu was chosen, so as to account for the losses in the separation phase and achieve at least 1 % Cu loading on CNT. The salt was mixed with (15 M, 10 ml) NaOH and then (3 mmol) EDA was added slowly under constant stirring at 750 rpm and temperature of 65 $^\circ\text{C}$ for 5 minutes. $\text{N}_2\text{H}_4 \cdot \text{H}_2\text{O}$ (1 mmol) was then added to the solution and the stirring was stopped after 3 minutes. As shown in *Fig. 4.4*, the solution undergoes various color changes starting from dark blue (Cu^{2+}) to white (Cu^+) and finally to pinkish red (Cu Nanowires – Cu NWs). When left undisturbed for 10 minutes, a slow settling of dark red macro particles can be seen floating towards the air-water interface indicating the formation of lighter Cu NWs. The NWs were analysed using TEM before and after deposition.

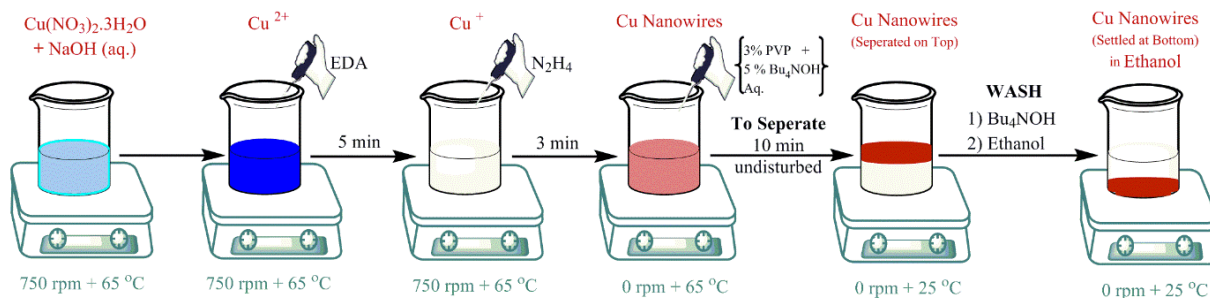


Fig. 4.4 A Schematic with the process steps involved in the Cu Nanowires synthesis.

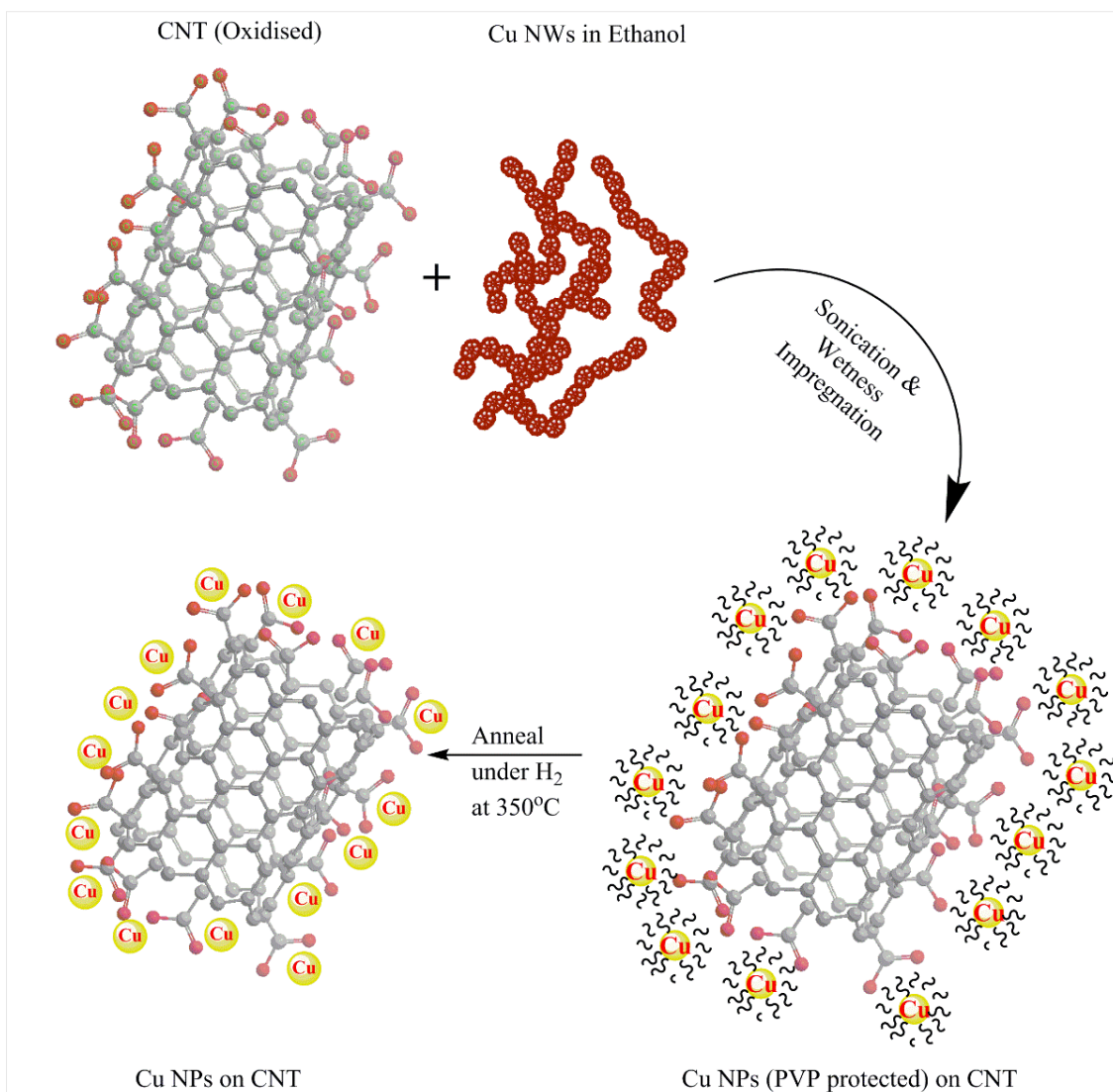


Fig. 4.5 A Schematic showing formation of Cu NPs from Cu NWs on the CNTs.

To separate the Cu NWs from the reaction solution, 10 ml aqueous solution consisting of 3 wt % PVP and 5 wt % Bu₄NOH was slowly added from the sides of the beaker. It can be clearly noticed that there are two layers, one thick semi-solid layer of Cu NWs and other thick

basic leftover solution. The Cu NWs can be separated using a separation funnel or simply by removing the unwanted solution using a pipette. The Cu NWs were further washed with 5 wt % Bu₄NOH, (2 times or more), to ensure the removal of PVP. Now, wash the Cu NWs twice with ethanol, and the final Cu NWs were left with ethanol as suspension solvent (1-2 ml equivalent to calculated wettability volume of 100 mg CNT). *Fig. 4.5* demonstrates the transferring of the Cu to CNTs; first the ethanol suspension was sonicated for 10 minutes at room temperature and then deposited on to CNTs using incipient wetness impregnation. Cu NWs ethanol suspension is added to CNTs drop by drop till it slightly wets the CNTs, then dry it in the oven at 70 °C. Repeat this process till the Cu NWs solution is exhausted. Now, the sample was dried overnight at 80 °C. Then, the dried sample was reduced at 350 °C (ramp rate 6 °C/min) for 2 hours under constant H₂ flow (25 ml/min).

4.2.3. Preparation of working electrode

Metal NPs loaded CNTs were mixed with 3-5 ml of ethanol, 1 drop of liquid Nafion (acts as a binding agent) and sonication was performed for 30 minutes to form a dark black ink. The ink was transferred onto GDL in multiple steps of deposition and drying, thus creating the final working electrode as shown in *Fig. 4.6*.

The catalysts were characterized using different techniques to determine the physical and structural properties. The characterizations include AAS, BET, HRTEM, XPS, XRD and current profiles as discussed in the result section.

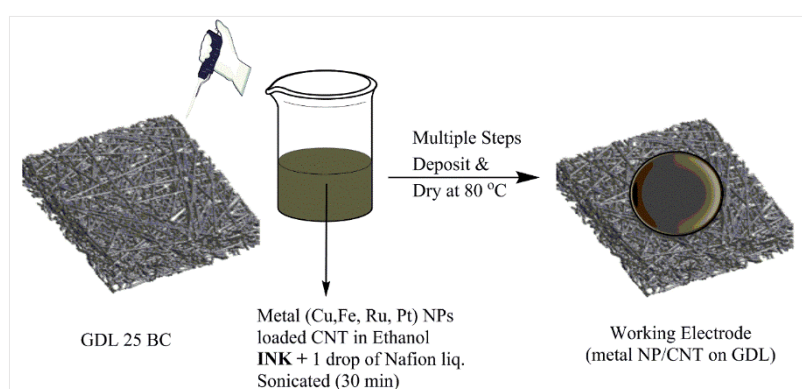


Fig. 4.6 Working electrode preparation by depositing metal NPs on CNT based INK on GDL.

4.3. Results and Discussions

4.3.1. Organo-metallic route

4.3.1.1. Synthesis and Characterization

The colloidal solutions of metal NPs were used to impregnate CNTs as discussed in [Chapter 3](#), which lead to formation of different sized metal NPs as shown here after –

In the OM synthesis route, one of the conditions applied was H₂ pressurization, used to speed up the reaction, and to enable the reduction of Mⁿ⁺ to M⁰ and constant stirring prevents the possibility of agglomeration. The reduction of organometallic complexes Pt(dba)₂ and Ru(COD)(COT) in presence of octyl silane under hydrogen (see [Fig. 4.1](#) and [Fig. 4.2](#)) leads to well dispersed small (1-2 nm) colloidal solution, as already reported elsewhere [3, 12, 13]. Although, we did not perform any intermediary characterization of the colloids at this stage, the characterization of the NPs after deposition on the CNT tend to corroborate that the syntheses were correctly performed and lead to well-dispersed NP of 1.1 nm and 1.3 nm in diameter, as expected.

Note that the iron precursor is actually a co-ordinate complex but the synthesis procedure followed is organometallic, which works in this case too. This specific conditions used in this route lead to 1 to 3 nm NPs in solution as shown in [Fig. 4.8](#), and on CNTs they were around 3-5 nm NPs (probably due to formation of thin oxide layer of 2 nm in air).

4.3.1.1.1. Structural Analysis

X-Ray Diffraction (XRD) was performed to determine the crystal structure of the catalysts. [Fig. 4.7](#) shows the XRD patterns for (a) bare-CNTs, (b) Fe-CNT, (c) Ru-CNT and (d) Pt-CNT synthesized via organometallic approach. In the diffraction pattern of [Fig. 4.7 \(a\)](#), the dominant peak at $2\theta = 26.45^\circ$ and several weak peaks at $2\theta = 43.30^\circ$ and 54.13° were observed, which correspond to the planes (002), (101), (004) of the CNTs (graphitic), respectively. In the [Fig. 4.7 \(b\)](#), the peak found at $2\theta = 44.88^\circ$ corresponds to the plane (110) of the Fe metal (BCC). In the [Fig. 4.7 \(c\)](#), the peak found at $2\theta = 44.37^\circ$ corresponds to the plane (101) of the Ru metal (HCP). In the [Fig. 4.7 \(d\)](#), peaks were observed at $2\theta = 39.85^\circ$ and 46.43° , corresponding to the planes (111) and (200) of the Pt metal (FCC), respectively. A common peak at $2\theta \sim 26.40$, found in all the metal NPs cases correspond to the CNTs (graphitic).

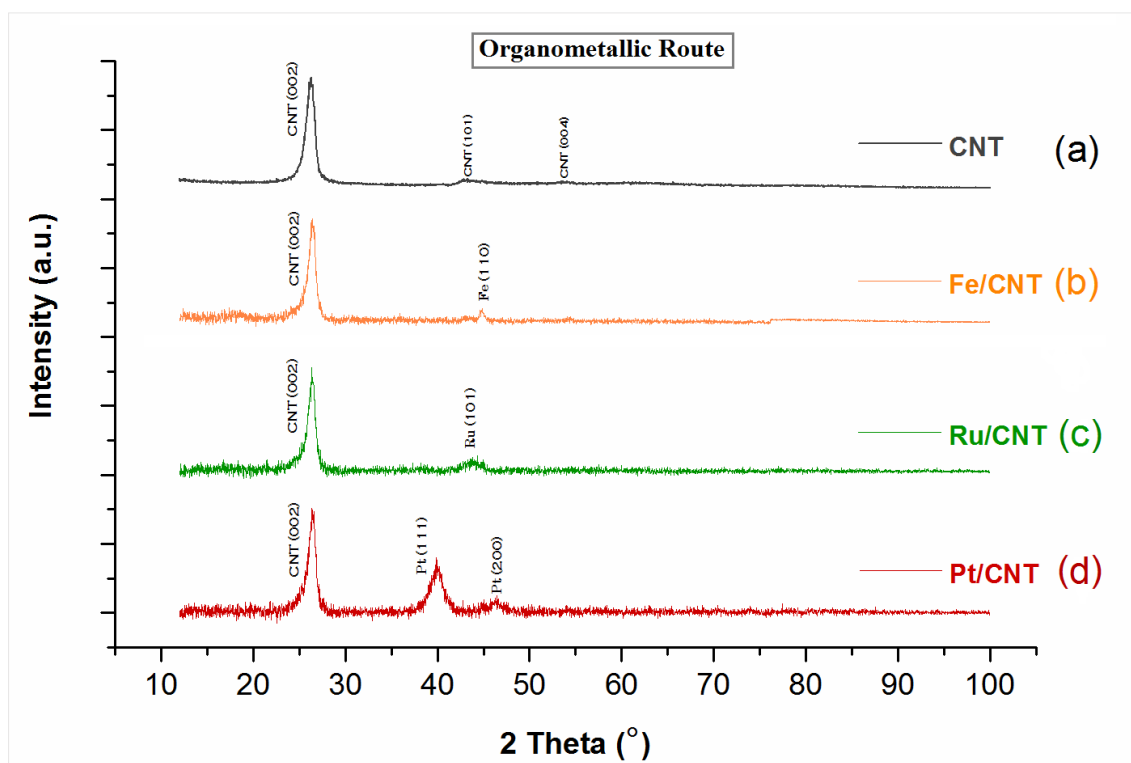


Fig. 4.7 XRD patterns (OM route) for (a) bare CNTs, (b) Fe-CNT, (c) Ru-CNT, (d) Pt-CNT.

4.3.1.1.2. TEM Morphological Measurements

High Resolution Transmission Electron Microscopy (HRTEM) was used to assess some structural and morphological characteristics of the catalysts. *Fig. 4.9 (a), (c), and (e)* provide micrographs and histograms of particle size distribution for Pt, Fe, and Ru NPs obtained via OM route. *Fig. 4.9 (b), (d), and (f)* show the corresponding STEM micrographs. A uniform (mono-disperse) distribution can be clearly noticed.

Table 4.1 provides detailed size distributions of the metal NPs on CNT in terms of mean standard deviation and range values as well as the corresponding data obtained on the homologous catalysts obtained by impregnation route. Thus showing that the NPs synthesized via Impregnation route were not as mono-disperse and generally bigger than the NPs obtained via the organometallic route (refer *Chapter 3*).

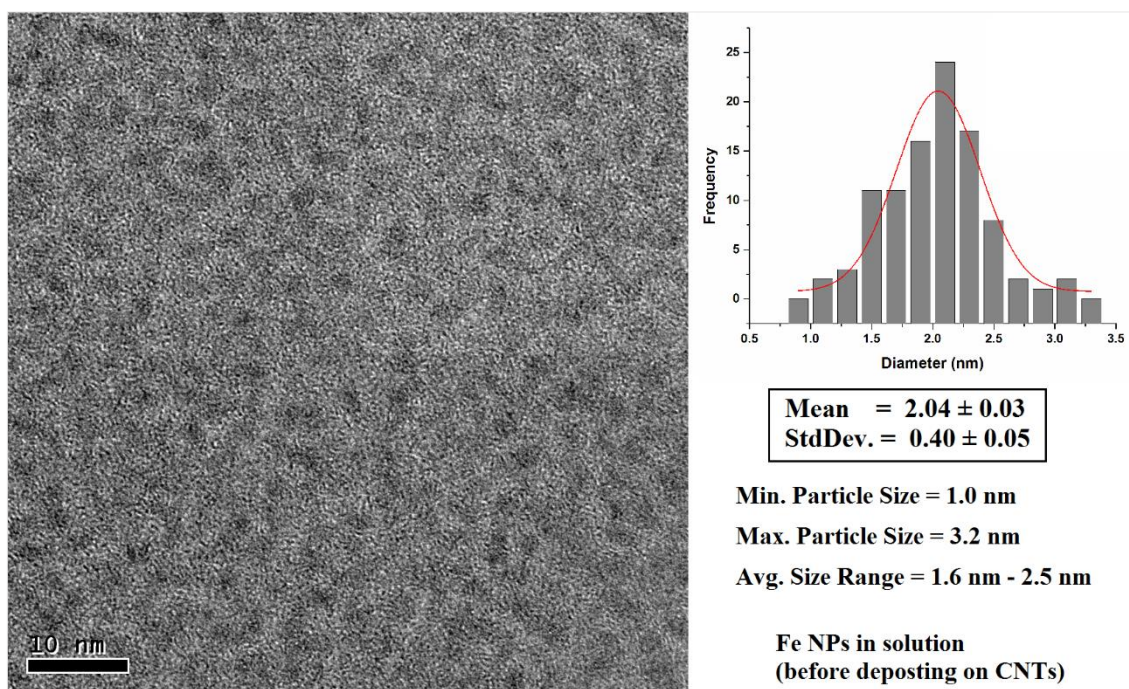


Fig. 4.8 TEM image showing Fe NPs colloidal solution via Organo-metallic route (1 – 3.2 nm).

Table 4.1 Detailed size distributions of Pt, Fe and Ru NPs via organo-metallic route.

Electro-catalyst	Particle Size (nm)		
	Mean	Standard Deviation	Min. – Max.
<i>Pt-CNT_{ox} (ImR Route)</i>	7.8	3.8	2.2 – 32.0
<i>Fe-CNT_{ox} (ImR Route)</i>	9.3	3.1	3.2 – 25.4
<i>Ru-CNT_{ox} (ImR Route)</i>	2.6	1.2	1.5 – 12.5
<i>Pt-CNT_{ox} (OM Route)</i>	1.1	0.3	0.7 – 1.8
<i>Fe-CNT_{ox} (OM Route)</i>	4.1	1.6	1.5 – 15.3
<i>Ru-CNT_{ox} (OM Route)</i>	1.3	0.4	0.7 – 2.7

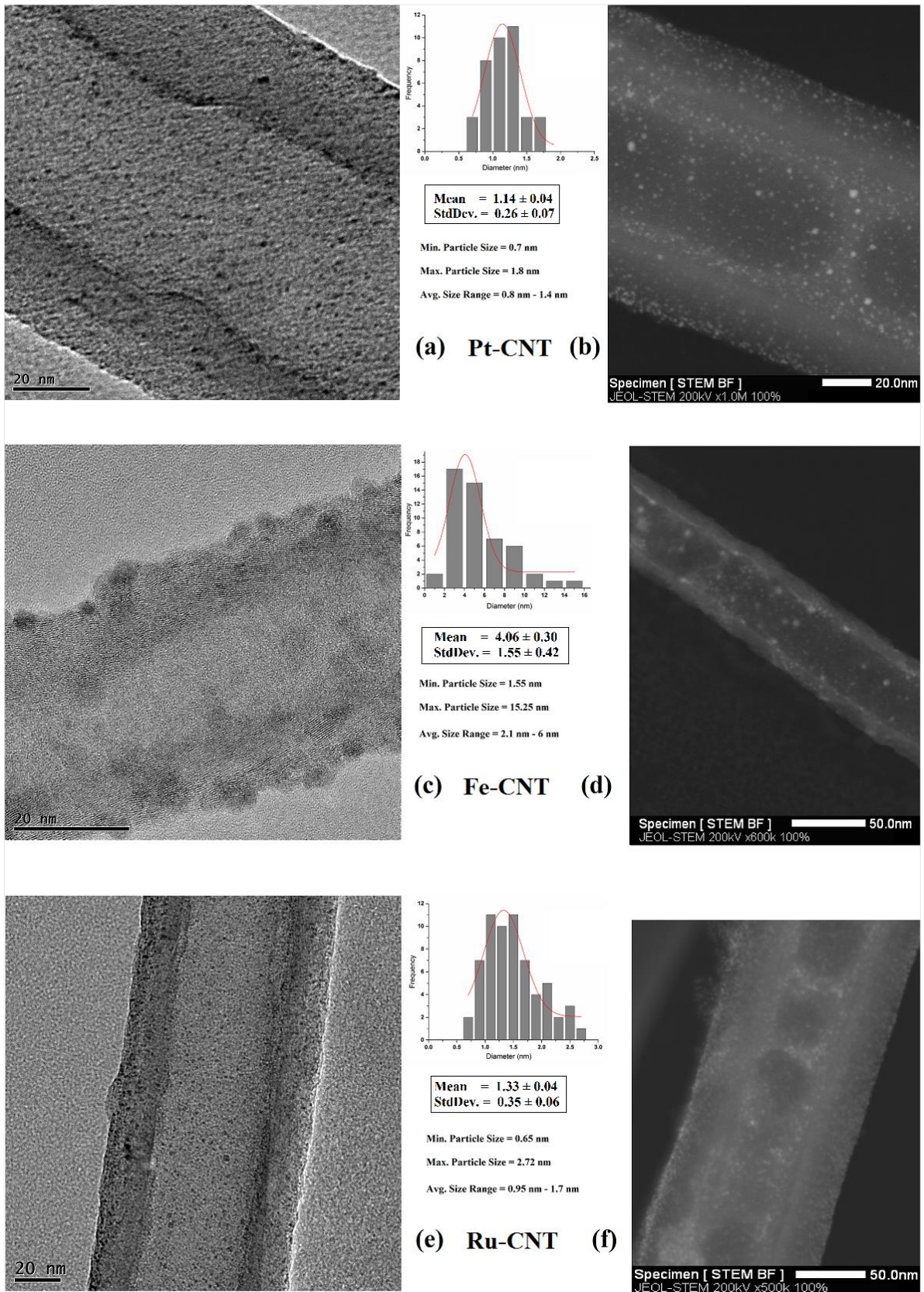


Fig. 4.9 TEM image showing Pt, Fe, and Ru NPs on CNT via Organo metallic route (0.9 nm - 5.6 nm) and STEM image showing the uniformity of metal NP loading on the CNTs.

4.3.1.1.3. Surface Analysis

A quantitative surface analysis performed by X-Ray photoelectron spectra (XPS) on the CNT-supported Pt, Ru and Fe nanoparticles. The survey gives an insight into the oxidation state of the Pt, Fe, Ru NPs and the different oxygen functionalities present on the CNTs. The The C-1s binding energy of adventitious carbon (284.9) served as the reference.

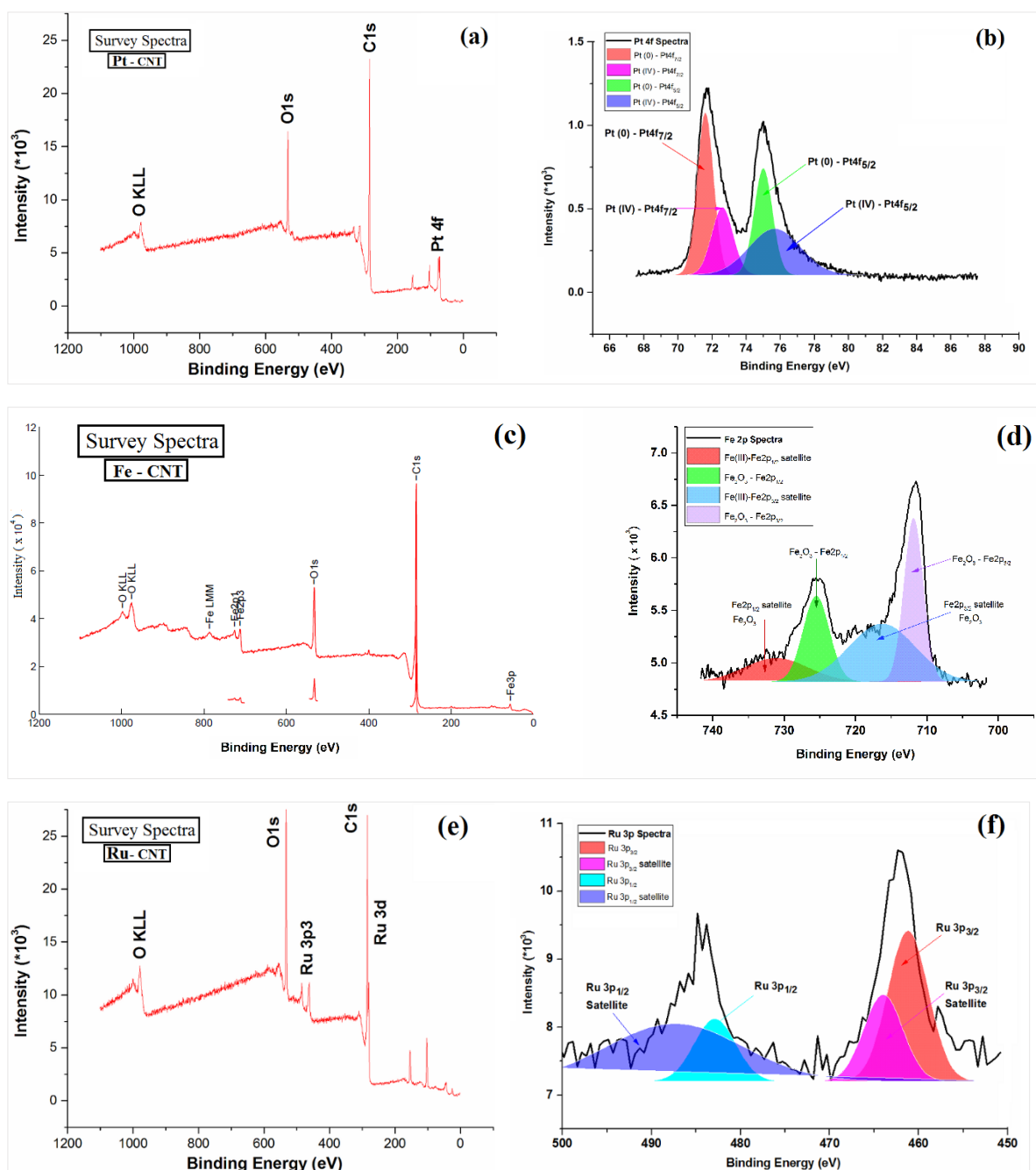


Fig. 4.10 (a, c, e) XPS wide scan survey spectra for Pt, Fe, Ru on CNT catalyst (OM Route) ; (b, d, f) High-resolution spectrum of the Pt 4f, Fe 2p, Ru 3p doublets and their respective deconvolution spectra.

Fig. 4.10 (a), (c) and (e) give a general survey of the Pt-CNT, Fe-CNT and Ru-CNT samples, respectively. *Fig. 4.10 (b)* shows the Pt oxidation state as mostly Pt (0) with a characteristic peak of 71.5 eV. In addition, a small peak of Pt (IV) observed at 75 eV. *Fig. 4.10 (d)* shows the Fe oxidation state as mostly Fe³⁺. The peaks found at 711.85 eV and 725.50 eV are the characteristic binding energies for the Fe³⁺ species, further confirmed by satellite peaks at 716.25 eV and 731.10 eV. *Fig. 4.10 (f)* shows the characteristic binding energy of Ru 3p at 461.65 eV. Ru is mostly in Ru (0), with the characteristic peak at 280.4 eV.

4.3.1.1.4. Quantitative and physical characterizations

Atomic absorption spectroscopy was used to make a quantitative analysis of the metal loading on the CNT substrate in the catalyst. The weight % of metal NPs on the CNT substrate prepared via different synthesis routes are reported in the *Table 4.2*. The initial loading weight of the precursor was same for both the routes (i.e. 10 % w.r.t. CNTs) and using same loading technique incipient wetness impregnation. However, the final % metal loading on the CNTs was found to be quite less for the OM route (1% to 5 %.) in comparison to that of the impregnation route (~ 9 %).

Table 4.2 Textural characteristics of the electro-catalysts by BET method.

Electro-catalyst	AAS (% wt. metal w.r.t. CNTs)	BET		
		a_{BET} ($m^2 \cdot g^{-1}$)	V_m ($cm^3 \cdot g^{-1}$)	Avg. pore diameter (nm)
<i>CNT_{ox}</i>	–	23.1	5.3	11.4
<i>Pt-CNT_{ox} (ImR Route)</i>	9.3	23.6	5.4	11.3
<i>Fe-CNT_{ox} (ImR Route)</i>	8.8	63.8	14.6	9.2
<i>Ru-CNT_{ox} (ImR Route)</i>	9.0	47.2	10.8	19.1
<i>Pt-CNT_{ox} (OM Route)</i>	2.0	21.2	4.8	13.0
<i>Fe-CNT_{ox} (OM Route)</i>	5.2	50.5	11.6	12.1
<i>Ru-CNT_{ox} (OM Route)</i>	2.0	40.9	9.4	11.2

The Brunauer-Emmett-Teller (BET) surface area and porosity of the catalytic material were analysed by N₂ adsorption/desorption. The characteristics are presented in the *Table 4.2*. An increase in the surface area and pore volume with respect to the metal-free starting CNT_{ox} can be clearly noticed. No significant change in average pore diameter can be explained as the

reduced sticking between the CNTs, due to the modified surface properties of functionalized CNTs during the metal NPs addition, except for Ru NPs. *Fig. 4.11* shows the N₂ adsorption-desorption isotherms for the Ru-CNT_{ox} via organo-metallic and ImR routes. For other metal NPs (Pt and Fe) the graph shown in *Fig. 4.20*, in the *annex*⁴.

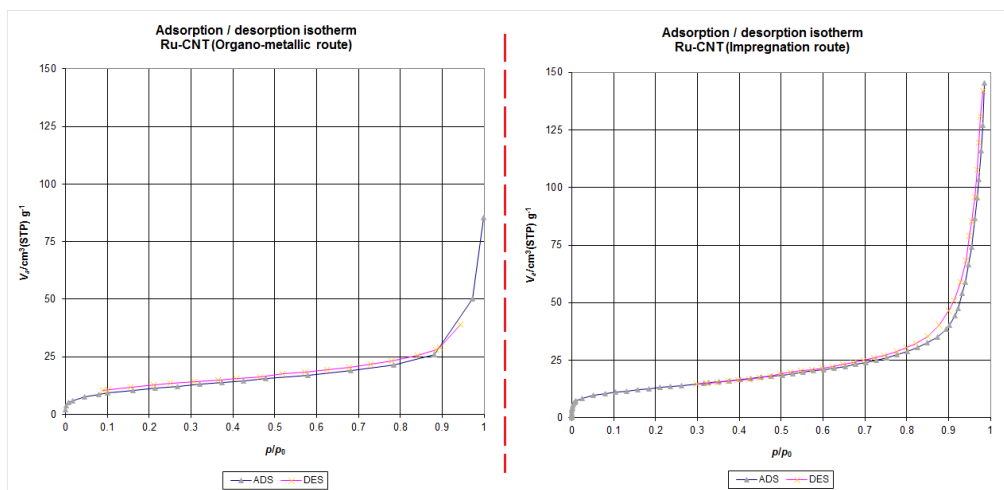


Fig. 4.11 N₂ adsorption/desorption isotherms for Ru NPs-CNT_{ox} (a) OM route, (b) ImR route.

4.3.1.1.5. Current profile

The electrocatalytic performances of the NPs loaded on the CNT were assessed after assembly with the GDL layer, as described in *Chapter 3*. The current profiles (in milli-amperes) for the CO₂ reduction reactions, for the different metal (Fe, Pt and Ru) doped CNT based electrodes formed via organometallic route are shown below in *Fig. 4.12*.

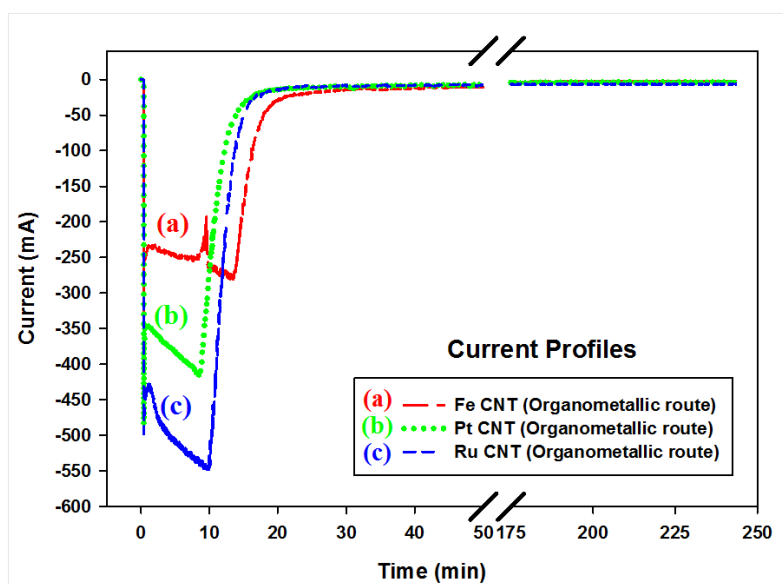


Fig. 4.12 Current profiles for OM route (a) Fe CNT_{ox}, (b) Pt CNT_{ox}, (c) Ru CNT_{ox}.

A constant potential of -2.0 V applied to the cell. It can be observed that the currents at the beginning of the reaction are quite high and then stabilize as an equilibrium P^H was achieved in the electrolytes in the anodic and cathodic compartments. Although the initial currents vary from 0.2 to 0.5 A, the equilibrium current lies in the range of 3 mA to 7 mA.

4.3.1.2. Electro-catalytic CO₂ reduction

4.3.1.2.1. Fuel productivity

The fuel productivity values for the catalysts synthesized via the organometallic route are shown in *Table 4.3*. The performance obtained on the analogous electrodes where the nanoparticles are obtained by classic impregnation route (ImR route, results from *Chapter 3*) are also shown in *Table 4.3* to facilitate the comparison between the two synthetic protocols. It is also evident from the *Table 4.3* that the selectivity for all metals shifted towards the H₂ production rather than CO₂ reduction with small nanoparticles. For the Ru metal, the productivity of C-products also increased while for the Pt metal, it was more or less same, and for Fe metal, we see a diminished productivity.

Table 4.3 Productivity for the CO₂ EC reduction in liquid phase cell (Units: $\mu\text{mol}\cdot\text{hr}^{-1}$).

CATALYSTS (%w metal)		FUELS ($\mu\text{mol}\cdot\text{hr}^{-1}$)								
		<i>Formic Acid</i>	<i>Acetic Acid</i>	<i>Methanol</i>	<i>Methyl Formate</i>	<i>Acetone</i>	<i>Iso-propanol</i>	<i>Ethanol</i>	<i>H₂</i>	<i>C-Products (NET)</i>
	<i>CNT_{ox}</i>	0.311	0.119	-	-	-	-	-	6.099	0.430
ImR Route	<i>Pt-CNT_{ox}</i> (9.3%w)	1.763	1.380	-	-	-	-	-	97.232	3.143
	<i>Fe-CNT_{ox}</i> (8.8%w)	0.414	0.483	-	0.276	-	-	-	32.263	1.173
	<i>Ru-CNT_{ox}</i> (9%w)	0.696	0.276	0.697	-	-	-	0.009	63.640	1.678
	<i>Ru-CNT_{ox}</i> (2%w)	0.084	0.058	0.026	-	-	-	0.004	49.260	0.172
OM Route	<i>Pt-CNT_{ox}</i> (2%w)	2.834	0.169						355.050	3.003
	<i>Fe-CNT_{ox}</i> (5%w)	0.372	-	0.235	-	0.006	0.004	-	63.348	0.617
	<i>Ru-CNT_{ox}</i> (2%w)	1.202	0.432	4.146	-	0.007	0.027	0.025	96.910	5.839

For Ru NPs (2%) via OM route when compared to the analogous material obtained by the salt impregnation route (ImR 2%), the formation increased by 14 times for formic acid, 7 times for acetic acid, 160 times for methanol, 6 times for ethanol and 2 times for H₂. The net C-products for Ru NPs (2%) OM route increased by 3.5 and 34 times for Ru NPs (10% and 2%) ImR route, respectively.

For Pt NPs via OM route, the productivity in net C-products remains more or less same but the H₂ formation increased by a factor of 3.6 with respect to the analogous material containing the Pt NPs synthesized via ImR route, even though the metal loading for the OM route is 2% wt. while ImR route loading is 10 % wt.

For the Fe NPs via OM route, the net C-products halved but the H₂ formation is twice higher over the Fe NPs via ImR route. Again, with the same discrepancy in metal loading.

A common aspect in all the afore-discussed results, the H₂ formation is favoured for smaller NPs, for all the metals (Ru, Pt, Fe). Also, the C-productivity increases for the NPs via OM route over the bigger NPs of ImR route. The better dispersion of the metal in the NP obtained by the organometallic route could partly explain this observation.

An estimate of the dispersion can be performed based on geometric consideration. The number of surface metal atoms ^[37, 38] can be calculated from the average NP diameter and the lattice constant of the unit cell of the metal ^[39] by using the below formulation –

$$N_{SA} = (n_{UnitCell} * \frac{V_{NPshell}}{V_{UnitCell}})$$

N_{SA} - Number of surface atoms per NP ; $n_{UnitCell}$ - Number of atoms per unit cell

$V_{UnitCell}$ - Volume of unit cell ; $V_{NPshell}$ - Volume of shell of NP

$V_{NPtotal}$ - Total volume of NP ; V_{NPcore} - Volume of core of NP

$$V_{NPshell} = (V_{NPtotal} - V_{NPcore})$$

$$V_{NPtotal} = \frac{\pi}{6}(\text{diameter of NP})^3$$

$$V_{NPcore} = \frac{\pi}{6}[(\text{diameter of NP}) - (\text{Lattice constant})]^3$$

Fraction of surface atoms = [(Number of surface atoms in NP) / (total number of atoms in NP)]

or $[V_{NPshell} / V_{NPtotal}]$

Table 4.4 Approximate calculated number of surface atoms and the fraction of surface atoms.

CATALYSTS (%w metal)		Diameter (nm)	Total Volume of NP (nm ³)	Volume of Core of NP (nm ³)	Volume of Shell of NP (nm ³)	Total Number of Atoms per NP	Number of Surface metal Atoms per NP	Fraction of Surface metal atoms
ImR Route	<i>Pt-CNT_{ox}</i> (9.3 %w)	7.8	248.2	213.4	34.8	16450	2306	0.14
	<i>Fe-CNT_{ox}</i> (8.8 %w)	9.3	420.7	382.9	37.8	35749	3208	0.09
	<i>Ru-CNT_{ox}</i> (9 %w)	2.6	9.2	6.6	2.6	2043	573	0.28
	<i>Ru-CNT_{ox}</i> (2 %w)	1.9	3.6	2.3	1.3	797	294	0.36
OM Route	<i>Pt-CNT_{ox}</i> (2 %w)	1.1	0.7	0.2	0.5	46	33	0.72
	<i>Fe-CNT_{ox}</i> (5.2 %w)	4.1	36.1	29.0	7.1	3063	599	0.20
	<i>Ru-CNT_{ox}</i> (2 %w)	1.3	1.2	0.6	0.6	255	128	0.50

Using the above formulation, the approximate number of surface atoms and the fraction of surface atoms calculated values are as shown in [Table 4.4](#). From these data, it is observable that the fraction of surface atoms for the smaller NPs via OM route is higher than the bigger NPs via ImR route and works as one of the factors for the increased fuel productivity values.

4.3.2. Nanowire route (Cu NWs to get Cu NPs)

4.3.2.1. Synthesis and Characterization

The colloidal solutions of metal nanowires were used to impregnate CNTs as discussed in [Chapter 3](#), which lead to formation of different sized metal NPs as shown here after –

The nanowires were characterized using TEM before impregnation. The final CNT based catalysts were characterized using different techniques to determine the physical and structural properties as performed for the Pt, Ru, and Fe catalysts discussed above.

4.3.2.1.1. Structural Analysis

X-Ray Diffraction (XRD) was performed to determine the crystal structure of the catalyst. XRD for bare CNTs and Cu (via ImR route) are also provided to have a better comparison.

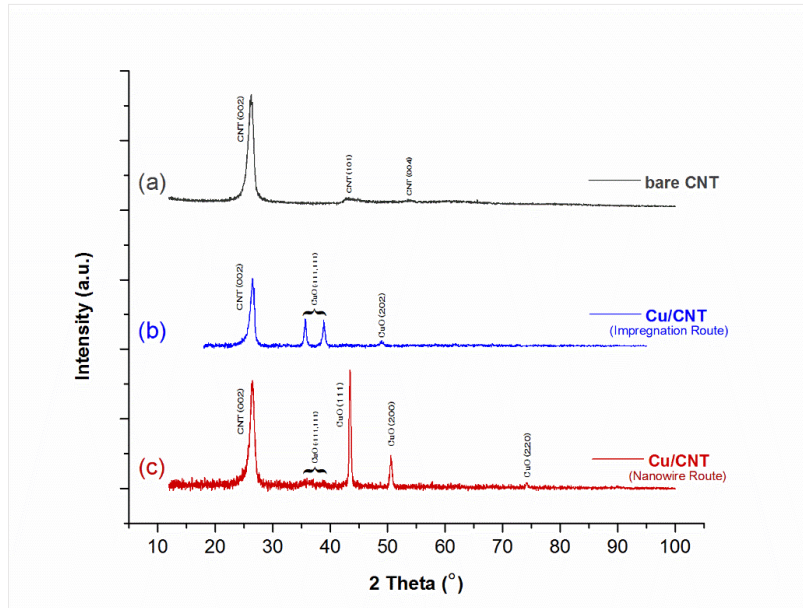


Fig. 4.13 XRD patterns (a) bare CNTs, (b) Cu-CNT (ImR route), (c) Cu-CNT (NW route).

Fig. 4.13 shows the XRD patterns for (a) bare-CNTs, Cu-CNT (ImR route), and (c) Cu-CNT (NW route). In the diffraction pattern reported in *Fig. 4.13 (a)* the dominant peak at $2\theta = 26.35^\circ$ and several weak peaks at $2\theta = 43.30^\circ$ and 54.13° were observed, which correspond to the planes (002), (101), (004) of the CNTs (graphitic), respectively. In *Fig. 4.13 (b)*, 2 twin peaks were observed at $2\theta = 35.67^\circ$ and 38.90° , corresponding to the planes (-111) and (111), respectively and a weak peak at $2\theta = 48.97^\circ$, corresponding to the plane (202), of Cu oxide (monoclinic). From *Fig. 4.13 (c)*, 3 peaks at $2\theta = 43.44^\circ$, 53.64° , and 74.11° , corresponding to the planes (111), (200) (220), respectively of the FCC of Cu metal can be identified. Also, weak peaks are observed at $2\theta = 35.96^\circ$ and 38.76° , which may correspond to small amounts of CuO formed. The dominant peak at $2\theta \sim 26.40^\circ$ is found in all the cases which corresponds to the CNTs (graphitic).

4.3.2.1.2. TEM Morphological Measurements

High Resolution Transmission Electron Microscopy (HRTEM) was used to understand the structural and morphological characteristics of the Cu NWs and Cu NPs on the CNTs. *Table 4.5* provides detailed size distributions of the Cu NPs on CNT in terms of mean, standard deviation, range values and of Copper nanowires before impregnation.

Table 4.5 Detailed size distributions of Cu-CNT via nanowire (NW) and ImR routes.

Electro-catalyst	Particle Size (nm)		
	Mean	Standard Deviation	Min. – Max.
<i>Cu-CNT_{ox}</i> (ImR route)	10.4	4.4	3.6 – 39.0
<i>Cu-CNT_{ox}</i> (NW route)	2.9	0.9	1.5 – 6.5
	<i>Length</i>	<i>Avg. Diameter</i>	<i>Outer PVP Covering Thickness</i>
Nanowire before impregnation	5-30 μ m	147 \pm 5 nm	12 \pm 1 nm

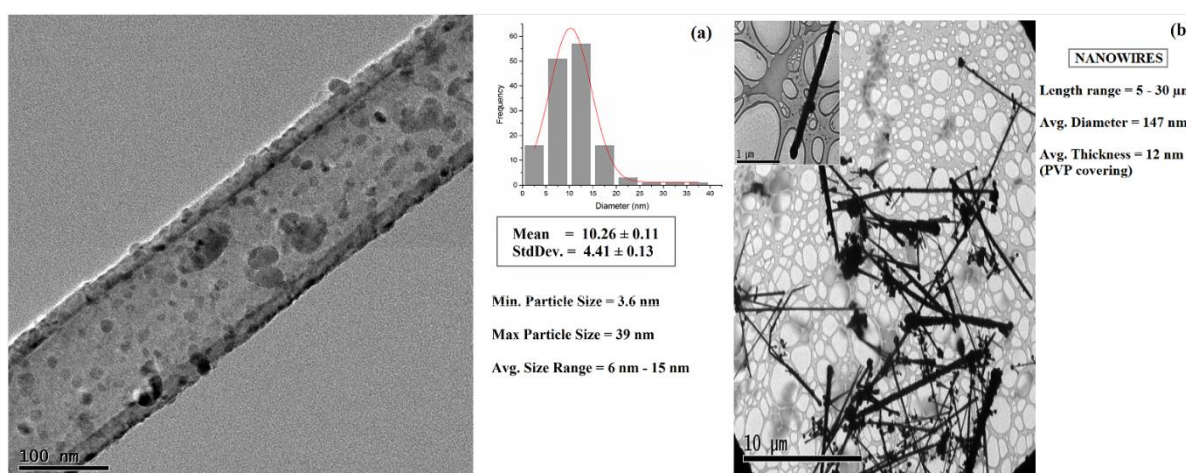


Fig. 4.14 TEM image showing (a) Cu NPs on CNT for ImR route (5 nm - 16 nm), (b) Cu nanowires before deposition onto CNTs.

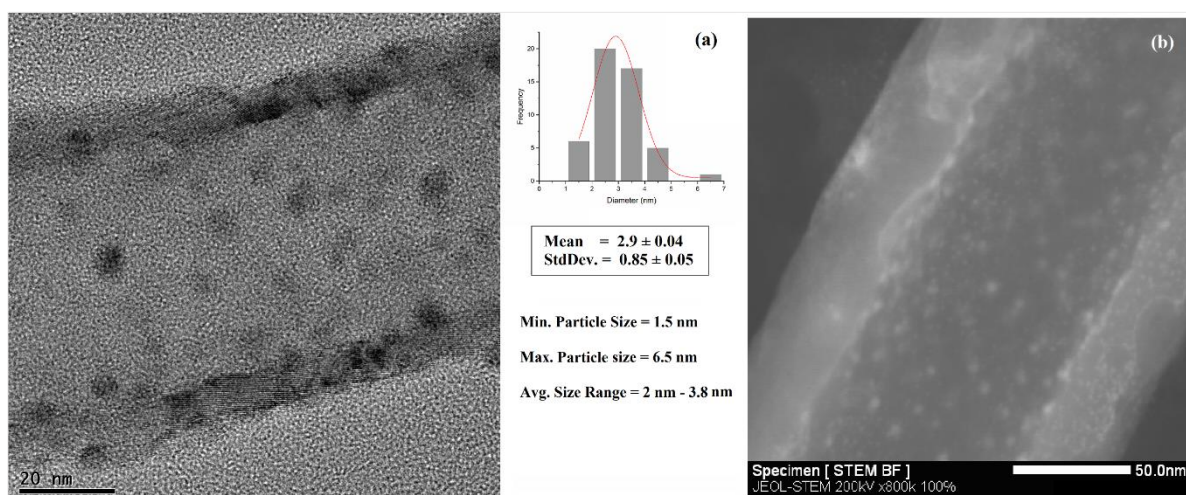


Fig. 4.15 TEM image showing Cu NPs on CNT via NW route (2 nm - 3.8 nm) and STEM image showing the uniform dispersion of the Cu NPs on the CNT.

As shown in *Fig. 4.14 (a)*, the average size of the Cu NPs obtained through the ImR route was measured to be 6 nm - 15 nm and non-uniformly distributed; *Fig. 4.14 (b)*, shows the nanowires formed which are 5-30 μm long and have an average diameter of 147 nm. Now these nanowires were transferred onto CNTs after sonication, obtaining the Cu NPs shown in *Fig. 4.15 (a)*, which have a uniform distribution and very fine size range of 2 nm - 3.8 nm. This followed a top-down approach from very long and thick nanowires to achieving very fine Cu NPs. *Fig. 4.15 (b)*, is a STEM image showing the uniformity of the distribution of NPs.

4.3.2.1.3. Surface Analysis

A quantitative surface analysis was performed by X-Ray photoelectron spectra (XPS). The survey gives an insight into the oxidation state of the Cu NPs and the different oxygen functionalities present on the CNTs.

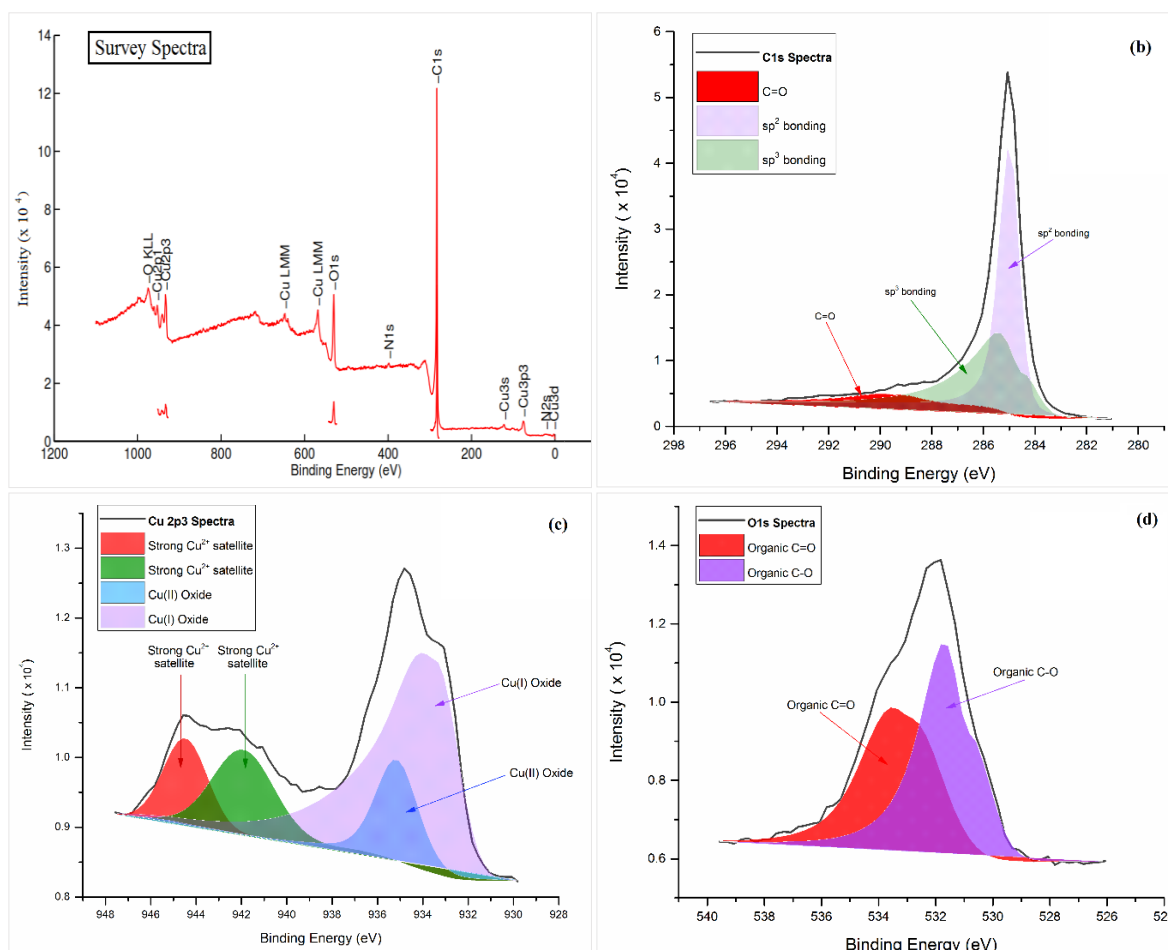


Fig. 4.16 (a) XPS wide scan survey spectra for Cu/CNT catalyst, (b) XPS data illustration of the C1s and respective deconvolution spectra, (c) High-resolution spectrum of the Cu 2p doublet and respective de-convolution spectra, (d) XPS data illustration of the O1s and respective de-convolution spectra.

Fig.4.16 (a) gives a general survey of the sample, *(b)* explains the type of carbon bonding present. The reference was set using the C-1s binding energy of adventitious carbon (284.9). *Fig.4.16 (c)* Shows the Cu oxidation state as mostly Cu^{2+} and Cu^+ , the peak at 934.8 eV represents the characteristic binding energy for the Cu^{2+} species, which is further confirmed by satellite peaks at 942 eV and 944.5 eV. The peak at 933 eV matches for the Cu^+ binding energy. *Fig.4.16 (d)* illustrates the possible oxygen-carbon bonding found. This shows that there are some oxygen functional groups left over after the Cu NPs were loaded on the CNTs.

4.3.2.1.4. Quantitative and physical characterizations

Atomic absorption spectroscopy was used to make a quantitative analysis of the metal loading on the CNT substrate in the catalyst. The weight % of Cu on the CNT substrate were found to be - Cu-CNT (ImR route) ~ 9.5 % and Cu-CNT (NW route) ~ 1-1.3 %. The Brunauer-Emmett-Teller (BET) surface area and porosity of the catalytic material were analysed by N_2 adsorption/desorption. The characteristics are presented in the *Table 4.6*.

An increase in the surface area and pore volume can be clearly noticed which follows in accordance with the addition of Cu NPs and decreasing size of Cu NPs. No significant change in average pore diameter may be due to the reduced sticking between the CNTs, due to the modified surface properties of functionalized CNTs during the Cu NPs addition. These values attribute to the increased catalytic active area and increased fuel productivity, in tune with the results. *Fig. 4.17* shows, the N_2 adsorption-desorption isotherms for the Cu CNT via NW route and ImR routes.

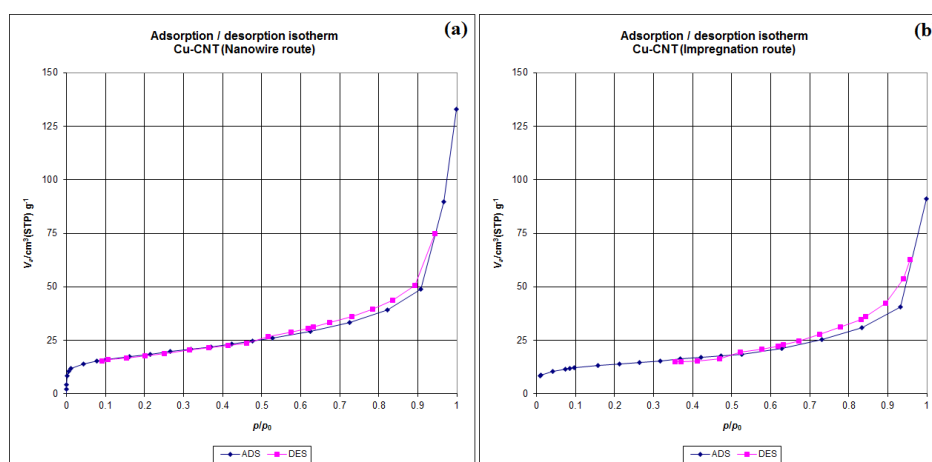


Fig. 4.17 N_2 adsorption/desorption isotherms for Cu NPs-CNT_{ox} (a) NW route, (b) ImR route.

Table 4.6 Textural characteristics of the electro-catalysts by BET method.

Electro-catalyst	$a_{BET} (m^2 \cdot g^{-1})$	$V_m (cm^3 \cdot g^{-1})$	Average pore diameter (nm)
CNT_{ox}	23.1	5.3	11.4
$Cu-CNT_{ox}$ (ImR route)	48.3	11.1	10.8
$Cu-CNT_{ox}$ (NW route)	64.3	14.8	11.7

4.3.2.1.5. Current profile

The current profiles for the CO_2 reduction reactions, for the two different Cu CNT based electrodes formed via NW route and ImR route are shown below in [Fig. 4.18](#). In the case of ImR route catalyst the current in the beginning of the reaction is quite high and then stabilizes as the P^H in the anodic compartment stabilizes itself. A similar trend is seen for the Cu CNT electrode (NW route), but the starting current is significantly lower compared to the other case.

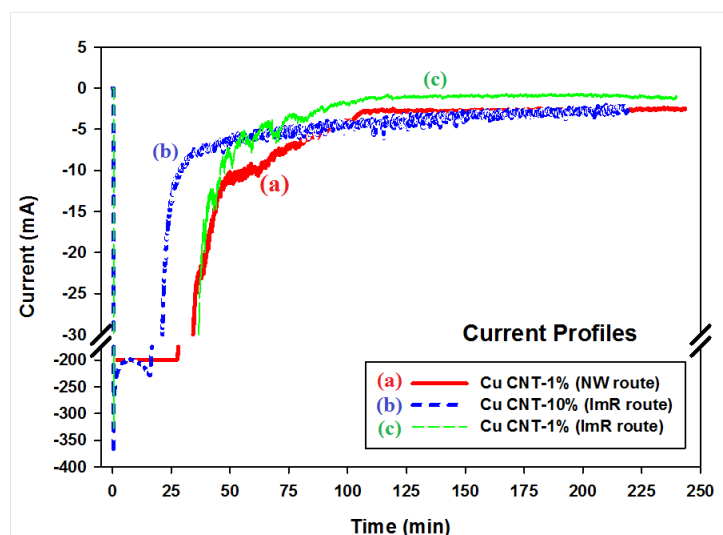


Fig. 4.18 Current profiles for $Cu\ CNT_{ox}$ (a) NW route, (b) 10%, ImR route, (c) 1%, ImR route.

4.3.2.2. Electro-catalytic CO_2 reduction

4.3.2.2.1. Fuel productivity

The fuels produced during the electrochemical reduction of CO_2 were analysed using various techniques, which include IC, GC-Mass, 1H NMR, and GC-TCD. The major liquid products detected in the liquid electrolyte on the cathode side were formic acid, methanol and acetic acid. Minor quantities of acetone, isopropanol and ethanol were also found. And GC-TCD was used to detect gaseous products H_2 , CH_4 and CO . But the CH_4 and CO values were quite below the sensitivity of the GC-TCD analysis. The products obtained are shown in [Table 4.7](#) for the

two different sized Cu NPs based electrocatalysts and also, to provide a reference – results of CNT (oxidised) alone are presented (i.e. without any metal NPs, CNT deposited on the GDL).

Cu NPs (1% wt. loading, ImR route) was also carried out, to have a better comparison with the Cu NPs (NW route). The results are expressed in micromoles of the products obtained for a given time of the reaction. The results given in the [Table 4.7](#) are performed under similar conditions, with potentiostatic conditions (- 2V), and constant CO₂ flow rate of 10 ml/min and the catalytic surface area ~ 5.7 cm². The presence of a Cu NPs on CNT_{ox} leads to a substantial increase in the productivity for the conversion of CO₂. When the Cu NPs size is varied, the productivity changes drastically, indicating that NPs size have a significant effect on the reaction mechanism and selectivity of products.

Table 4.7 Products obtained in the CO₂ electro-chemical reduction in liquid phase cell.

FUELS ($\mu\text{mol}\cdot\text{hr}^{-1}$)	CATALYSTS			
	CNT _{ox} *	Cu-CNT _{ox} (1% Cu) (ImR route)*	Cu-CNT _{ox} (10% Cu) (ImR route)*	Cu-CNT _{ox} (1% Cu) (NW route)*
Formic Acid	0.094	0.431	0.542	1.713
Acetic Acid	0.258	0.260	0.617	0.369
Acetone	-	0.010	0.005	0.002
Methanol	-	0.020	0.309	0.976
Isopropanol	-	0.000	0.000	0.002
Ethanol	-	0.031	0.000	0.006
H ₂	6.099	14.025	35.357	93.190
C-Products (NET)	0.352	0.752	1.473	3.068

* ImR- impregnation; NW – Nanowire; ox-functionalized.

With decrease in the NP size, the productivity increases by 3.2 times in the case of formic acid and methanol but decreased by 1.7 times for acetic acid in the comparison of 1% NW route with 10 % ImR route. While the productivity increases by 4 times in the case of formic acid, 49 times in the case of methanol and increased by 1.4 times for acetic acid in the comparison of 1% NW route with 1 % ImR route. This indicates that the selectivity of products is dependent on the NP size. In terms of net C-products, the productivity for ultrafine Cu NPs (1%) increased by 2.1 times and 4 times over larger Cu NPs 10% and 1%, respectively as observed from [Table 4.7](#). Also, this is in quite a good agreement with the BET surface area (S.A. ratio = 64.3/48.3 ~ 1.33) measurements shown in [Table 4.6](#).

Considering that, we used only 1-1.3 % wt. loading of Cu (Ultrafine NPs - NW route) against 9.5 % wt. loading of Cu (large NPs - ImR route), equivalently 8 times less loading. Also, using the formulation discussed above for the surface atoms and their fractions, the number of surface atoms of Cu NPs via ImR and NW routes are 7123 and 355, respectively. In addition, the fraction of surface atoms of Cu NPs via ImR and NW routes are 0.12 and 0.33, respectively. We can see the same increased trend in the fraction of surface atoms, which is one of the factors for higher fuel production. The other major product in the reaction is H₂

The productivity is quite high in the case of Cu (small NPs - NW route). The productivity factor is about 3 times in comparison to Cu (large NPs - ImR route, 10% Cu), while the factor is 7 times for the 1% ImR case. The H₂ formation is the major factor leading to the decrease in the carbon atom efficiency. The huge increase in the H₂ production for smaller NPs, is in a good agreement with reported studies in literature where several experimental and DFT calculations were performed for different metals [17, 40].

A time dependent study conducted on the products formed is shown in *Fig. 4.19* for both the Cu NPs catalysts with 1% loading. For the small NPs, the formation of H₂ and acetic acid increase with time whereas formic acid formation rate falls by small factor, which fits the supposed mechanism (discussed in *Chapter 3*) scheme where formic acid is converted to acetic acid. For the larger NPs, with time both acetic and formic acid values increase slowly but the H₂ production decreases. The reaction run-time was increased from 4 hr to 20 hr and also, the working electrodes were reused, to see if there is a significant loss in the catalytic activity. The fuel productivity values were found to be constantly increasing with time and also, the re-use of the electrodes showed similar results.

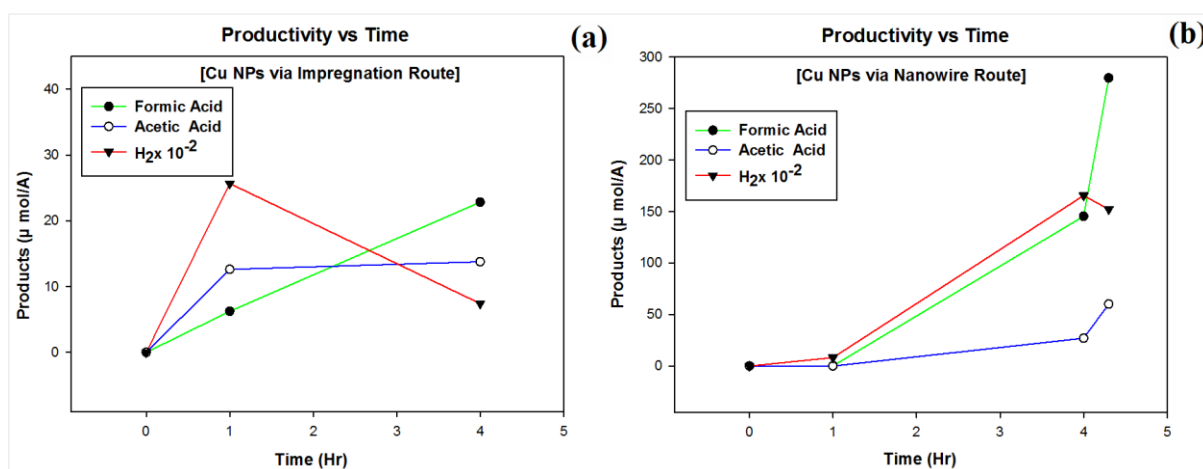


Fig. 4.19 Time dependence vs productivity of formic acid, acetic acid and H₂ for Cu NPs on CNT_{ox} (a) 1%, ImR route, (b) 1%, NW route.

Turnover frequency (TOF) values for the results have been calculated in order to have a better idea about the productivity values of fuels and the enhancements achieved. To have a correlation with other reported results in the literature in terms of TOF is not simple as the operating conditions of the cell, electrodes and cell design itself are not comparable. TOF values presented in the literature Kuhl et al. [41] have been considered to have a comparison. Also, the total TOF value of all products combined is taken as the basis for comparison, since the type of catalytic electrode (Copper electrode @ Kuhl et al. [41]) is very different. The TOF values thus obtained are given in *Table 4.8*. The units for the TOF data are reported in micromole per unit area per unit time ($\mu\text{mol}\cdot\text{s}^{-1}\cdot\text{cm}^{-2}$). The CO formation in our case is well below the detection limits in our case, so the CO amount from the literature [41] are differentiated to be accounted or not. However, the impact is minimal.

Table 4.8 TOF values ($\mu\text{mol}\cdot\text{s}^{-1}\cdot\text{cm}^{-2}$) on Cu CNT (nanowire and impregnation routes) based electrodes, in comparison with TOF values reported by Kuhl et al. [41] (*) for Cu foil electrode.

Electrode	<i>TOF (all products)</i>	<i>TOF (all products, except CO)</i>
<i>CNT_{ox}</i>	1.52e-3	-
<i>Cu-CNT_{ox} (ImR Route, 10%)</i>	5.94e-3	-
<i>Cu-CNT_{ox} (ImR Route, 1%)</i>	3,03e-3	-
<i>Cu-CNT_{ox} (NW Route, 1%)</i>	1,24e-2	-
<i>Cu foil (*)</i>	6,96e-3 *	6,66e-3 *

From the *Table 4.8*, it is evident that the TOF value in the case of Cu-CNT_{ox} (NW route) electrode is a good 100 % to 300% higher with respect to the Cu-CNT_{ox} (ImR route), 10% and 1%, respectively and nearly 80 % higher with respect to the values reported in literature [41] for (Cu foil). We can draw same evidence using the dispersion (surface atoms) formulation, assuming the Cu foil to be group of NPs of 10 nm together. Then, the number of surface atoms would be many factors less in comparison to the Cu NPs on CNTs.

4.4. Conclusions

Organo-metallic synthesis route was used for synthesizing CNT loaded with Pt, Ru and Fe NPs and nanowire route for Cu NPs loaded CNTs to attain uniform, well dispersed and small sized nanoparticles of (avg. size – 1.1 nm Pt; 1.5 nm Ru; 2.9 nm Cu; 5 nm Fe). The NPs were also found to be quite stable. A novel synthesis route and specific conditions have been presented to obtain small Fe NPs of size (1-5 nm; average NPs size = 2 nm in solution phase before transfer onto CNTs).

An elaborate study on the metal doped CNT based catalysts for Electro-catalytic CO₂ reduction is presented. The various products detected in the liquid phase and the selectivity towards different products have been discussed. The carbon support is shown to have a very active role unlike the common notion of inactive support.

An insight into the CO₂ reduction to fuel productivity dependence, on the type of the nanoparticle synthetic routes is presented for the electrodes formed using different electrocatalysts. (i) CNT_{ox} considered to draw a reference value; (ii) Fe, Pt, Ru and Cu - CNT_{ox} (via impregnation route) creating nanoparticles of average sizes (9.3 nm Fe; 10.4 nm Cu; 7.8 nm Pt; 2.6 nm Ru); (iii) Fe, Pt, Ru and Cu - CNT_{ox} (via organo-metallic route and nanowire route) for very small nanoparticles formation (size range 1–5 nm). The study shows that there is as much as 1 full-order increase in the carbon fuel productivity for Cu, Ru when changing the synthetic procedure. For the Pt NPs case, the C-fuels productivity increased by 5 times and for the Fe NPs case, the C-fuels productivity more or less remains same as the most of the energy is utilized towards the H₂ generation. A similar trend is observed for the decreasing size of NPs which lead to higher hydrogen evolution reaction (HER). Also, by comparing OM and ImR routes catalysts (Ru, Pt, Fe and Cu), the productivity of the gaseous H₂ fuel increased by a factor of 2, 1-order, 4 and 7 times, respectively. This is worth the note, though it is not the major goal for the CO₂ reduction reaction.

The reusability of the working electrodes is also worked upon and long reaction times were also probed. In terms of TOF values the enhancement in fuel productivity is noted to be 80 to 300 % higher for Cu NPs in comparison to different results reported in the literature ^[41].

It is also interesting to comment on the significant decrease in the metal loading (from ~ 10 % to ~1-2 %), with better C-products efficiency and in addition to increased H₂ evolution. The steady rate of generation of products is also addressed, which gives insight into the stability

of the catalytic electrode. The equilibrium current ranges in from 2.5 mA to 7.5 mA, which demonstrates that very small current is enough to reduce CO₂ to fuels. This lies well within the range of photo-current generated in photo-catalysis works [42, 43], signifying the feasibility of a full cell photo-electro catalysis.

The most noticeable change observed between the NPs obtained via the OM route and the NPs obtained by the Impregnation route is the decrease in nanoparticle size (from 8-12 nm to 1-3 nm). The substantial drop in size could therefore be, considered a possible explanation for this increased catalytic performances. Attempts to correlate the performance to effective dispersion of the NPs have lead us to conclude that the fraction of surface atoms for smaller NPs is much higher than the bigger NPs, thereby adding to the fuel efficiency. Other effects possibly due to the difference in side products of the two syntheses (possibly connected to the presence of =r not of contaminants depending on the route) and/or difference in sintering phenomena along the reaction have not been investigated and could have an effect on explaining these performance differences between the two routes. One of the outlook of this work could be to address this point more precisely for example by tackling the effect of inorganic salts in the OM route (to address the hypothesis of contaminant effect) or to study the size of the NPs after electrocatalysis (to address the hypothesis of the sintering effect). Regardless the explanation, one concluding point remains clear: the superior performance of the catalysts developed through the OM route, which achieve higher productivity with lower metal loading with respect to analogous classical impregnation route from inorganic salts.

4.5. References

- [1] K. Philippot and B. Chaudret, *C. R. Chimie*, 2003, **6**, 1019–1034.
- [2] K. Pelzer, O. Vidoni, K. Philippot, B. Chaudret and V. Colliere, *Adv. Funct. Mater.*, 2003, **13**, 118-126.
- [3] K. Pelzer, B. Laleu, F. Lefebvre, K. Philippot, B. Chaudret, J. P. Candy, and J. M. Basset, *Chem. Mater.*, 2004, **16**, 4937–4941.
- [4] J. Tang, F. Redl, Y. Zhu, T. Siegrist, L. E. Brus and M. L. Steigerwald, *Nano Lett.*, 2005, **5**, 543-548.
- [5] B. Chaudret; *C.R. Physique*, 2005, **6**, 117.
- [6] O. Margeat, C. Amiens, B. Chaudret, P. Lecante and R. E. Benfield, *Chem. Mat.*, 2005, **17**, 107.

- [7] C. Amiens and B. Chaudret, *Mod. Phys. Lett. B*, 2007, **21**, 1133.
- [8] B. Chaudret and K. Philippot, *Oil & Gas Sci. and Tech.*, 2007, 62, 799-817.
- [9] M. Boualleg, D. Baudouin, J. M. Basset, F. Bayard, J. P. Candy, J. C. Jumas, L. Veyre and C. Thieuleux, *Chem. Commun.*, 2010, **46**, 4722–4724.
- [10] C. Desvaux, F. Dumestre, C. Amiens, M. Respaud, P. Lecante, E. Snoeck, P. Fejes, P. Renaud and B. Chaudret, 2009, *J. Mater. Chem.*, 2009, **19**, 3268-3275.
- [11] D. Baudouin, K. C. Szeto, P. Laurent, A. D. Mallmann, B. Fenet, L. Veyre, U. Rodemerck, C. Coperet, C. Thieuleux, *J. Am. Chem. Soc.*, 2012, **134 (51)**, 20624.
- [12] M. Boualleg, S. Norsic, D. Baudouin, R. Sayah, E.A. Quadrelli, J.-M. Basset, J.-P. Candy, P. Delichere, K. Pelzer, L. Veyre, C. Thieuleux, *Journal of Catalysis*, (2011), **284**, 184–193.
- [13] P. Laurent, L. Veyre, C. Thieuleux, S. Donet, and C. Copéret, *Dalton Trans.*, 2013, **42**, 238-248.
- [14] M. L. M. Bonati, T. M. Douglas, S. Gaemers, N. Guo, *Organometallics*, 2012, **31**, 5243-5251.
- [15] A. Ryzhikov, J. Jonca, M. Kahn, K. Fajerweg, B. Chaudret, A. Chapelle, P. Menini, C.H. Shim, A. Gaudon and P. Fau, *J Nanopart Res*, 2015, **17**, 280.
- [16] M. B. Gawande, A. Goswami, F. X. Felpin and T. Asefa, *Chem. Rev.*, 2016, **116**, 3722–3811.
- [17] R. Reske, H. Mistry, F. Behafarid, B. R. Cuenya, and P. Strasser, *J. Am. Chem. Soc.*, 2014, 136, 6978–6986.
- [18] J. H. Kim, T. A. Germer, G. W. Mulholland and S. H. Ehrman, *Adv. Mater.*, 2002, **14**, 518–521.
- [19] A. A. Ponce and K. J. Klabunde, *J. of Molecular Catalysis A – Chemical*, 2005, **225**, 1–6.
- [20] A. G. Nasibulin, E. I. Kauppinen, D. P. Brown and J. K. Jokiniemi, *J. of Physical Chemistry B*, 2001, **105** , 11067 – 11075 .
- [21] R. M. Tilaki, A. I. Zad and S. M. Mahdavi, *Applied Physics A*, 2007, **88** , 415 – 419.
- [22] G. R. Dey, *Radiation Physics and Chemistry*, 2005, **74**, 172 – 184.
- [23] B. Deng, A. W. Xu, G. Y. Chen, R. Q. Song and L. Chen, *J. of Physical Chemistry B* , 2006, **110**, 11711 – 11716.
- [24] B. J. Murray, Q. Li, J. T. Newberg, E. J. Menke, J. C. Hemminger and R. M. Penner, *Nano Lett.*, 2005, **5**, 2319 – 24.
- [25] I. Haas and A. Gedanken, *Chemistry of Materials*, 2006, **18**, 1184 – 1189.

- [26] Y. Chang, M.L. Lye and H. C. Zeng, *Langmuir*, 2005, **21**, 3746 – 3748.
- [27] P. Kanninen, C. Johans, J. Merta and K. Kontturi, *Journal of Colloid and Interface Science*, 2008, **318**, 88 – 95.
- [28] A. A. Athawale, P. P. Katre and M. B. Majumdar, *J. of Nanoscience and Nanotechnology*, 2005, **5**, 991 – 993.
- [29] C. Salzemann, I. Lisiecki, A. Brioude, J. Urban and M.P. Pileni, *The Journal of Physical Chemistry B*, 2004, **108**, 13242 – 13248.
- [30] N. Cioffi, N. Ditaranto, L. Torsi and L. Sabbatini, *Approaches to Synthesis and Characterization of Spherical and Anisotropic Copper Nanomaterials. Nanotechnologies for the Life Sciences*, 2010.
- [31] S. Stopić, P. Dvorak, and B. Friedrich, *World of Metallurgy – Erzmetal*, 2005, **58**, 4.
- [32] C. Mayousse, C. Celle, A. Carella. and J. P. Simonato, *Nano Res.*, 2014, **7**, 315-326
- [33] S. Li, Y. Chen, L. Huang and D. Pan, *Inorg. Chem.*, 2014, **53**, 4440–4444.
- [34] D. Nunes, A. Pimentel, P. Barquinha, P. A. Carvalho, E. Fortunato and R. Martins, *J. Mater. Chem. C*, 2014, **2**, 6097–6103.
- [35] I.E. Stewart, A. R. Rathmell, L. Yan, S. Ye, P. F. Flowers, W. You and B. J. Wiley, *Nanoscale*, 2014, **6**, 5980-5988.
- [36] T. Gao, G. Meng, Y. Wang, S. Sun and L. Zhang, *J. Phys.: Condens. Matter*, 2002, **14**, 355-363.
- [37] F. J. Owens, C. P. Poole Jr., “The Physics and Chemistry of Nanosolids”, John Wiley and sons, Inc. publication, 2008.
- [38] A. K. Singh, “Engineering Nanoparticles: Structure, Properties and Mechanisms of Toxicity”, Academic Press, 2015
- [39] E. M. Savitskiĭ, “Handbook of Precious Metals”, Hemisphere publishers, 1989.
- [40] H. Mistry, R. Reske, Z. Zeng, Z. Zhao, J. Greeley, P. Strasser, and B. R. Cuenya, *J. Am. Chem. Soc.*, 2014, **136** (47), 16473-16476.
- [41] K.P. Kuhl, E.R. Cave, D.N. Abram, T.F. Jaramillo, *Energy & Environ. Sci.*, 2012, **5**, 7050.
- [42] C. Ampelli, G. Centi, R. Passalacqua and S. Perathoner, *Catal. Today*, 2016, **259**, 246-258.
- [43] C. Ampelli, C. Genovese, F. Tavella, M. Favaro, S. Agnoli, G. Granozzi, S. Perathoner and G. Centi, *Chem. Engg. Trans.*, 2015, **43**, 667-672.

Materials and Reagents

Chemicals used in our synthesis route are Iron (III) nitrate nonahydrate [Fe(NO₃)₃·9H₂O], Iron (III) acetyl acetonate [Fe(C₂H₇O₂)₃ or Fe(acac)₃], chloroplatinic acid hexahydrate [H₂PtCl₆·6H₂O], Bis(dibenzylidene acetone) Platinum [Pt(dba)₂], (1,5-cyclooctadiene)(1,3,5-cyclooctatriene) Ruthenium [C₁₆H₂₂Ru], Ruthenium Chloride hydrate (RuCl₃·xH₂O), nitric acid (HNO₃, 65%), sulphuric acid (H₂SO₄, 95%), absolute ethanol (98 %), potassium bicarbonate (KHCO₃, 99.7%), Nafion perfluorinated resin were obtained from Sigma-Aldrich and used without any further purification. Solvents hexane, toluene, tetrahydrofuran (THF) were obtained from Carlo-Erba reagents and were dried and distilled before use. Commercial carbon nanotubes (CNTs, PR-24-XT-PS) were bought from Pyrograf® and were pre-treated before use. Gas Diffusion layer (GDL 25 BC) was obtained from Sigracet®. Nafion membrane (Nafion¹¹⁷) was obtained from Ion power and was pre-treated before use.

Characterization Tools:

X-Ray Diffraction (XRD):

XRD was performed to determine the crystal structure of the catalysts using a D2 Phaser Bruker diffractometer equipped with a Cu-K α radiation (1.5406 Å) source operating at 30 kV and 10 mA. A scan rate of 0.025°/s with a 2 θ range in 12° to 100° was used for data collection.

High Resolution Transmission Electron Microscopy (HRTEM):

HRTEM was used to understand the structural and morphological characteristics of the catalysts by using a MET JEOL 2100FEF (field effect gun energy filtering) microscope at the “Centre Technologiques des Microstructures”, CT μ Villeurbanne, France; equipped with an energy-dispersive x-ray (EDX) analyser.

X-Ray photoelectron spectra (XPS):

Quantitative surface analysis was performed by XPS using PHI 5000 VersaProbe II spectrometer with a monochromatic Al-K α X-ray source operated at 100 W, 20 kV.

Brunauer-Emmett-Teller (BET):

BET surface area and porosity of the catalytic material were analysed by N₂ adsorption/desorption at 77 K using an ASAS 2020 Micromeritics system. To degas the samples, a pre-treatment was performed at 10⁻⁴ Pa, 150 °C for 2 Hr.

Atomic absorption spectroscopy (AAS):

The amount of metal loading on the CNT substrate in the catalyst was determined using a Perkin-Elmer AAnalyst 200, atomic absorption spectrometer.

N₂ adsorption-desorption isotherms:

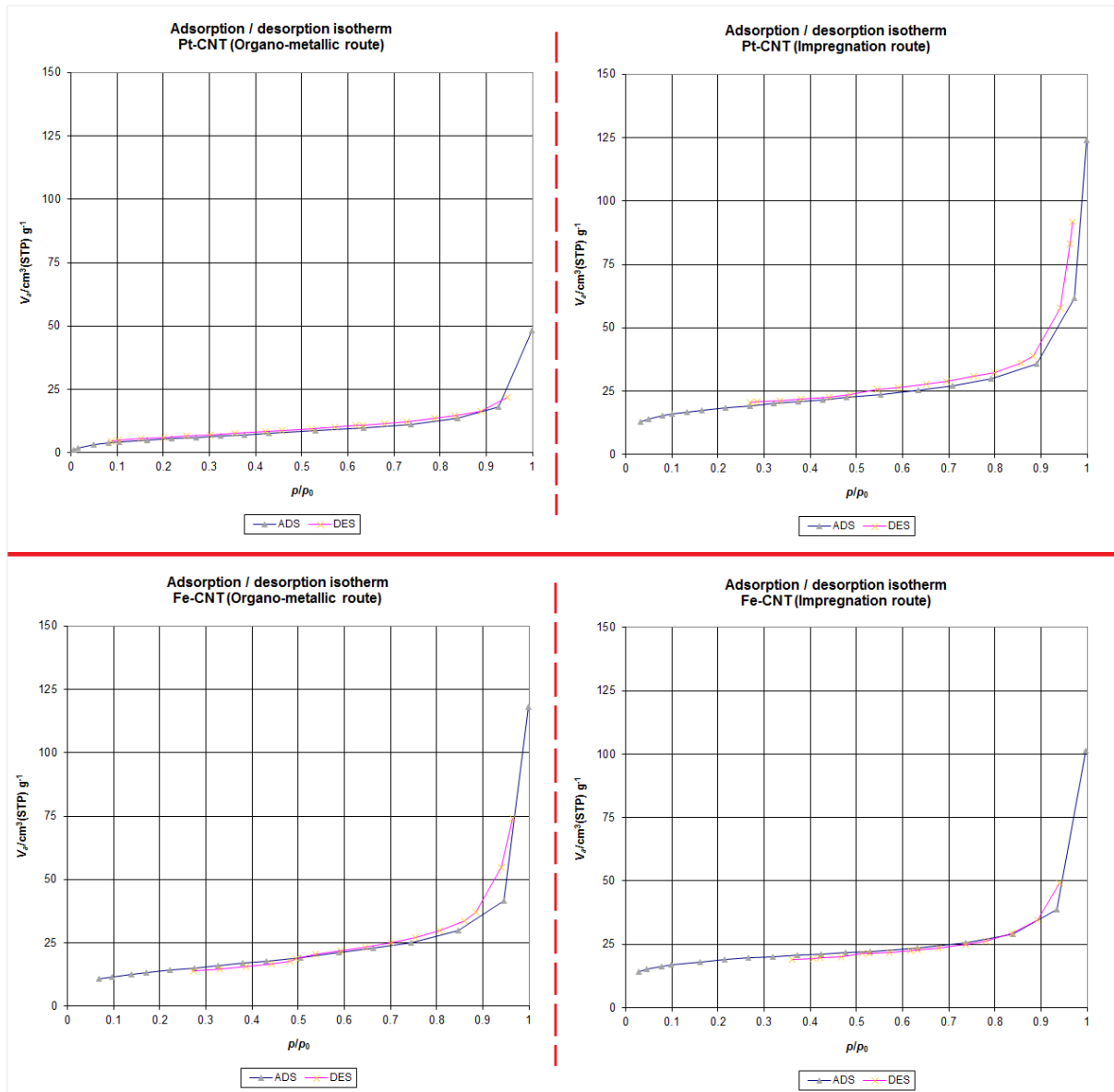


Fig. 4.20 N₂ adsorption/desorption isotherms for Pt, Fe, NPs on CNT_{ox} (OM & ImR routes).

CHAPTER 5

Nano foams for liquid phase CO₂ electro-reduction

5.1 Introduction

5.1.1. State of the art

The foam is a type of material with trapped pockets of gas. The trapped voids can be interconnected (open-cell foam, e.g. bath sponge) or independent due to fully covered by material (closed-cell foam, e.g. camping mat). If the void dimensions are in the range of a few microns to 10's of nanometers, then they are termed as nano-foams. Foams are century old material systems [1, 2]. In nature intricate nano-foam materials existed from ages, e.g. bones. Nano foams include aerogels [3-11], carbon nano-foams [12-14], metal nano-foams [15-20], etc. Cu metal nano-foams are studied from more than a decade with keen focus on the aspects of tuning the nano-foams physical and structural properties [21]. However, on application of copper nano-foams to CO₂ reduction, only a few recent studies exist [22, 23].

The state of the art fuel productivity achieved using different metal electrodes, macro metal foams and combination of metals with nano-foams are shown in *Table 5.1*. These results show high faradaic efficiency for specific products, however, the voltage applied, the current density and the electrolytes solution used have to be considered while understanding these results. Sn and Cu seem to be good candidates for CO₂ reduction and show promising results. Nano-foams can be better alternative to look into as a replacement for pure metal electrodes. High purity metals are quite costly and nano-foams can be a cheaper alternative with high fuel productivity and in addition foams hold a large catalytic area for a given geometrical area.

Table 5.1 A review of the results of CO₂ electro-reduction using metals and foams catalysts.

Electrodes	E vs. NHE (V)	Major Products	Faradaic Efficiency (%)	Current Density (mA cm ⁻²)	Reference	Electrolyte
SnO ₂ on Sn	- 1.8	HCOO ⁻	85	5.5	[24]	2.5 M KHCO ₃
Cu-In bimetallic	- 0.7	HCOOH, CO	85	1.8	[25]	0.1 M KHCO ₃
Sn on Cu Foam	- 1.8	HCOO ⁻	83.5	11	[26]	2.5 M KHCO ₃
Cu nanofoam	- 1.5	HCOOH	37	100	[22]	0.5 M K ₂ SO ₄
Sn nanofoam	- 1.8	HCOOH	91.5	6	[27]	2.5 M KHCO ₃
Cu Foil	- 1.2	CH ₄ , CO	40	10	[28], [29]	0.1 M KHCO ₃

5.1.2. Electro-chemical deposition

The electro-chemical deposition is a century old technique for creating thin metallic, oxide, inorganic or organic coating or film on a conducting or semi-conducting substrate. The motive behind the deposition can be to protect the surface, decorate (colour or lustre), create reflective or magnetic or frictionless or conductive surface, etc. This process attains micro to nano scale thin films, thus the process follows micro/nano-manufacturing. The deposition is performed using a metal ion or its chemical complex solution. The basic concept behind this process is the oxidation of metal ions either of the anode or already present in the electrolytic solution and finally getting reduced on the cathode on application of positive direct voltage or current to the anode as shown in *Fig. 5.1*. Various factors can be varied during the deposition such as temperature, P^H , sonication, pressure, signal functions, time, stabilizers, ion charge, potential, etc., to tune the structural and physical properties of the deposited films. In literature, there are many studies specific to these conditions to achieve the desired end product. Some of them lead to the formation of metal oxide nano-foams (NFs) on specific substrates [30-32].

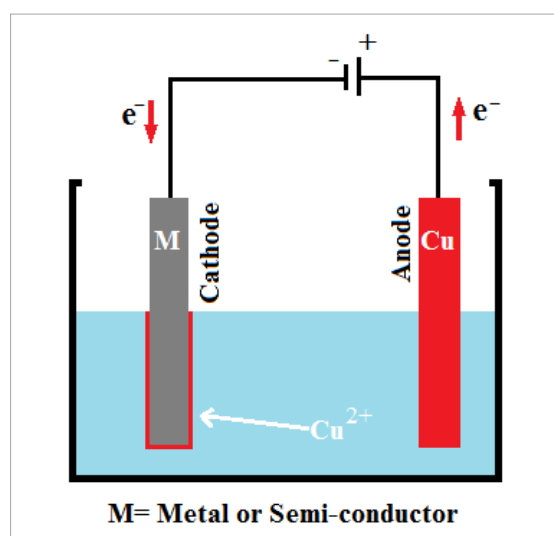


Fig. 5.1 Schematic showing Electro-deposition of Cu on metal/semi-conductor.

5.1.3. Scope of the chapter

This chapter is dedicated towards the understanding of the simple synthesis routes to nano foams for various metals as well as on various substrates and their catalytic activity on the CO₂ electro-reduction to fuels. To accomplish this, first we needed to synthesize metal NFs using simple electro-deposition technique. Cu, Fe NFs were formed on various substrates which include Cu, Fe, Al, Inconel (Ni-Cr-Fe alloy), Al grid, etc. Metal oxide based dendrite like

structures were formed on these substrates with varying structural and catalytic properties. The nano-foam deposited on the metal substrates formed the working electrode and were tested for their catalytic performance on CO₂ reduction in the liquid phase cell (discussed in [Chapter 3](#)).

5.2 Experimental

5.2.1. Synthesis of metal nano-foams via electro-chemical deposition

A nano-foam is a porous nano-structure material with nano-scale pores or voids. Metal nano-foams can be achieved using specific combination of deposition ions and their substrate counter parts. Electro-deposition of Cu ions onto Cu or Fe or Al or Inconel cathode forms different kinds of foamy structures which are mostly dendrite like porous structures as show in schematic [Fig. 5.2](#). In the similar lines, Fe foams can be formed on Fe, Al, and Inconel cathodes.

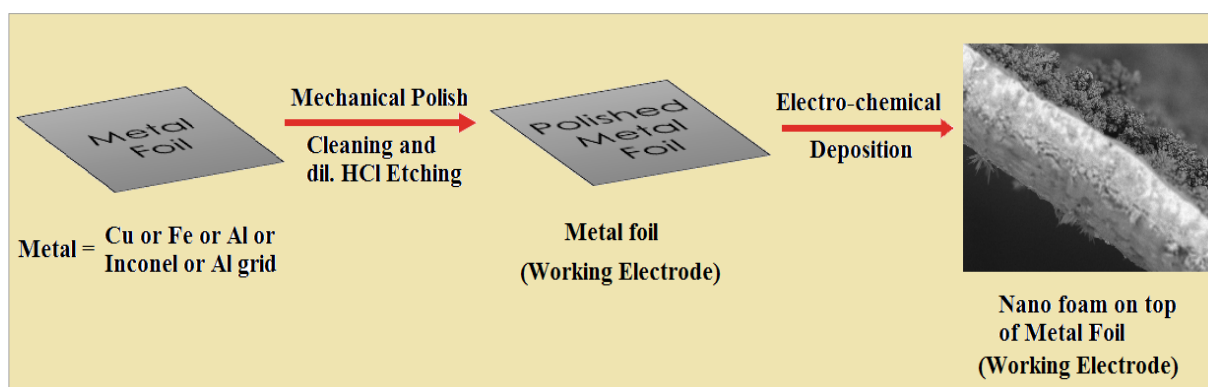


Fig. 5.2 Schematic of the Electro-deposition of metal to nano-foam electrodes.

5.2.1.1. Cu nano-foam synthesis

The Cu thin film is used as the anode and for the cathode different materials were experimented, which include Cu Foil, Fe foil, Al foil, Inconel foil and Al grid. Both the anode and cathode materials were initially pre-treated by mechanical polishing followed by cleaning with acetone and etching with aqueous dil. HCl solution. A fixed separation distance of 2 cm between anode and cathode was maintained. A 40 ml of aqueous electrolytic solution containing 0.4 M CuSO₄ or 0.4 M Cu(acetate)₂ and 1.5 M H₂SO₄ mixed with 0.2 M acetic acid and 50 mM HCl was used for the electro-deposition. These specific conditions were obtained from the well-established study on Cu NFs ^[33].

A positive current of 1.2 A is applied for various time periods (1, 2 and 4 min) to understand the formation and stability of the nano-foam based catalytic electrode. The initial experiments were started with Cu foil acting as both anode and cathode for different time periods for electro-deposition. The thus, formed Cu NFs were calcined at 150 °C for 2 hr. For time periods of 1 and 2 min, the nano-foams remained stable and robust, while the 4 min nano-foam was brittle and fragile. These three Cu NFs on Cu foil electrodes were tested for their CO₂ reduction capabilities to optimize the time period of deposition.

From here on, all the depositions were performed for time = 2 min. The Cu NF was formed on Fe, Al, Inconel foils and Al grid using this time of deposition. The NFs were characterized using SEM, XRD and XPS. Cu NF on Al grid was used together by physical attachment with Cu NF on Cu, to form a mixed electrode. Cu NF on Al grid alone was not used as the sample (being a grid) could not seal the liquid phase cell compartment.

However, one sample of Cu NF on Fe cathode was prepared using under-potential deposition, with deposition time of 15 min. This technique does not involve application of current, but it utilizes the reduction potential difference between the Cu and Fe metals to its advantage and deposit Cu foam on Fe foil.

5.2.1.2. Fe nano-foam synthesis

The Fe thin film is used as the anode and for the cathode different materials were experimented which include Fe foil, Al foil, Inconel foil, Al grid. Cu foil cannot work as cathode in this case as the reduction potential of Cu is quite higher than Fe.

Same pre-treatments, conditions such as the distance between electrodes, the current applied and the time of 2 min were used. A 40 ml of aqueous electrolytic solution containing 0.4 M FeSO₄ or 0.4 M Fe(NO₃)₃ and 1 M H₂SO₄ mixed with 0.2 M acetic acid and 50 mM HCl was used for the electro-deposition. After the electro-deposition for 2 min at 1.2 A, the as-formed Fe NFs were calcined at 200 °C for 2 hr. The Fe NFs were found to be not as flexible as Cu NF as they were quite brittle and peeling-off. The CO₂ reduction activity of these three Fe NF based electrodes were tested in the liquid phase cell.

5.2.1.3. Metal foils

Metal foils of Cu, Fe, Al and Inconel were pre-treated by mechanical polishing followed by cleaning with acetone and etching with aqueous dil. HCl solution. Since, nano-foams foams were formed on metals, it can be supposed that their activity might be partly due to the base substrate. Thus, these plain metallic electrodes were tested separately in the electro-catalytic reduction of CO₂ to fuels. In order to have a better comparison and understanding for the nano-foams fuel productivity data.

5.3 Results and Discussions

5.3.1. Characterization

The nano-foams were characterized using different techniques to determine the physical and structural properties. These include SEM, XPS, XRD, EDX and current profiles.

5.3.1.1. SEM Morphological Measurements

Scanning Electron Microscopy (SEM) was used to understand the structural and morphological surface characteristics of the nano-foams. *Fig. 5.3 (a) & (b)*, shows the surface with Cu foamy structures formed on Cu foil with deposition time = 1 min and 4 min, respectively. In the former figure, it can be observed that dendrite structures are yet to be formed, while in the later a flake-like structure formed bulk up into flakes due to increased time of deposition of the dendrites.

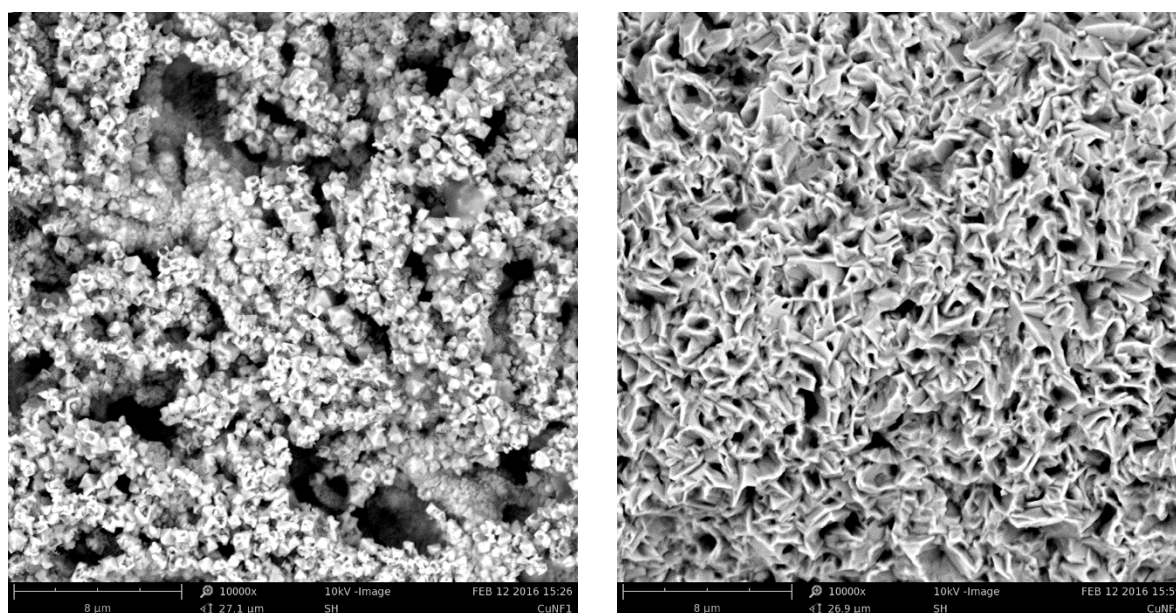


Fig. 5.3 SEM image (top view) of the Cu NF on Cu foil with deposition time (a) 1 min, (b) 4 min.

Fig. 5.4 shows the top view of the Cu foamy structures formed on Cu foil with deposition time = 2 min. *Fig. 5.5 (a) & (b)*, give a closer view of the Cu dendritic structures formed on the Cu foil, for deposition time of 2 min. The dendrites resemble a leaf like model, with each leaf edge branching out into more leaves. The smallest edge measures about 100 nm. The leaf branches measure about 3, 5, 8 μm and the maximum about 13 μm before it collapses due to the increasing weight. The leaf branching approximately follows a Fibonacci sequence. Moreover, holey areas can be observed, which are formed due to the H_2 bubbles pushing out of the foamy structures formed during the electro-deposition. If higher current is applied, a porous foam tube like system can be achieved as shown in the literature [33].

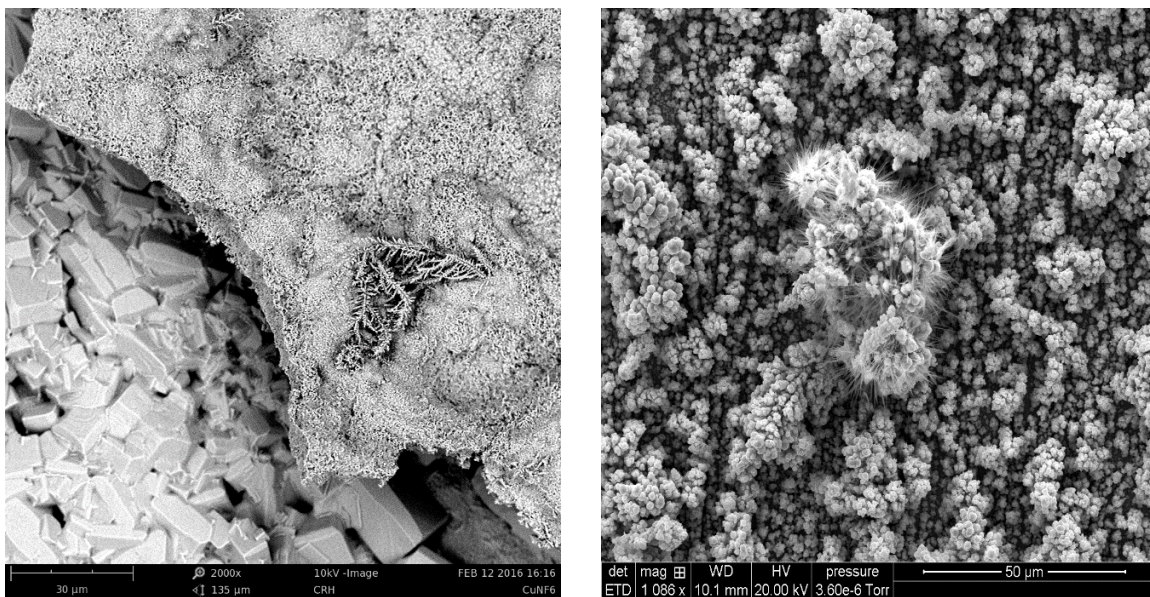


Fig. 5.4 SEM images (top view) of the Cu NF on Cu metal foil with deposition time = 2 min.

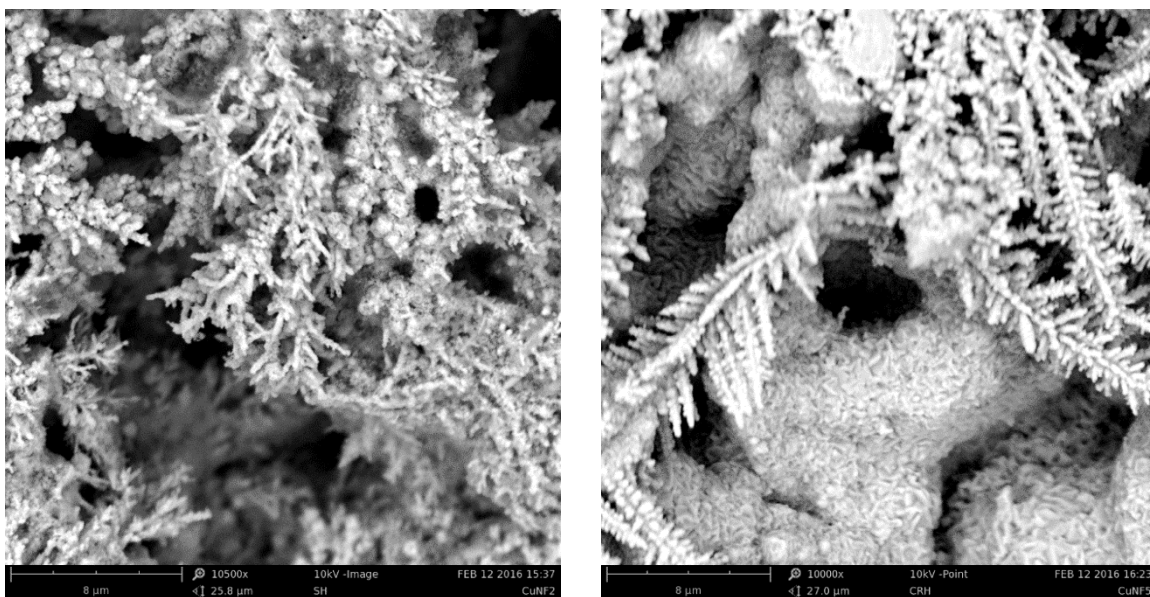


Fig. 5.5 SEM images of Cu NF on Cu (2 min) - dendrite structures.

Fig. 5.6 shows the cross-sectional view of the nano-foams, evidencing a thickness of the Cu foam ranging between about 15-20 μm . *Fig. 5.7* shows the thick leaf-like Cu foams formed on Fe metal foil as the base substrate. It can be observed that these dendrites are more compact and closely packed as compared to that of the Cu foil based foams. Moreover, the lengths of these systems ranged from 100 nm to 100 μm . Since the thickness and length are very high, they collapse under their own shear weight and form a dense intricate structure.

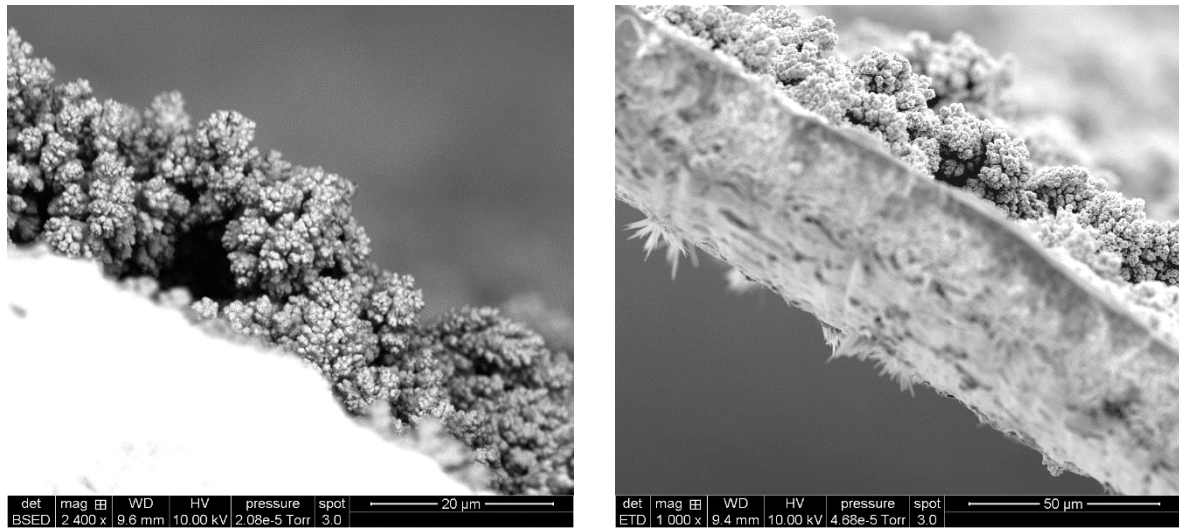


Fig. 5.6 SEM images (cross-section view) of Cu NF on Cu (2 min).

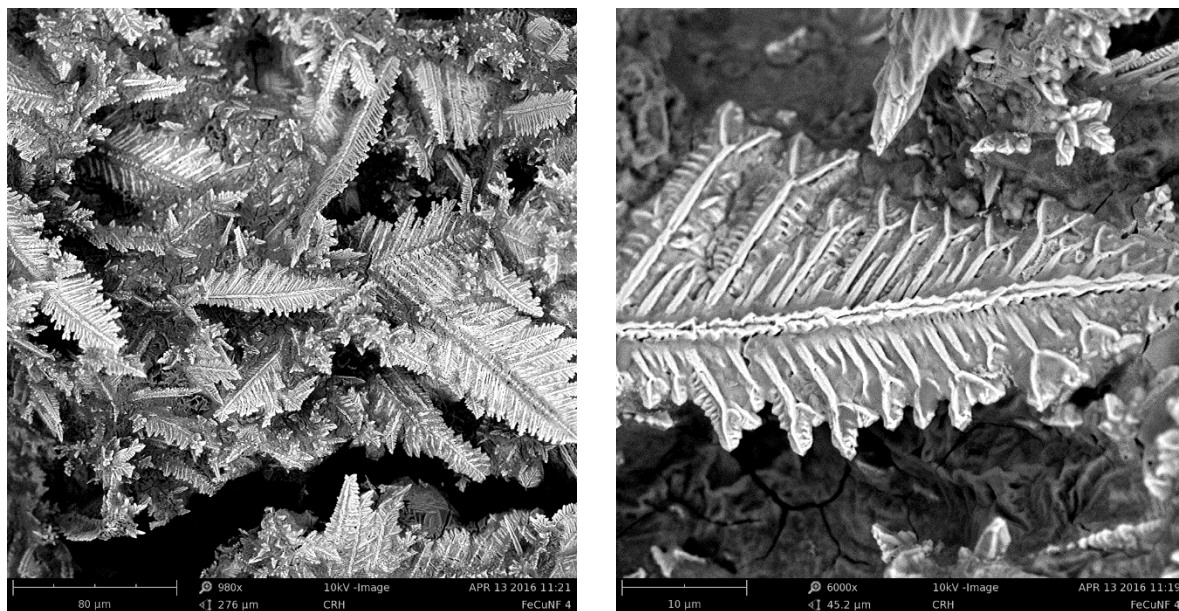


Fig. 5.7 SEM images of Cu NF on Fe foil (2 min) (a) top view, (b) dendrite close-up.

The best electrode was the two-minute nano-foam sample in terms of structure as seen from the EM images and fuel productivity tests which showed Cu NF (2 min) yielded 3 times and 5 times higher fuel productivity than Cu NF (4 min and 1 min), respectively.

Fig. 5.8 shows the Cu foam formed on an Al grid as base substrate. The foam is compact and thick. Not many dendrites are seen for Al as the base. In addition, from the cross-sectional view, we can calculate the thickness of the foam, which is about 4-5 μm . Increasing the deposition time would make the foam peel-off since the base is cylindrical, thereby it has additional bending forces. *Fig. 5.9* shows the Fe foam formed on Al base substrate. The Fe foams do not have dendrite like structure unlike Cu and are about 5 μm thick.

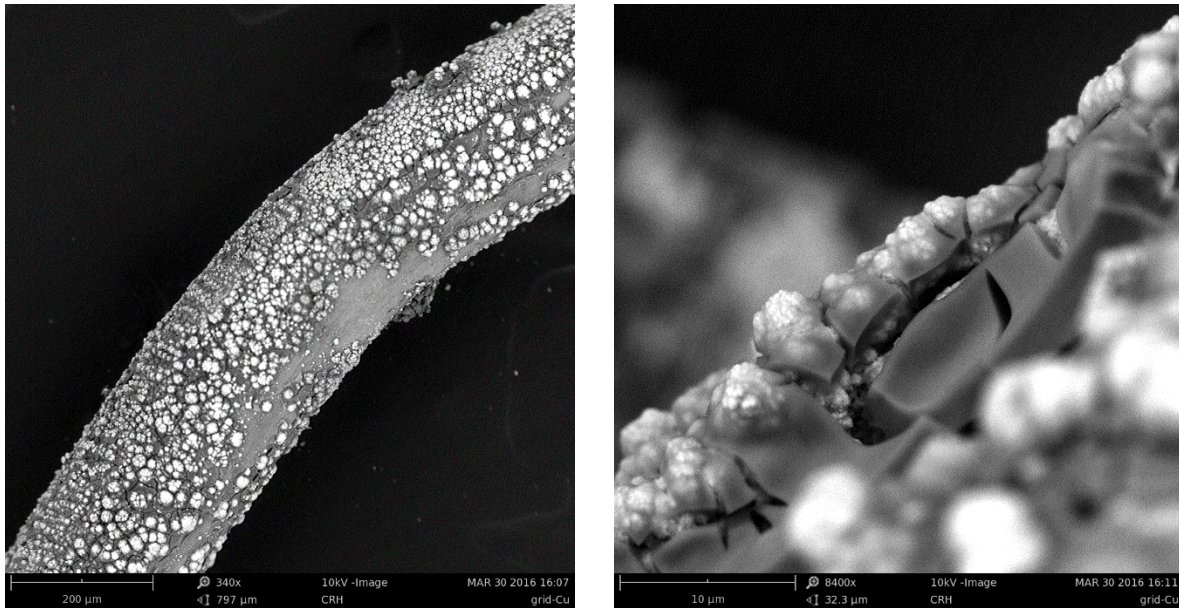


Fig. 5.8 SEM images of Cu NF on Al grid (2 min) (a) top view, (b) cross-section view.

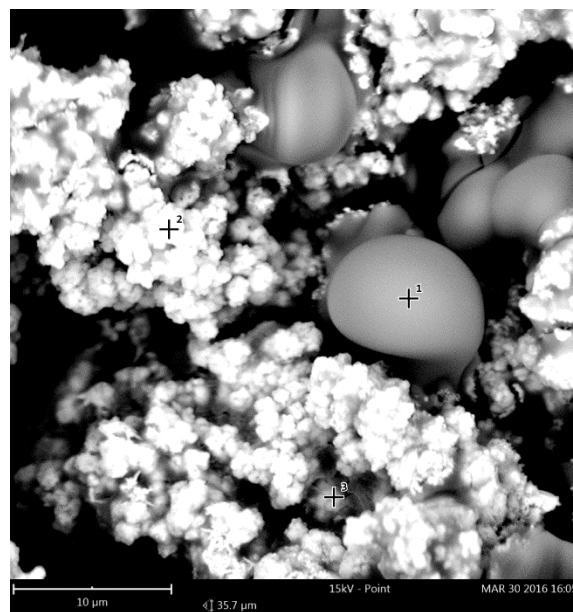


Fig. 5.9 SEM image of Fe NF on Al foil (deposition time = 2 min).

5.3.1.2. Surface Analysis

A quantitative surface analysis was performed by X-Ray photoelectron spectroscopy (XPS). The survey gives an insight into the oxidation state of the Cu foam formed. The C-1s binding energy of adventitious carbon (284.9) was used as the reference. *Fig. 5.10 (a)* gives the general survey spectra of the Cu nano-foam, while *(b)* shows a high-resolution spectrum evidencing the peaks at 932.3 eV and 952.1 eV. They represent the characteristic binding energies for the CuO species, which are further confirmed by satellite peaks at 942.5 eV and 962.6 eV.

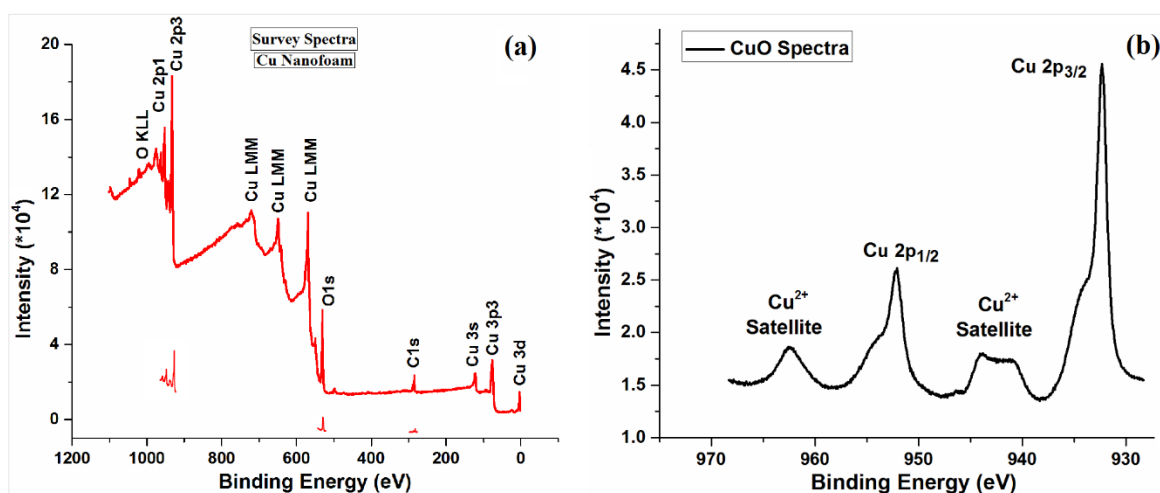


Fig. 5.10 (a) XPS wide scan survey spectra for Cu nano-foam on Cu (b) High-resolution spectrum of the Cu 2p doublets.

5.3.1.3. Structural Analysis

X-Ray Diffraction (XRD) was performed to determine the crystal structure of the nano-foam. *Fig. 5.11* shows the XRD patterns for Cu NF on Cu foil. From the diffraction pattern, the 3 peaks at $2\theta = 43.54^\circ$, 50.61° , and 74.25° , corresponding to the planes (111), (200) (220), respectively of the FCC of Cu metal. Also, 2 peaks are observed at $2\theta = 36.76^\circ$ and 58.64° , which may correspond to CuO formed.

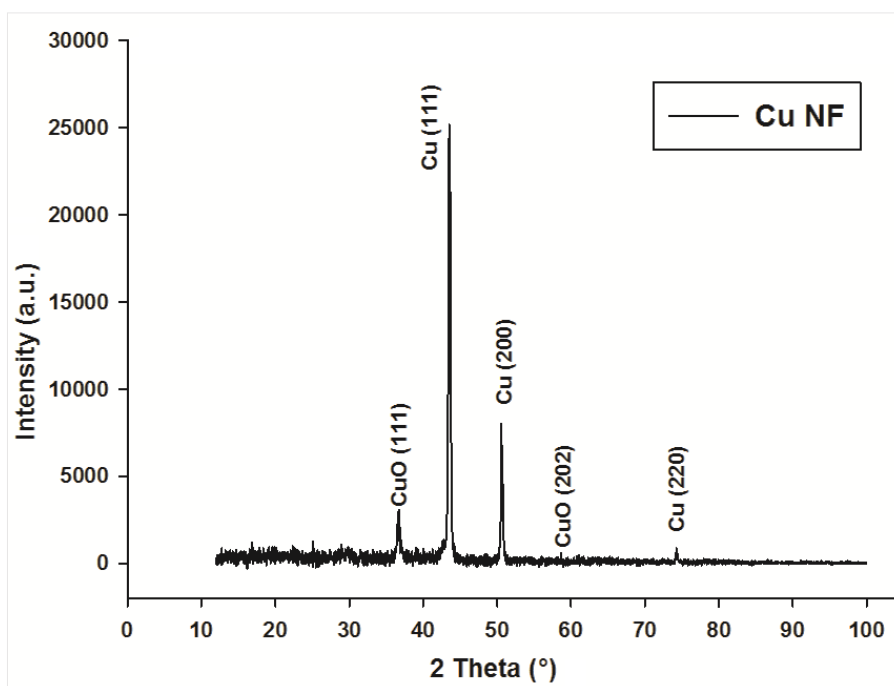


Fig. 5.11 XRD pattern of the Cu nano-foam with base substrate as Cu foil.

5.3.1.4. Energy Dispersive X-ray spectroscopy (EDX)

EDX was carried out on different nano-foam samples, to get an idea of the composition of the different elements present. *Fig. 5.12* shows the EDX spectra for Cu nano-foam on Cu foil, and the respective atomic concentrations are Cu (76.4 %), O (22.6 %), C (1%). Other samples EDX are discussed in the *annex⁵*.

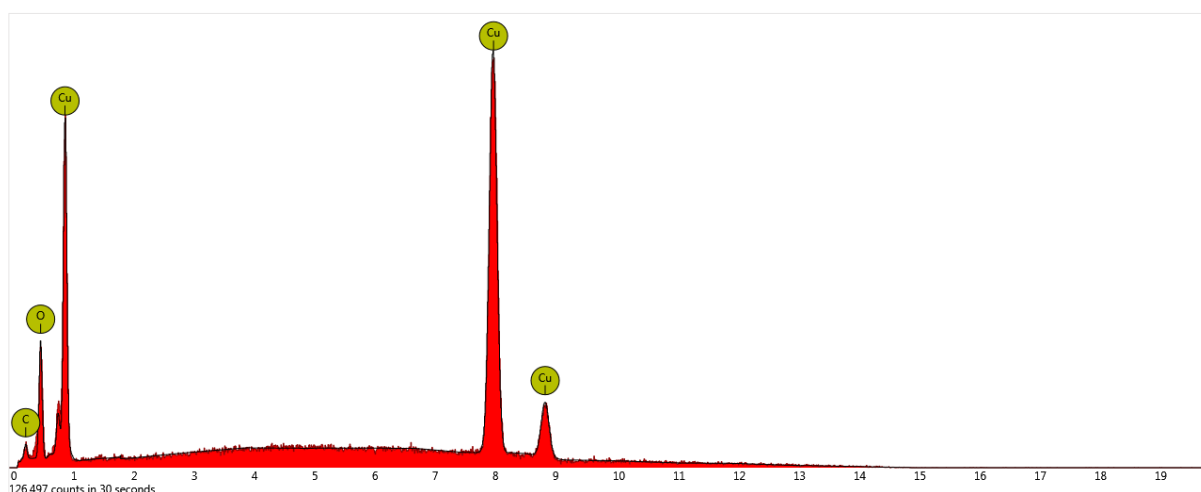


Fig. 5.12 EDX spectra of the Cu nano-foam with base substrate as Cu foil.

5.3.1.5. Quantitative discussion

From the SEM surface and cross-sectional views, considering for the Cu nano-foam on Cu foil case, the foam can be approximated as layers of leaf-like structures and the porosity to be around 30 %, calculated assuming the individual structures repeat themselves in the entire foam. The weight of the foam can be calculated using density and volume (considering 15 μm thickness) to be about 53 mg. The actual weight measured by peeling of the nano-foam from the metal base was about 25-30 mg, indicating the high porosity of the nano-foam.

5.3.1.6. Electro-catalytic CO₂ reduction

5.3.1.6.1. Current profile

The current profiles (in amperes) for the CO₂ reduction reactions, for the different Cu NFs on different base substrates and Cu Foil as a reference are shown below in [Fig. 5.13](#). A constant potential of -1.5 V is applied to the cell. It can be observed that the currents at the beginning of the reaction is quite high and then stabilize as an equilibrium P^H is achieved in the electrolytes in the anodic and cathodic compartments. Although the initial currents vary from 0.1 to 0.5 A, the equilibrium current lies in the range of 5 mA to 20 mA.

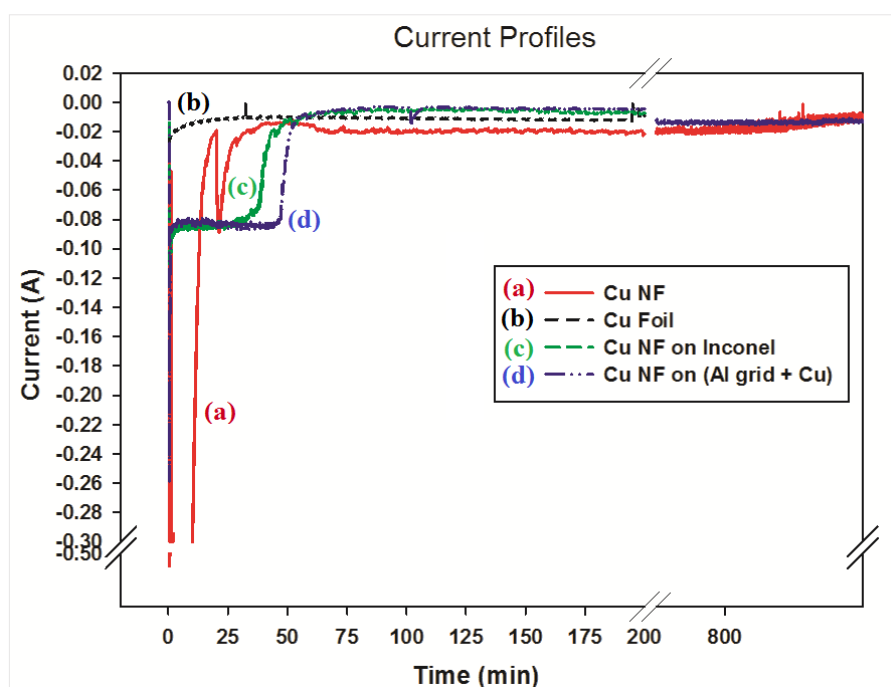


Fig. 5.13 Current profiles for (a) Cu NF on Cu, (b) Cu Foil, (c) Cu NF on Inconel, (d) Cu NF on (Al grid + Cu foil).

5.3.1.6.2. Voltage Optimization

CO₂ reduction studies were conducted using Cu foil as the working electrode and then varying the voltage to find an optimum potential needed to increase the fuel productivity. The different voltages at which experimented were performed: -0.5V, -1V, -1.4V, -1.5V, -1.6V and -2V. The fuel productivity results for major products are shown in the *Table 5.2*. From these results, the potential = -1.5 V, was chosen as the common potential applied for all other nano-foam electrodes and the average current lies around 10 mA. Note that the productivity for - 1.6 V is slightly higher but the current used is almost double (i.e. energy used is double).

Table 5.2 Productivity for the CO₂ electro-chemical reduction in liquid phase cell for Cu foil electrodes for different voltages (Units: $\mu\text{moles per hr}$).

Voltage, V (pure Cu Foil)	Avg. Current (mA)	FUELS ($\mu\text{mol}\cdot\text{hr}^{-1}$)					
		<i>Formic Acid</i>	<i>Acetic Acid</i>	<i>CH₄</i>	<i>CO</i>	<i>H₂</i>	<i>C-Products (NET)</i>
-0.5 V	0.02	0.162	0.102	-	-	-	0.264
-1.0 V	0.15	0.152	0.000	-	-	1.94	0.152
-1.4 V	13.56	8.959	0.000	2.39	-	391.00	11.349
-1.5 V	11.29	12.477	0.000	2.07	2.80	264.52	17.347
-1.6 V	19.27	23.085	0.000	-	-	15.67	23.085
-2.0 V	20.23	7.869	0.069	-	-	133.76	7.938

5.3.1.6.3. Fuel productivity

The fuels produced during the electro-chemical reduction of CO₂ were analysed using various techniques, which include IC, GC-Mass, and GC-TCD. The major liquid products detected in the liquid electrolyte on the cathode side were formic acid, methanol and acetic acid. Minor quantities of acetone, isopropanol and ethanol were also found. GC-TCD was used to detect gaseous products (H₂, CH₄ and CO). The results are expressed in micromoles of the products obtained for a given time of the reaction and the experiments were performed under same conditions, with potentiostatic conditions (- 1.5 V), and constant CO₂ flow rate of 10 ml/min and the catalytic surface area ~ 5.7 cm².

The fuel productivity values for the nano-foam electrodes synthesized via electro-chemical deposition and the respective plain metal electrodes (which acted as the base substrate for the foams) are shown in *Table 5.2*. It is clearly evident from the *Table 5.3*, for the nano-foams the productivity of C-products increased by several factors for different combinations of metal foams on metal substrates as compared to that of plain metal foil electrodes. The plain metals show near inert activity expect for Cu for the CO₂ reduction to fuels. In addition, there is a huge amount of H₂ production for the nano-foams (several orders higher than metals). The highest productivity obtained was for a combination of Cu nano-foam on Al grid with Cu nano-foam on Cu foil which produced about 44.8 μmol/hr C-products (i.e. 314 μmol/hr.cm² per gm of catalyst) and also, a close value of 44.6 μmol/hr for Cu NF on Inconel foil.

Table 5.3 Productivity for the CO₂ electro-chemical reduction in liquid phase cell for nano-foam electrodes (Units: μmoles per hr).

CATALYSTS (Foam on metal / metal foil)	FUELS (μmol·hr ⁻¹)									
	<i>Formic Acid</i>	<i>Acetic Acid</i>	<i>Methanol</i>	<i>Acetone</i>	<i>Iso- Propanol</i>	<i>Ethanol</i>	<i>CH₄</i>	<i>CO</i>	<i>H₂</i>	<i>C-Products (NET)</i>
Metals										
<i>Cu Foil</i>	12.477	0.060	0.366	0.007	0.010	0.015	2.07	2.80	264.52	17.745
<i>Inconel Foil</i>	0.120	0.000	-	-	-	-	-	-	22.83	0.120
<i>Al Foil</i>	0.580	0.000	-	-	-	-	-	-	89.28	0.580
<i>Fe Foil</i>	0.160	0.000	-	-	-	-	-	-	57.20	0.160
Nanofoam (NF)										
<i>Cu NF on Cu (1 min)</i>	1.960	0.070	0.000	0.001	0.000	0.003	-	-	97.82	2.029
<i>Cu NF on Cu (2 min)</i>	7.870	0.280	0.034	0.001	0.063	0.046	2.24	11.52	1069.55	22.054
<i>Cu NF on Cu (4 min)</i>	6.160	0.140	0.025	0.001	0.000	0.016	-	-	340.90	6.345
<i>Cu NF on Inc.*</i>	23.602	0.255	0.835	0.006	0.000	0.008	-	19.90	777.86	44.606
<i>Cu NF on Al</i>	11.033	6.434	0.286	0.005	0.002	0.005	-	3.30	226.58	21.065
<i>Cu NF on Fe**</i>	0.160	0.420	0.376	0.000	0.000	0.000	2.25	2.13	61.58	5.336
<i>Fe NF on Inc.</i>	5.310	0.630	0.624	0.000	0.007	0.019	-	-	1538.04	6.590
<i>Fe NF on Al</i>	0.360	0.820	0.070	0.000	0.000	0.000	-	-	480.27	1.250
<i>Cu NF on (Al grid+Cu Foil)***</i>	37.190	2.520	1.446	0.008	0.002	0.014	-	3.62	62.17	44.800

* Inc. – Inconel foil ; ** Cu NF on Fe electrode prepared using under potential ; *** Combo-electrode Cu NF on (Al grid + Cu foil)

It can be noticed that the nano-foam bases electrodes show better productivity of oxygenates and hydrocarbons with higher chain (C2-C3) as compared to plain metal electrodes. Higher amounts of C-products along with higher H₂ values indicate that the nano-foam electrodes use the energy supplied with more efficiently. Moreover, there are gaseous products (CH₄, CO) evolved for nano-foams, which were not seen for pure metal foil electrodes. The foams are synthesized via a simple technique and in some cases without application of electricity using only the reduction potential differences of metals, thereby this system can be easily scalable for mass production of foams.

A time dependent study conducted on the products formed is shown in *Fig. 5.14 (a) & (b)*, for two samples – Cu NF on Inconel foil and (Cu NF on Al grid + Cu NF on Cu foil). For these samples, the formation of H₂ and C-products increase with time.

The reaction run-time was increased from 4 hr to 20 hr and also, the working electrodes were reused, to see if there is a significant loss in the catalytic activity. The fuel productivity values were found to be constantly increasing with time and also, the re-use of the electrodes (2 times) showed similar results indicating the stability of the nano-foam electrodes.

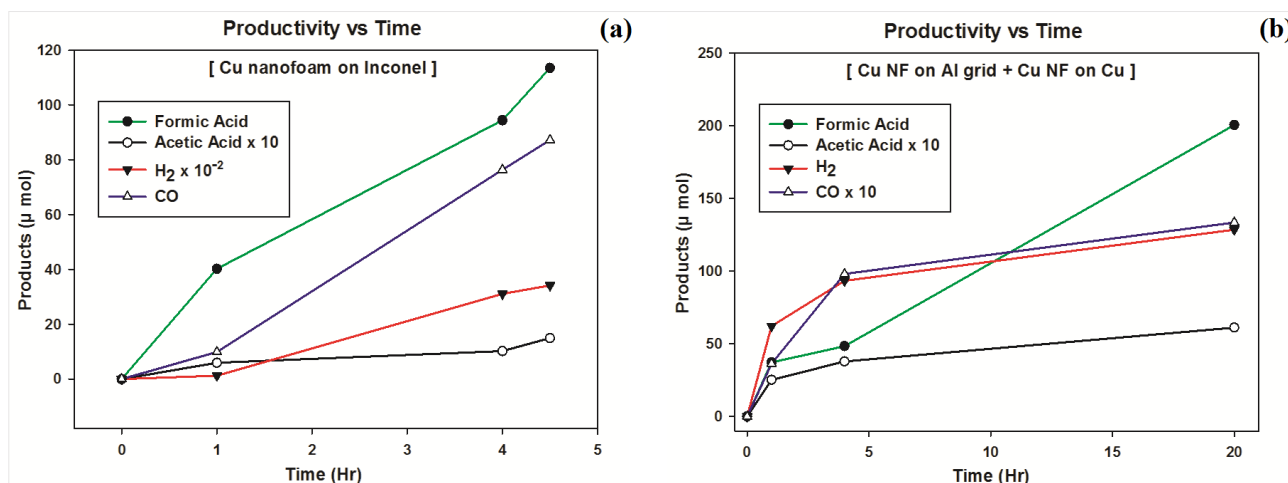


Fig. 5.14 Time dependence vs productivity of formic acid, acetic acid, CO and H₂ for (a) Cu NF on Inconel, (b) Cu NF on Al grid + Cu NF on Cu foil.

5.4 Conclusions

A simple electro-chemical deposition technique was used for developing nano-foams of Cu and Fe on various base substrates (Cu, Fe, Inconel, Al, Al grid). Dendrite like structured nano-foams were successfully formed. Various deposition times were experimented to understand the nano-foams strength and stability.

An elaborate study on the nano-foam based electrodes for Electro-catalytic CO₂ reduction is presented. The various products detected in the liquid phase and the selectivity towards different products have been discussed. Also, the base substrate metals were individually tested for electro-catalytic CO₂ reduction. And except for Cu, rest all base metals (Fe, Inconel, Al, Al grid) showed near inert activity towards CO₂ reduction. A voltage optimization study was also performed.

The fuel productivity values were several factors higher than simple metallic electrodes. The factors ranged from 1.5 to 2-full order. The highest productivity attained is 44.8 μmol/hr C-products (i.e. 314 μmol/hr.cm² per gm of catalyst) for a combination of Cu NF on Al grid + Cu NF on Cu foil electrode and also, a close value of 44.6 μmol/hr for Cu NF on Inconel foil.

The higher chain alkyl products were observed for the nano-foams, which were not present in the plain metallic electrodes. In addition to the C-products, there was a huge H₂ productivity.

The reusability of the working electrodes is also worked upon and long reaction times were also probed. A time dependent study on the fuel productivity, for the nano-foam electrodes showed the production rate to be stable.

Nano-foams showed to be highly porous materials, which opens up a pathway for their use in gas phase reactions for CO₂ reduction to fuels. Gas phase systems being advantageous in terms of no CO₂ solubility issues, separation of end-products from solvent, etc and more close to replicating of the nature's leaf (photosynthetic system), hold the key to future of artificial photosynthesis.

5.5 References

- [1] S. Berkman, G. Egloff, *Chem. Rev.*, 1934, **15**, 377-424.
- [2] M.F. Ashby, A.G. Evans, N.A. Fleck, L.J. Gibson, J.W. Hutchinson, H.N.G. Wadley, *Metal Foams: A design guide*, Butterworth-Heinemann, 2000.
- [3] S. S. Kistler, *J.Phys. Chem.*, 1932, **36**, 52-64.
- [4] R. W. Pekala, *J. Mater. Sci.*, 1989, **24**, 3221-3227.
- [5] J. Zhang, B. Li, A. Wang, *J. Mater. Chem. A.*, 2016, **4**, 2069-2074.
- [6] Y. Meng, T. M. Young, P. Liu, S. Wang, *Cellulose*, 2015, **22**, 435-447.
- [7] J. J. Gurav, I. K. Jung, H. H. Park, E. S. Kang, D. Y. Nadargi, *J. of Nanomater.*, 2010, **2010**, Article ID: 409310.
- [8] S. S. Kistler, *Nature*, 1931, **127**, 741.
- [9] A. S. Dorcheh, M. H. Abbasi, *J. Mater. Processing Tech.*, 2008, **199**, 10-26.
- [10] A C. Pierre, G. M. Pajonk, *Chem. Rev.*, 2002, **102**, 4243-4266.
- [11] L. W. Hrubesh, *J. Non-crystalline Solids*, 1998, **225**, 335-342.
- [12] A. V. Rode, S. T. Hyde, E. G. Gamaly, R. G. Elliman, D. R. Mckenzie, S. Bulcock, *Appl. Phys. A.*, 1999, **69**, 755-758.
- [13] A. Zani, D. Dellasega, V. Russo, M. Passoni, *Carbon*, 2013, **56**, 358-365.
- [14] S. Li, G. Ji, L. Lu, *J. Nanosci. Nanotechnol.*, 2009, **9**, 1133-1136.
- [15] K. J. Kreder III, A. Manthiram, *Chem. Commun.*, 2017, **53**, 865-868.
- [16] B. C. Tappan, S. A. Steiner III, E. P. Luther, *Angew. Chem.*, 2010, **49**, 4544-4565.
- [17] B. C. Tappan, M. H. Huynh, M. A. Hiskey, D. E. Chavez, E. P. Luther, J. T. Mang, S. F. Son, *J. Am. Chem. Soc.*, 2006, **128**, 6589-6594.
- [18] L. P. Lefebvre, J. Banhart, D. C. Dunand, *Adv. Engg. Mater.*, 2008, **10**, 775-787.
- [19] C. Y. Zhao, Z. G. Wu, *Sol. Energy Mater. Sol. Cells*, 2011, **95**, 636-643.
- [20] I. Vukovic, S. Punzhin, Z. Vukovic, P. Onck, J. Th. M. De Hosson, G. T. Brinke, K. Loos, *ACS Nano*, 2011, **5**, 6339-6348.
- [21] H. C. Shin, M. Liu, *Chem. Mater.*, 2004, **16**, 5460-5464.
- [22] S. Sen, D. Liu, G. Tayhas, R. Palmore, *ACS Catal.*, 2014, **4**, 3091-3095.
- [23] R. Kas, K. K. Hummadi, R. Kortlever, P. de Wit, A. Milbrat, M. W. J. L. Olieman, N. E. Benes, M. T. M. Koper, G. Mul, *Nat. Commun.*, 2016, **7**, 10748.
- [24] R. Zhang, W. Lv, L. Lei, *Appl. Surf. Sci.*, 2015, **356**, 24-29.
- [25] S. Rasul, D. H. Anjum, A. Jedidi, Y. Minenkov, L. Cavallo, K. Takanabe, *Angew. Chem. Int. Ed.*, 2015, **54**, 2146-2150.

- [26] Y. Wang, J. Zhou, W. Lv, H. Fang, W. Wang, *Appl. Surf. Sci.*, 2016, **362**, 394-398.
- [27] W. Lv, J. Zhou, F. Kong, H. Fang, W. Wang, *Int. J. Hydrogen Energy*, 2016, **41**, 1585-1591.
- [28] R. Kas, R. Kortlever, H. Yilmaz, M. T. M. Koper and G. Mul, *ChemElectroChem*, 2015, **2**, 354–358.
- [29] R. J. Lima, M. Xiea, M. A. Ska, J. M. Leea, A. Fisher, X. Wanga, K. H. Lim, *Catalysis Today*, 2014, **233**, 169–180.
- [30] A. Mzerd, B. Aboulfarah, A. Giani, A. Boyer, *J. Mater. Sci.*, 2006, **41**, 1659–1662.
- [31] R. Venkatasubramanian, T. Colpitts, E. Watko, M. Lamvik, N. El-Masry, *J. Cryst. Growth*, 1997, **170**, 817-821.
- [32] L. Bu, W. Wang, H. Wang, *Appl. Surf. Sci.*, 2007, **253**, 3360–3365.
- [33] H. C. Shin, M. Liu, *Chem. Mater.*, 2004, **16**, 5460-5464.

Materials and Reagents

Chemicals used in our synthesis route are Iron (III) nitrate nonahydrate [Fe(NO₃)₃.9H₂O], Iron (II) Sulphate [FeSO₄], Copper (II) Sulphate [CuSO₄], Copper (II) acetyl acetonate [Cu(C₂H₇O₂)₂ or Cu(acac)₂], acetic acid (CH₃COOH, 99.5%), nitric acid (HNO₃, 65%), sulphuric acid (H₂SO₄, 95%), Hydrochloric acid (HCl, 37 %) potassium bicarbonate (KHCO₃, 99.7%), Nafion perfluorinated resin were obtained from Sigma-Aldrich and used without any further purification. Nafion membrane (Nafion¹¹⁷) was obtained from Ion power and was pre-treated before use. Iron foil (99.5 %) was purchased from Goodfellow and Copper foil (99.99 %) was acquired from Alfa Aesar.

Characterization Tools:

X-Ray Diffraction (XRD):

XRD was performed to determine the crystal structure of the catalysts using a D2 Phaser Bruker diffractometer equipped with a Cu-K α radiation (1.5406 Å) source operating at 30 kV and 10 mA. A scan rate of 0.025°/s with a 2 θ range in 12° to 100° was used for data collection.

X-Ray photoelectron spectra (XPS):

Quantitative surface analysis was performed by XPS using PHI 5000 VersaProbe II spectrometer with a monochromatic Al-K α X-ray source operated at 100 W, 20 kV.

Scanning Electron Microscopy (SEM & EDX):

The physical structure and elemental composition of the materials was performed by Phenom ProX Scanning Electron Microscope (SEM) equipped with EDS analyser. The other nano-foam on different metals and pure metals EDX data are shown in the [Fig. 5.15](#).

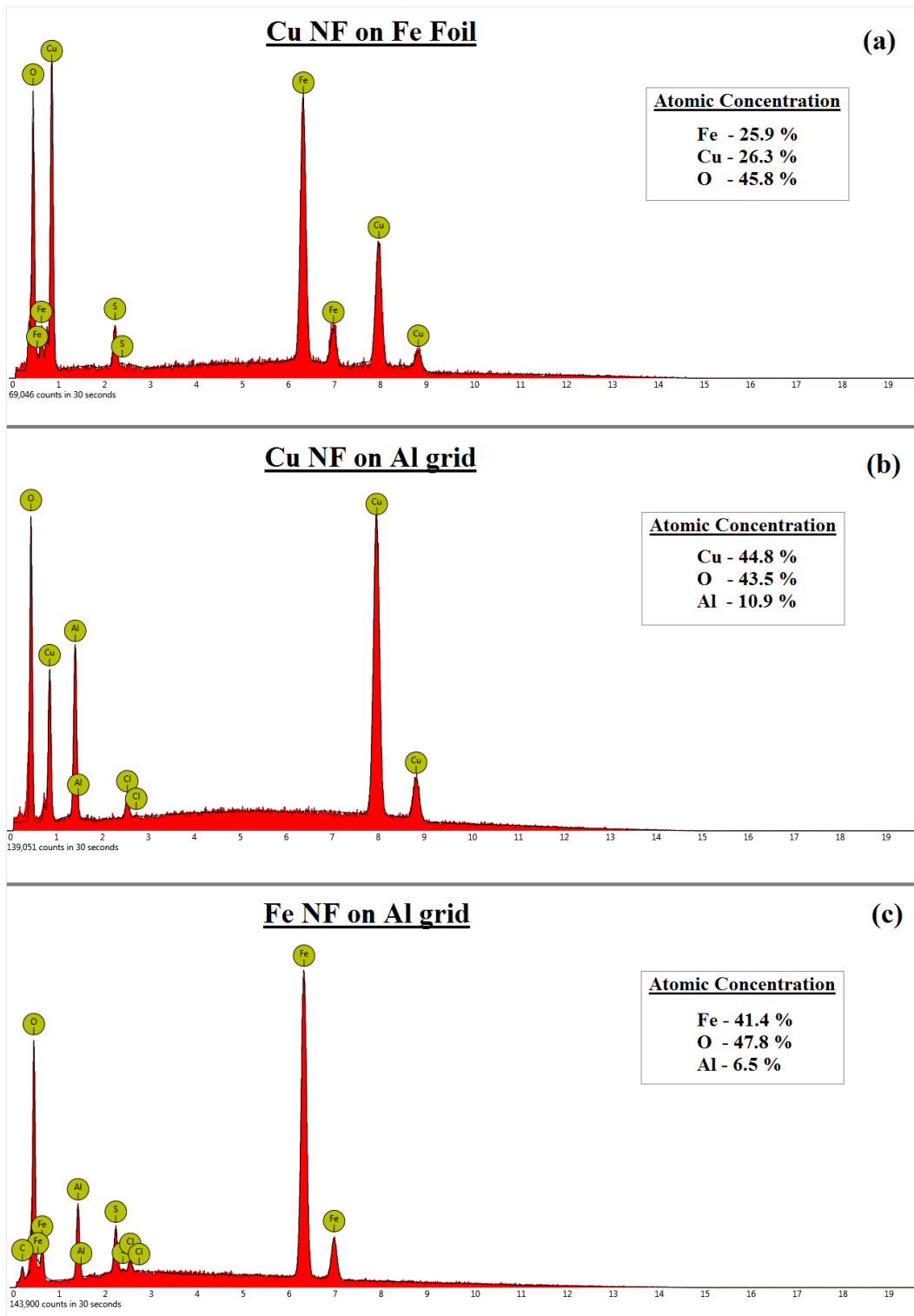


Fig. 5.15 EDX spectra for (a) Cu NF on Fe foil; (b) Cu NF on Al grid; (c) Fe NF on Al grid.

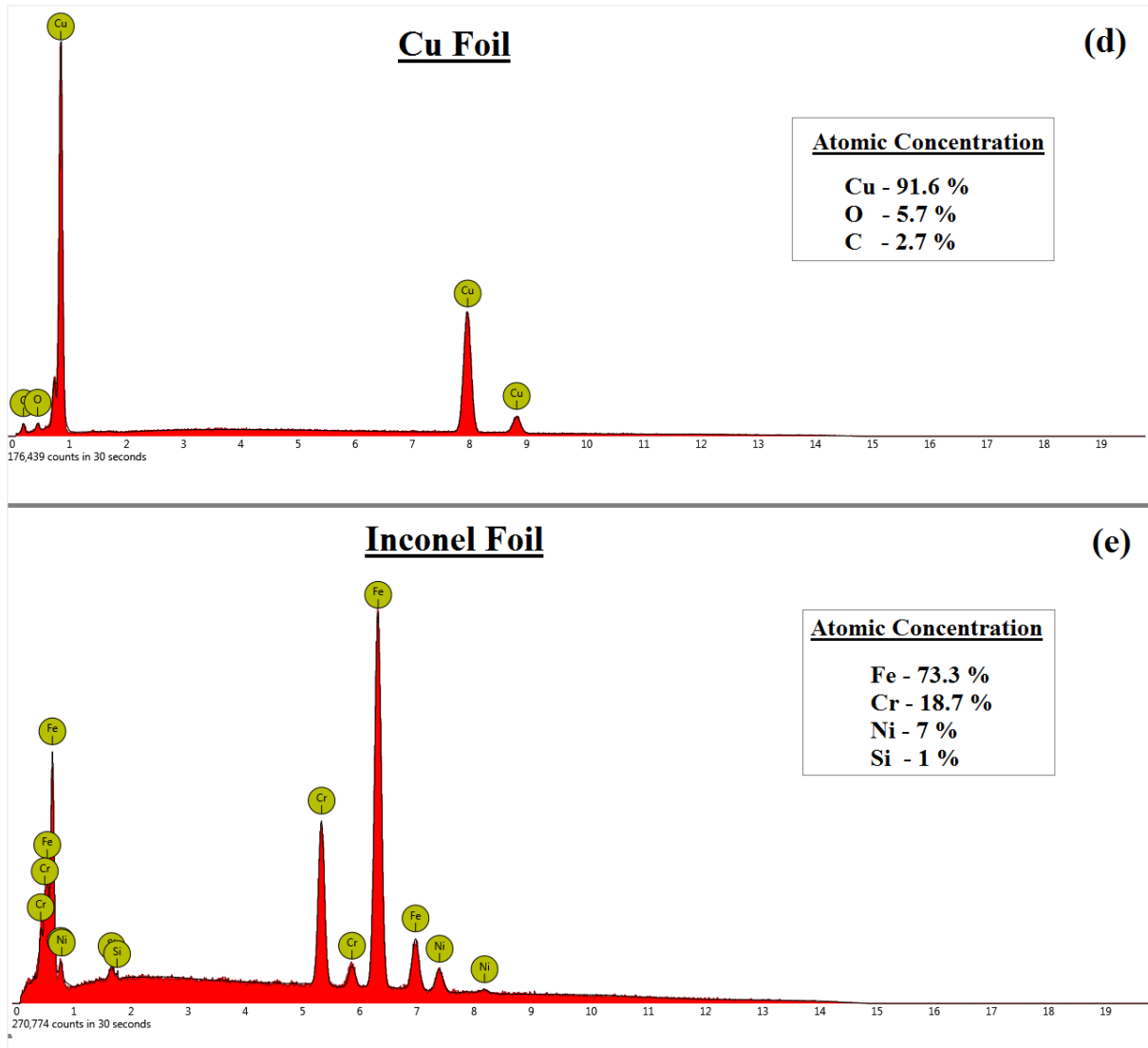


Fig. 5.15 EDX spectra for (d) Cu foil (polished); (e) Inconel foil.

CHAPTER 6

6. General Conclusions

The PhD research of this thesis has concerned the study of two different electro-catalytic CO₂ reduction systems: 1) electrolyte-less (gas phase) cell and 2) electrolytic (liquid phase) cell. These devices were used to test different metal doped carbon based catalytic electrodes, prepared via various novel synthetic routes or modified by metal-organic-frameworks, and other metallic nano-foam based electrodes. The major goal, as mentioned in the beginning of the thesis, was to develop an efficient device (better if working in gas phase) and the related tailor-made catalytic electrodes, which are close to mimic a natural photo-synthetic system, termed as artificial leaf.

Initially, a novel catalytic gas phase cell working with electrodes based on carbon based gas diffusion layers (GDL) was employed. Various catalysts were synthesized using noble and non-noble metal (Pt, Fe, Cu, CuFe, etc) nanoparticles deposited on carbon substrates (carbon black – CB – and carbon nanotubes - CNTs). These electrodes were tested to evaluate their performances in reducing CO₂ to liquid fuels. Moreover, further improvements were achieved by modifying these catalysts with substituted Zeolitic Imidazolate (SIM-1) type MOF coatings in order to improve CO₂ adsorption. Results showed that these MOF-modified catalysts (especially Pt/CNTs/GDL/MOFs) allowed not only to increase the productivity, but also to modify the selectivity, evidencing an active catalytic role in the electro-catalytic CO₂ reduction. Particularly, for the case of Pt-CNT-MOF the C-products improved by 1.5 times and the H₂ evolution decreased by 2 times, while, there was a shift in selectivity towards ethanol and isopropanol in comparison to basic Pt-CNT electrodes. On the other hand, for the case of Fe-CNT-MOF the C-products decreased by 20% and the H₂ evolution increased by 1.6 times. This can be considered as an initial step into understanding the effects of supplementing the working electrode with MOFs and it opens the basis for further experimentation.

In the next stage, the focus of the work was shifted towards a proper comparison for the results obtained in the gas phase with those reported in literature, which were carried out mainly in liquid phase in presence of an electrolyte. For this reason, one of the main research activity of the present PhD was to develop and realize a novel liquid phase electro-catalytic device for testing the electrodes under conditions very similar to those studied conventionally in literature.

The comparison of the same kind of electrodes in the process of CO₂ reduction in the presence (liquid-phase) or absence (gas-phase) of a bulk electrolyte, provided a series of interesting indications both on the limiting steps of the process and on the reaction mechanism. It was demonstrated that under electrolyte-less (EL, i.e. gas phase) operations, even if the total productivity of liquid fuels was slightly lower than liquid phase, more interesting products (higher C-chain alcohols and oxygenates) were formed. This is to relate to differences in the reaction mechanism, which were fully discussed, although further studies are needed to clarify better these aspects. In gas phase, Fe based catalyst showed very attractive results, even with respect to noble metals (Pt).

In liquid-phase operations, it was suggested that the mechanism involves the step reduction via intermediate formation of formic acid and formaldehyde and finally methanol, although the latter step was observed only in some electrodes. In fact, due to the strong acid conditions present at the electro-catalyst, located at the interface with the Nafion membrane, formic acid may decompose to generate CO, which reacts with formaldehyde to form acetic acid. Methanol may also react further in these strong acid conditions to form methyl formate.

In liquid phase, Cu and Ru based catalysts showed promising results much better than Co, Fe and good selectivity towards methanol production, in contrast to the results obtained in gas phase. This was due to the gas-phase operations mechanism being different to that of liquid phase and the conversion of CO₂ involved its dissociation to CO, which remains strongly chemisorbed, giving rise to further transformation reactions and formation of C-C bonds that produce a different spectrum of products in comparison to that of the liquid-phase operations.

The electrocatalysts utilized in liquid phase were based on metal nanoparticles (Fe, Cu, Co, Pt, Ru) deposited on two types of conductive carbon supports: carbon nanotubes functionalized by oxidation treatment (CNT_{ox}) and carbon black (CB). CNT_{ox} without metal particles was active both in producing H₂ from protons/electrons and in the reduction of CO₂. The possible mechanism and the role of the carboxyl and carbonyl groups, formed during the oxidative treatment, was discussed. In presence of metal nanoparticles, the carbon does not act only as a support or to transport charges, but has also an active role in the reaction mechanism. It was suggested that the active sites for the electro-catalytic reduction of CO₂ were located at the perimetral edge between metal nanoparticles and the carbon. The nature of the latter, in particular the type of surface functional groups, determines thus considerably the performances, as experimentally observed.

As commented, these results are the start, not the end of the analysis of the mechanism of reaction in the type of electrodes investigated here. However, we believe that these results evidence how a more complex surface chemistry than typically supposed in literature is present in the electro-catalytic reduction of CO₂ on the type of electrodes we investigated. It should be commented that their performances were better than those of various other electrodes reported in literature for the conversion of CO₂, even if the reaction conditions were different and way to report the data did not often allow a precise comparison.

There was thus the need for a better understanding of the performances and reaction mechanism of these electro-catalysts (based on metal nanoparticles on conductive, functionalized carbon support) for the reduction of CO₂. They may open new possibilities in controlling the type of products formed and their productivity in this challenging reaction.

Aiming at improving the performances of the process of CO₂ reduction to fuels, the effect of size of the nanoparticles on this reaction was also investigated. Organo-metallic synthesis route was used for synthesizing CNTs loaded with Pt, Ru and Fe NPs, as well as nanowire route for Cu NPs loaded CNTs to attain uniform, well dispersed and ultrafine sized nanoparticles of (avg. size – 1.1 nm Pt; 1.5 nm Ru; 2.9 nm Cu; 5 nm Fe). The NPs were also found to be quite stable. A novel synthesis route and specific conditions have been presented to obtain small Fe NPs of size (1-5 nm; average NPs size of 2 nm in solution phase before transfer onto CNTs).

The various products detected in the liquid phase and the selectivity towards different products were discussed. An insight into the CO₂ reduction to fuel productivity dependence on the size of the nanoparticles was presented for the electrodes formed using different electrocatalysts – (i) CNT_{ox} considered to draw a reference value; (ii) Fe, Pt, Ru and Cu - CNT_{ox} (via impregnation route, ImR) creating nanoparticles of average sizes (9.3 nm Fe; 10.4 nm Cu; 7.8 nm Pt; 2.6 nm Ru); (iii) Fe, Pt, Ru and Cu - CNT_{ox} (via organo-metallic route, OM and nanowire route, NW) for very small nanoparticles formation (size range 1–5 nm, see above). The study showed that there was as much as one-full-order increase in the carbon fuel productivity for Cu, Ru with decreasing nanoparticle size from 8-12 nm to 1-3 nm. For the Pt NPs case, the C-fuels productivity increased by 5 times and for the Fe NPs case, the C-fuels productivity more or less remains the same as the most of the energy is utilized towards the H₂ generation. A similar trend was observed for the decreasing size of NPs, which leads to higher hydrogen evolution reaction (HER). Moreover, by comparing the catalysts prepared by OM

and ImR routes (Ru, Pt, Fe and Cu), the productivity of the gaseous H₂ fuel increased by a factor of 2, 1-order, 4 and 7 times, respectively. This is worth noting, though it is not the major goal for the CO₂ reduction reaction.

The reusability of the working electrodes was also worked upon and long reaction times were also probed. In terms of TOF values, the enhancement in fuel productivity was noted to be 80 to 300 % higher for Cu NPs in comparison to different results reported in the literature.

It is also interesting to comment on the significant decrease in the metal loading (from ~ 10 % to ~1-2 %), with better C-products efficiency and in addition to increased H₂ evolution. The steady rate of generation of products was also addressed, giving an insight into the stability of the catalytic electrode. The equilibrium current ranges in from 2.5 mA to 7.5 mA, which demonstrated that very small current was enough to reduce CO₂ to fuels. This fell well within the range of photo-current generated in photo-catalysis works, signifying the feasibility of a full cell photo-electro catalysis.

Finally, a different set of electrodes based on nano-foams or dendrites prepared by electro-chemical deposition technique on metal foils, were investigated to improve further the efficiency of the CO₂ electro-reduction process to fuels. Optimization studies on the deposition of these foams were performed initially to fix the set of preparation conditions. The voltage optimization study was performed using cyclic voltammetry and full CO₂ reduction tests to find an optimum voltage for the reactions. The nano-foam electrodes tested included Cu and Fe foams on Cu foil, Fe foil, Al foil, Inconel foil and Al grid/mesh. The enhancements in the fuel productivity for these nano-foam based electrodes were in the range of 2-10 times greater as compared to the highest net fuel productivity achieved using metal NPs doped carbon catalytic electrodes, from all the previous studies. Moreover, it is interesting to note that these nano-foams based electrodes can be slightly modified to work in gas phase reactions, which might be a good starting point to a novel path into new electrode models in the gas phase conditions.

PERSONAL INFORMATION

BHANU CHANDRA MAREPALLY



Papardo Residence, ERSU, University of Messina, 98166 MESSINA (Italy)

+33 3456726829 +91 7675824181

mbhanu.iit@gmail.com

Sex Male | Date of birth 12/05/1987 | Nationality Indian

EDUCATION AND TRAINING

07/02/2014–03/04/2017	Erasmus Mundus SINCEM – Doctoral Fellow at --- (1) UNIVERSITY OF MESSINA, ITALY (2) CPE, UNIVERSITÉ CLAUDE BERNARD LYON, FRANCE.	EQF level 8
15/07/2013–20/01/2014	Doctoral Student in NANO TECHNOLOGY as CSIR-JRF Fellow VIT UNIVERSITY, VELLORE, TAMIL NADU (India)	EQF level 8
12/07/2011–21/05/2013	MASTER OF TECHNOLOGY IN NANO TECHNOLOGY VIT UNIVERSITY, VELLORE, TAMIL NADU (India) Nano Photonics, Synthesis of Nano Materials and Thin Film Deposition, Advanced Characterization and Lithography Techniques, Carbon Nanotubes, Inorganic Nanowires and Functionalization, Nano Electronics	EQF level 7
12/07/2005–05/07/2009	BACHELOR OF TECHNOLOGY IN ELECTRONICS AND COMMUNICATIONS ENGINEERING IIIT - HYDERABAD, Telangana (India) VLSI Design, Signal Processing, Analog & Digital Circuits, Gravity & Cosmology	EQF level 6
01/06/2002–30/04/2004	Intermediate (Higher Secondary Education) Board of Intermediate, Hyderabad, Andhra Pradesh (India) Maths, Physics, Chemistry	EQF level 4

PERSONAL SKILLS

Mother tongue(s) TELUGU

Other language(s)

	UNDERSTANDING		SPEAKING		WRITING
	Listening	Reading	Spoken interaction	Spoken production	
Hindi	C2	C2	C2	C2	C2
English	C2	C2	C2	C2	C2
TOEFL IBT CERTIFICATION					
German	A2	A2	A1	A1	A1
Guajrati	A2	A2	A1	A1	A2
Italian	A1	A1	A1	A1	A1

Levels: A1 and A2: Basic user - B1 and B2: Independent user - C1 and C2: Proficient user
 Common European Framework of Reference for Languages

PUBLICATIONS

- 1) C. Ampelli, C. Genovese, B. C. Marepally, G. Papanikolaou, S. Perathoner and G. Centi, "Electrocatalytic conversion of CO₂ to produce solar fuels in electrolyte or electrolyte-less configurations of PEC cells", *Faraday Discuss.*, 2015, **183**, 125-145.
- 2) Chiara Genovese, Claudio Ampelli, Bhanu C. Marepally, Georgia Papanikolaou, Siglinda Perathoner, Gabriele Centi, "Electrocatalytic Reduction of CO₂ for the Production of Fuels: a Comparison between Liquid and Gas Phase Conditions", *Chem. Eng. Trans.*, 2015, **43**, 2281-2286.
- 3) Bhanu Chandra Marepally, Claudio Ampelli, Chiara Genovese, Francesco Tavella, Laurent Veyre, Chloe Thieuleux, Elsjé Alessandra Quadrelli, Siglinda Perathoner, Gabriele Centi, "Ultrafine Cu nanoparticles onto nanocarbon-based electrodes for the electrocatalytic reduction of CO₂", *Journal of CO₂ Utilization* - (submitted).
- 4) Bhanu Chandra Marepally, Claudio Ampelli, Chiara Genovese, Reine Sayah, Laurent Veyre, Chloe Thieuleux, Elsjé Alessandra Quadrelli, Siglinda Perathoner, Gabriele Centi, "Organometallic approach towards size controlled nanoparticles: An Investigation into dependence on the size and dispersion on the performance of electrocatalytic reduction of CO₂", - (to be submitted).
- 5) Bhanu Chandra Marepally, Claudio Ampelli, Chiara Genovese, Tapish Saboo, Siglinda Perathoner, Gabriele Centi, "Nanofoams for enhanced performance of electrocatalytic reduction of CO₂" - (to be submitted).

CONFERENCE PRESENTATIONS

- 1) XVIII National School of Material Science and Technology, Ischia, Italy.
- 2) The 3rd CO₂ Forum, International Conference, Lyon, France.
- 3) The 3rd International Symposium on Green Chemistry (ISGC-III), La Rochelle, France.
- 4) The 12th International Conference on Chemical & Process Engineering, AIDIC, ICheaP12, Milan, Italy.
- 5) The XII European Congress on Catalysis (EuropaCat-XII), Kazan. Russia.
- 6) The 3^o SINCHEM Winter School, Bologna. Italy.
- 7) The 7th International Symposium on Carbon for Catalysis (CarboCat-VII), Strasbourg, France.